Master's Thesis

# Carbonization Study of Cellulose Nanocrystals and its Applications for Battery Anode, and Super Engineering Plastic Based Nano Composite Fibers

Yea Eun Kim

Department of Materials Science and Engineering

Graduate School of UNIST

2020

# Carbonization Study of Cellulose Nanocrystals and its Applications for Battery Anode, and Super Engineering Plastic Based Nano Composite Fibers

Yea Eun Kim

Department of Materials Science and Engineering

Graduate School of UNIST

# Carbonization Study of Cellulose Nanocrystals and its Applications for Battery Anode, and Super Engineering Plastic Based Nano Composite Fibers

A thesis/dissertation
submitted to the Graduate School of UNIST
in partial fulfillment of the
requirements for the degree of
Master of Science

Yea Eun Kim

11. 27. 2019 of submission
Approved by

Advisor
Han Gi Chae

# Carbonization Study of Cellulose Nanocrystals and its Applications for Battery Anode, and Super Engineering Plastic Based Nano Composite Fibers

Yea Eun Kim

This certifies that the thesis/dissertation of Yea Eun Kim is approved.

11. 27. 2019 of submission

Advisor: Han Gi Chae

Myoung Hoon Song

Hyun-Wook Lee

## Abstract

Cellulose nanocrystals (CNCs) are extracted from cellulose materials by removing amorphous parts through acid hydrolysis. The nanometric CNCs with rod shape have intrinsically well-ordered crystalline structures. CNCs have been used as nanofillers for nanocomposites and promising carbon precursor based on the high mechanical properties, natural abundancy, high crystallinity, high surface area, and many functional groups on the surface. Based on these features, the carbonized CNCs and the pristine CNCs have been mainly studied for the applications.

In chapter 2, spray-dried CNCs (SD-CNC) were carbonized to prepare the highly efficient carbon anode material for sodium ion batteries (SIBs). Development of SIBs paves a new way as an alternative of lithium-based batteries. Even though sodium has similar chemical properties to lithium, it is unable to achieve facile intercalation reaction of sodium ion in graphite because of the larger ionic radius of Na (102 pm) and narrow interlayer distance of graphite (0.335 nm). Thus, new carbon-based anode materials for SIBs should be developed. SD-CNCs were carbonized at the various carbonization temperature (i.e., 800–2500 ℃) and the anodes for SIB were prepared from the carbonized SD-CNCs. The microstructure of carbonized SD-CNC was investigated and electrochemical performance was measured. Upon increasing carbonization temperature, the less ordered structures are decreased, resulting in the decrease of the irreversible and sloping capacities. The ordered crystal structure with d-spacing above 0.37 nm are developed up to 1500 °C, resulting in the increase of plateau capacity. The d-spacing is suddenly dropped down to 0.345 nm at 2500 °C, and it leads to the dramatical decrease of plateau region. By correlating the microstructure with the electrochemical performance, the sodium ion storage mechanism was derived. The sloping capacity (above 0.2 V) is attributed to the sodium ion adsorption to the structural defects and the plateau region (below 0.2 V) is attributed to the sodium ion intercalation between graphene layers. Among the carbonized SD-CNCs, the carbonized SD-CNC show the best performance in SIBs, which is the reversible capacity of 310.6 mAh $g^{-1}$ at 10 mA $g^{-1}$ with highest initial coulombic efficiency (ICE) of 85%. Also, it shows the excellent specific capacity retention of 92.3% even after 400 cycles at 100 mA $g^{-1}$.

In chapter 3, freeze-dried CNCs (FD-CNCs) with nanometric and fibrillar morphology were prepared by freeze drying for the precursor of carbon nanofillers from CNCs with the well-ordered crystal structure. Then, FD-CNCs are carbonized for the preparation of high-surface area carbons. Structural evolution mechanism of FD-CNCs was investigated during carbonization from 1000 to 2500 °C. The weak and amorphous structure from the pristine state was converted into amorphous carbon or amorphous (A)-component with heat-treatment while the intrinsically highly crystallized parts become turbostratic (T)- or graphitic (G)-components at the low carbonization temperature of

1000 °C. The FD-CNCs undergo four stages of structural development with carbonization temperature: In stage 1, the carbons with turbostratic structure are developed. In stage 2, small carbon crystallites with many defects are observed while the more ordered structure is seen as compared to the stage 1. In stage 3, graphitic crystals begin to develop, and subsequently in stage 4, the size of graphitic crystals dramatically increases via coalescence and lateral inter-fusion between crystals with removal of the defects. Meanwhile, the effects of oxidative stabilization are negligible due to the rapid heat diffusion and uniform structural change based on the high surface area of FD-CNCs. Carbonized FD-CNCs show the superior dispersibility due to the high surface area, indicating the possibility for carbon nanofillers.

In chapter 4, CNCs were applied as a reinforcement to enhance the mechanical properties of polymer. Polyether imide (PEI)/cellulose nanocrystal (CNC) nanocomposite fibers were dry-jet wet spun at CNC concentrations of 0, 1, 3, and 5 wt.% with respect to the polymer. The as-spun fibers were drawn in the draw ratio (DR) range from 2.8 to 7, and the behavior of their mechanical properties and fiber structures has been studied upon drawing at various amounts of CNC. At a DR of 7, the tensile strength and modulus of control fibers were 466.2 MPa and 8.1 GPa, respectively, and those of PEI/CNC3 fibers were 408.9 MPa and 9.2 GPa, which are the highest of any mechanical properties reported previously. The increase in tensile modulus by the addition of CNC was significantly influenced by the alignment of CNC along the fiber axis and the high specific modulus of CNC itself, rather than by the alignment of PEI polymeric chains. CNC, which is a crystalline material, already showed a high degree of orientation in the as-spun fibers and they became further aligned rapidly with drawing. Whereas, the orientation of amorphous polymeric chains developed slowly and exhibited still a low orientation factor even after drawing to a maximum extent. Further, the degree of orientation of PEI chains in the composite fibers was lower than that in the control fibers, indicating that the CNC disturbed PEI alignment to the axial direction. This research suggested that optimizing processing condition can maximize the mechanical properties of even amorphous polymers and adding nanofillers can further improve the properties.

# Table of Content



## Contents

# List of Figures

# List of Tables

# Chapter 1. Introduction to cellulose nanocrystals

## 1.1 Cellulose Nanocrystals (CNCs)

Cellulose is the most abundant biopolymer available on the earth and it is considered as primary carbon resource capable of mass production at low cost. It is found in a variety of organisms such as tunicate, algae, bacteria, fungi as well as plants and woods [1, 2]. Cellulose is a fibrous, tough, and insoluble polymer in water and it plays an indispensable role in maintaining the structure of plant cell walls. The figure 1.1 shows the chemical structure of cellulose formed by condensation. Cellulose is composed of β-1,4-linked glucopyranose units that form a linear homo-polymer with high molecular weight, in which every monomer unit is corkscrewed at 180° with respect to its neighbors [1-3]. The degree of polymerization of cellulose can vary depending on the source and it is approximately 10,000 glucose units for wood-derived cellulose and 15,000 units for cotton-derived cellulose. Each glucopyranose unit bears three hydroxyl groups, which impart cellulose some of the characteristic properties such as hydrophilicity, chirality and biodegradability which are initiated by the high reactivity of the hydroxyl groups. The ability of these hydroxyl groups to form strong hydrogen bonds is the main reason for some other properties such as multiscale microfibrillar structure, hierarchical organization (crystalline and amorphous fractions), and highly cohesive nature.

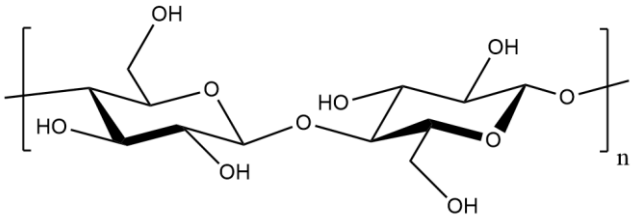


Figure 1.1 Chemical structure of cellulose.

Nanocomposites show exclusive properties compared to conventional composites based on the nanometric size effect [4]. Nanofillers can interact strongly with the polymer matrix based on the enlarged interface area, resulting in strong reinforcing effects. The improved properties of polymer nanocomposites have been reported in recent researches even at low content of reinforcements. In these days, polymer materials based on the renewable and biodegradable resources as like cellulose have attracted considerable attention for sustainability. The reinforcing ability of cellulose is primarily ascribed to its semi-crystalline structure and the extended chain conformation of cellulose molecules in

the crystalline regions. This structure results from the strong intermolecular hydrogen bonding from the hydroxyl groups of the cellulose molecule. By removing amorphous regions through acid hydrolysis, the resulting nanometric crystalline materials can be obtained, which is called by cellulose nanocrystals (CNCs). Among various nanocellulose materials, CNCs can be of great interest as a 'green' nanofiller for polymer nanocomposites due to the unique properties based on the high crystallinity [3-6].

## 1.2 Preparation of Cellulose Nanocrystals

### *1.2.1 Crystalline structure of cellulose*

There are four representative polymorphs of crystalline cellulose (I, II, III, IV). Cellulose I structure is the naturally occurring crystal structure produced by various species (plants, trees, tunicates, bacteria and algae) [3, 7]. Cellulose I structure is classified into two kinds of polymorphs, cellulose $I_\alpha$ (a triclinic structure) and cellulose $I_\beta$ (a monoclinic structure), which fraction depends on the source. The $I_\alpha$ structure is the dominate in most algae and bacteria, whereas $I_\beta$ is the dominant in plant cell wall cellulose and in tunicates [3, 7]. For both $I_\alpha$ and $I_\beta$ unit cells, the cellulose chains are arranged in what is called the "parallel up" configuration. Since the cellulose repeat unit has a different structure on either side of the 1–4 linkage, the directionality of the 1–to–4 linkage (1–4 linkage) along the length of the cellulose chain affects how neighboring chains interact with each other [3, 7]. The term "parallel" is used when all the cellulose chains are arranged such that the 1–4 link points in the same direction. The "up" configuration corresponds to the 1–4 link direction pointing in the positive c-axis direction of the unit cell. Thus, all cellulose chains are arranged such that the 1–4 link points in the same direction and that direction is in the positive c-axis direction of their respective crystalline unit cell.

### *1.2.2 Extraction of cellulose nanocrystals*

Cellulose nanocrystals (CNCs) is produced by removing amorphous regions of the cellulosic materials through acid hydrolysis. This acid hydrolysis step is followed by centrifugation, dialysis, and ultrasonication. Different strong acids have been shown to successfully degrade non-crystalline (amorphous) regions of cellulose fibers to release crystalline cellulosic nanoparticles, such as sulfuric, hydrochloric, phosphoric, hydrobromic, nitric acids, and a mixture composed of hydrochloric and organic acids [1-3, 6]. Nevertheless, the acid hydrolysis with sulfuric acid has been used and appears to be the most effective method. One of the main reasons for using sulfuric acid as a hydrolyzing agent is related to the dispersibility of CNCs. During hydrolysis, sulfuric acid reacts with the hydroxyl groups on surface of CNCs via an esterification process allowing the introduction of anionic sulfate ester groups

($–OSO_3^-$). [1-3, 6] These sulfate groups are randomly distributed on the surface of CNCs. The presence of these negatively charged groups induces the formation of a negative electrostatic double layer in aqueous system, and it leads to the promotion of dispersion of CNCs in water. The CNC obtained by sulfuric acid-hydrolysis form the highly stable dispersed state in water by the electrostatic repulsion between individual nanoparticles.

Sebe et al. [7] reported that CNC with cellulose II structure can be obtained directly by treatment of microcrystalline cellulose (cellulose I substrate) with sulfuric acid by both controlling the amount of $H_2SO_4$ introduced and the time of addition during the hydrolysis process. They found that CNCs with cellulose II structure were significantly smaller than CNC with cellulose I structure, and they had rounded shapes like ribbon-shape morphology compared with the CNC with cellulose I wtructure of needle-shape morphology.

### *1.2.3 Mechanical properties of Cellulose nanocrystals*

The mechanical properties of CNCs have been attractive for the application of nanofillers of polymer nanocomposites [4, 5, 8-14]. Outstanding mechanical properties can be obtained by blending CNCs and a polymer matrix even at low filler contents. The properties originate from the high stiffness of crystalline cellulose that provides the strength to higher plants, the nanoscale dimensions, and high aspect ratio of the nanoparticles, and the high reactivity of cellulose [4, 5, 8-14].

For cellulose I, the elastic modulus is around 137 GPa when considering intramolecular hydrogen bonding, and 92 GPa without intramolecular hydrogen bonding, evidence of the important role of intramolecular bonding on the determination of the crystallite modulus and chain deformation mechanism [4]. For cellulose II, the average value is around 113 GPa [4]. The lower value observed for form II is ascribed to lower intramolecular hydrogen bonds, whereas the intermolecular hydrogen bonds were found to play a minor role. The highest mechanical reinforcement effect of CNCs is observed when using unmodified nanoparticles bearing hydroxyl groups and for materials processed by casting evaporation from a liquid medium in which they are homogeneously dispersed. Grunert et al. [15] studied the reinforcement effects of unmodified and modified CNCs in polymer nanocomposites. They prepared the topochemically trimethylsilylated CNCs to improve the interaction with the hydrophobic matrix of cellulose acetate butyrate by reducing hydrophilicity of CNCs. They found that the unmodified CNCs exhibited better reinforcements due to the high hydrogen bonding.

## 1.3 Carbonization of Cellulose Nanocrystals

### *1.3.1 Carbonization mechanism of cellulose nanocrystals*

Eom et al. [16] studied the structural evolution mechanism of cellulose nanocrystals during carbonization in the temperature range of 1000 – 2500 °C. Raman shows the three stages of structure developments of CNCs during carbonization depending on the carbonization temperature; (1) formation of turbostratic-graphitic structure below 1500 °C (1st stage), (2) phase conversion to polycrystalline graphite between 1500 and 2000 °C (2nd stage), and (3) in-plane homogenization to highly ordered graphite above 2000 °C (3rd stage). They also reported that the structure of stabilized and carbonized CNC has been developed due to dehydration at low temperature, which help the heteroatoms be removed, compared to directly carbonized CNC at the same temperature.

Zhu et al. [17] reported that the formation of nanometric graphitic carbon from the ordered CNC even at 1000 °C. The *in-situ* TEM data proves the formation of graphitic carbon from CNC under 1000 °C carbonization. performed the simulation to investigate the low-temperature carbonization mechanism of CNCs below 1000 °C. They also performed molecular dynamics (MD) simulation to analyze the formation mechanism of ordered carbon from CNCs. At 600 K, the cellulose bundle which contains 36 cellulose chains with 4 repeat units remains in a rather crystalline configuration. At 800 K, the crystalline configuration shows collapse of crystal boundary. The further decomposition of the cellulose bundle is caused with the increase of temperature. At 900 K, the original bundle has been de-polymerization into segments such as $H_2$, $H_2O$, CO, $CO_2$ and carbon radicals. At 1300 K, the entire cellulose bundle has been decomposed, and four carbon radicals and some other segments emerge.

Souza et al. [18] studied the CNCs with various morphologies were carbonized in the 300–1000 °C. They reported that the morphology of obtained carbonized CNC is attributed to the precursor arrangement. They also have observed the highly ordered graphitic carbon with rod-like structure in carbonized CNC at 1000 °C by TEM images. They carefully suggested that the formation of graphitic structure in carbonize CNC may be attributed that CNCs have strong hydrogen bonding, and it leads to welding of the carbon particles to form complex structures during carbonization.

Cho et al. [19] prepared fibrous carbon materials from self-assembled CNC fibers obtained by freeze drying. They reported that the CNCs with nanomicron and submicron fiber morphologies maintained their original morphologies after carbonization at 1000 °C, which is demonstrated by SEM images. They also suggested the importance of stabilization at low temperature in an oxidative atmosphere, which stabilize the cellulose materials by dehydration and by the formation of double bonds. The stabilization process can improve yield and properties of carbonaceous materials.

# Chapter 2. Structure dependent sodium ion storage mechanism of cellulose nanocrystal-based carbon anode

## 2.1 Introduction

The demands of lithium ion batteries (LIBs) have been continuously increased, but new battery systems should be developed due to the depletion of lithium resources and resulting high cost. Thus, sodium ion batteries (SIBs) have been attractive as a substitute based on the similar electrochemistry with lithium and resource abundancy. However, the graphite which is the commercial anode of LIB shows the extremely low capacity in SIBs. lithium has the smallest ionic radius which enables reversible intercalation into the graphite anode [20-22], but sodium intercalated graphite is thermodynamically unstable as proved by positive formation energy [21]. Also, the narrow interlayer distance of graphite (~0.34 nm) enables exfoliation of graphene layers by solvated sodium ions, which is not appropriate for practical application [22-26]. Moreover, calculated binding energy of $NaC_6$ is demonstrably lower than that of $LiC_6$ [21]. Therefore, new anode materials should be developed.

Among the various candidate for anodes, hard carbon materials have been regarded as the attractive candidate due to wide d-spacing, lots of pores and defects for sodium ion storage as well as the low cost of precursors [27-29]. The high fraction of defects and pores contribute to the considerable reversible capacity [17, 30-32]. However, several researches have reported that hard carbons show supercapacitor-like voltage profiles and the poor rate capability [17, 28]. Also, some hard carbons with the high surface area cause the high irreversible capacity, which reduces specific energy density of full cell [17, 33, 34]. Thus, the further process such as coating with soft carbon or additional chemical reactions is required to reduce the surface area [33, 35]. To avoid these complex processes, simple and low-cost processing of carbon-based anode materials with high-performance and high-energy should be required.

Among the hard carbon precursors, cellulose materials are attractive materials due to the abundant polymer resources in the earth [1, 2]. Removing amorphous parts of cellulose thorough acid hydrolysis, cellulose nanocrystals (CNC) are achieved [1, 2]. Obtained cellulose nanocrystals (CNC) is regarded as promising carbon precursor for hard carbon-based anode material with its intrinsically well-ordered crystal structure and high crystallinity [16, 17]. The microstructure of carbonized CNCs have been investigated with the carbonization conditions [16]. The microstructure such as the d-spacing, pores, surface area and defects in crystal depends on the carbonization temperature. Also, the long-range ordered graphitic structure is formed even at low temperature of 1000 ℃ due to the original crystal structure of CNC unlike the conventional cellulose materials. In addition, the morphology of CNC

depends on the drying process such as spray drying and freeze drying, resulting in the tunable surface area [36, 37].

Throughout temperature scanning (i.e., 800–2500 ℃), microstructure of the carbonized SD-CNCs are investigated to prepare the efficient carbon anode materials for SIBs. Electrochemical performance of carbonized SD-CNCs depends on the microstructures (less ordered structures and d-spacing). By the correlation of microstructure with the electrochemical performance, sodium ion storage mechanism in the carbon-based anode will be confirmed. Detailed observation on the sodium ion storage sites in the carbonized CNCs helps understanding on charge-discharge mechanism of sodium ion in carbon anodes.

## 2. 2. Experimental Section

### *2.2.1. Carbonization of CNC*

Spray-dried CNCs (SD-CNCs) were produced by CelluForce Co. (Canada) The as-received CNC powders were dried at 65 °C overnight and then directly carbonized at 800, 1000, 1500 and 2500 ºC (hereafter, referred to as SD-D800, SD-D1000, SD-D1500 and SD-D2500, respectively) under argon (Ar) at a heating rate of 5 °C $min^{-1}$ using a box furnace (Nasil Tech Co., South Korea) without isothermal heat treatment at the target temperature.

### *2.2.2 Cell preparation*

Anode electrode was prepared with carbonized CNC, binder (styrene butadiene rubber (SBR) and sodium carboxymethyl cellulose (CMC)), and carbon black (Super P) with the weight ratio of 8:1:1, using a Thinky Super Mixer (ARE-310) for 15 min. The mixed slurry was casted on Cu current collector by film coating technique using a doctor blade and dried at 100 °C for 12 h in a vacuum oven. 2032-coin cells were assembled in an Ar-filled glove box for half-cell test. The electrolyte was 0.7 M $NaClO_4$ in ethylene carbonate (EC) and diethyl carbonate (DEC) (1:1, v/v), and 10 wt.% of fluoroethylene carbonate (FEC) (PuriEL). A Glass-fiber filter (GFF) membrane (Whatman) was used to prevent short circuit between the anode and Na metal.

### *2.2.3 Characterization*

The morphology of the as-received and carbonized CNC was observed using scanning electron microscopy (SEM, Novanano230, FEI Co.) at an accelerating voltage of 10 kV. The samples were

placed on the carbon tape and coated with platinum at 20 mA for 45 s. The dimension and microstructure of the carbonized CNC were examined by a high-resolution transmission electron microscopy (HRTEM, JEM-2100. JEOL) operated at 200 kV accelerating voltage. The Brunauer-Emmett-Teller (BET) tests were measured on BELSORP-max (BEL Japan Inc.) by nitrogen adsorption-desorption isotherms to calculate the surface area. The pore size distributions were estimated by Barret-Joyer-Halenda (BJH) model. The crystal structure of carbonized CNC was evaluated by wide-angle X-ray diffraction (WAXD, D8 Advance, Rigaku) with Cu-Kα radiation (λ=1.54 Å) operating at 40 kV and 200 mA. Raman spectra of carbonized CNC were measured using an Alpha 300s micro Raman spectrometer (WITec) from 10 sites with 100 accumulations with accumulation time of 1s. The excitation wavelength was 532 nm and the laser power was 0.5 mV. Raman curve fitting was performed with the Peakfit software package to determine the spectral parameters. X-ray photoelectron spectroscopy (ESCALAB 250XI, Thermo Fisher Scientific) was performed to investigate the atomic percentage and the composition of $sp^2$ and $sp^3$ carbons in carbonized SD-CNCs.

The electrochemical properties were measured by galvanostatic charge/discharge test (WBCS3000) with the voltage window between 0.01 V vs. $Na/Na^+$ and 2.5 V vs $Na/Na^+$. The specific capacity of CNC-based electrode was calculated based on the total weight of active material on electrode. Cyclic voltammetry was also measured by EC-LAB potentiostat (BioLogic).

## 2.3. Results and discussion

### *2.3.1 Morphological analysis*

SD-CNC used in this study was prepared from wood fibers by removing amorphous part through acid hydrolysis, followed by dilution, neutralization, and spray drying (Figure 2.1). Figure 2.1a shows a TEM image of dispersed CNCs with the nanometric and fibrillar morphologies. The dimension of individual CNC was 23.9 ± 3.3 nm in diameter and 197.2 ± 4.4 nm in length as shown in Figure 2.1b and 2.1c. The pristine SD-CNCs show the form of fine powder (Figure 2.1d), and the form was preserved even after carbonization (Figure 2.1e). The prepared anode of carbonized SD-CNC is represented in Figure 2.1f. As shown in Figure 2.2a, SD-CNCs macroscopically shows the densely aggregated morphology due to the drying process of spray-drying [36, 37]. The SEM images of carbonized CNCs are also shown in Figure 2.2b-e and the compact morphologies of pristine CNCs are maintained even after carbonization. It is interesting that the pores were formed on the surface of granule after carbonization, which was not observed on the surface of pristine SD-CNC (Figure 2.2f-j) [38, 39]. To investigate the surface area and pore volume, $N_2$ adsorption-desorption measurements were performed (Figure 2.3), and the Brunauer-Emmett-Teller (BET) surface area and the pore distribution were calculated (Table 2.1). The surface area and pore volume of carbonized SD-CNCs are higher than those of the pristine SD-CNC because of the emission of volatile byproducts by the decomposition during carbonization, corresponding to the rough surface with pores (Figure 2.2g-j). With the increase of the carbonization temperature, the surface area and total volume fraction decrease. It is attributed to the increase in density of carbon by the growth and fusion of graphitic crystal based on the high thermal energy [40]. The surface area of all carbonized CNCs except SD-D800 is below 10 $m^2/g$. The surface area is important factor for the reversible capacity and long-term performance in battery system, because the solid electrolyte interphase (SEI) layer is formed on the surface of carbon anode by consuming sodium ion. During the first charge/discharge, it is well-known that the carbon with low surface area shows the low irreversible capacity, resulting in the high ICE. Therefore, except SD-D800, all carbonized CNCs will show the low irreversible capacity and it can be achieved by the usage of the appropriate carbon precursor SD-CNC, without the additional process to reduce the surface area.

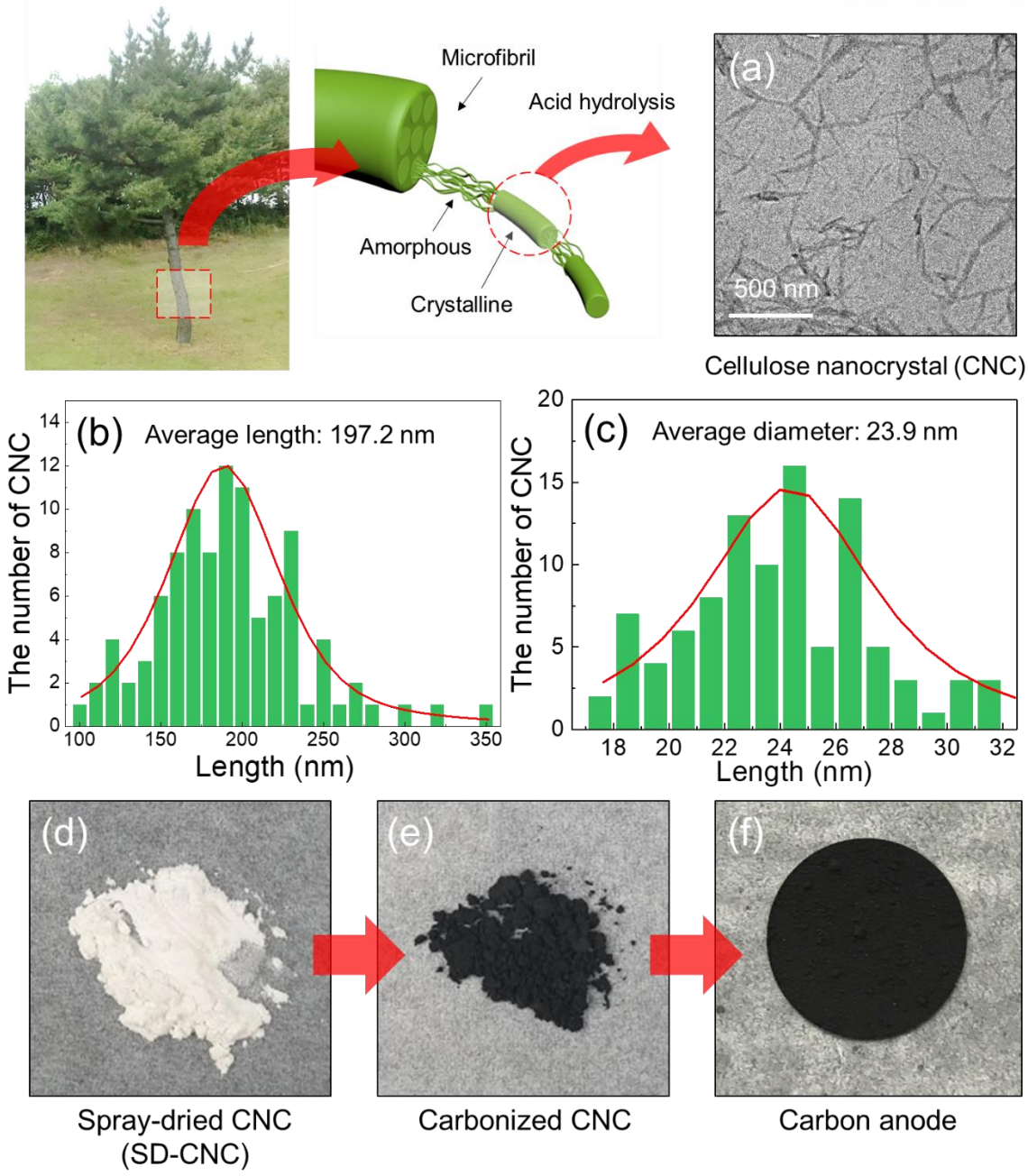


Figure 2.1 Schematic description of obtaining CNCs from natural source (wood, etc.). (a) TEM micrograph of the dispersed CNC, exhibiting rod-shape morphology. (b)-(c) Length and diameter distribution of CNC calculated from TEM images through Image J. (d)-(f) Photographs of the spray-dried CNC, the carbonized CNC, and the carbonized CNC-based anode fabricated on Cu foil, respectively. The composition of the anode was the carbonized CNC, the binder (styrene butadiene rubber and sodium carboxymethyl cellulose), and the carbon black (Super P) with a weight ratio of 8:1:1, respectively.

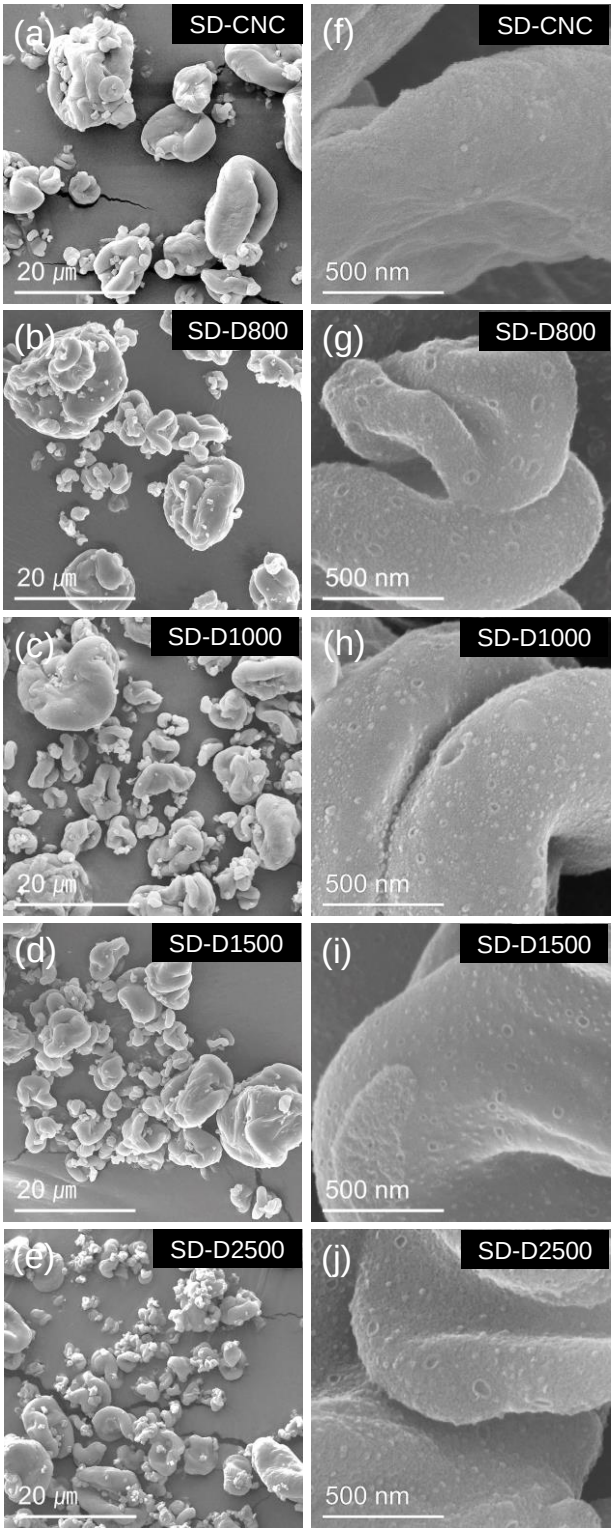


Figure 2.2 (a) SEM image of the spray-dried CNC (precursor). The precursor CNC exhibits compact morphology with various granule sizes. (b)-(e) SEM images of the CNCs carbonized at 800, 1000, 1500 and 2500 ℃, respectively. (f)-(j) The high magnification SEM images of (a)-(e), respectively. The pore structure development is observed on the surface of the carbonized CNCs.

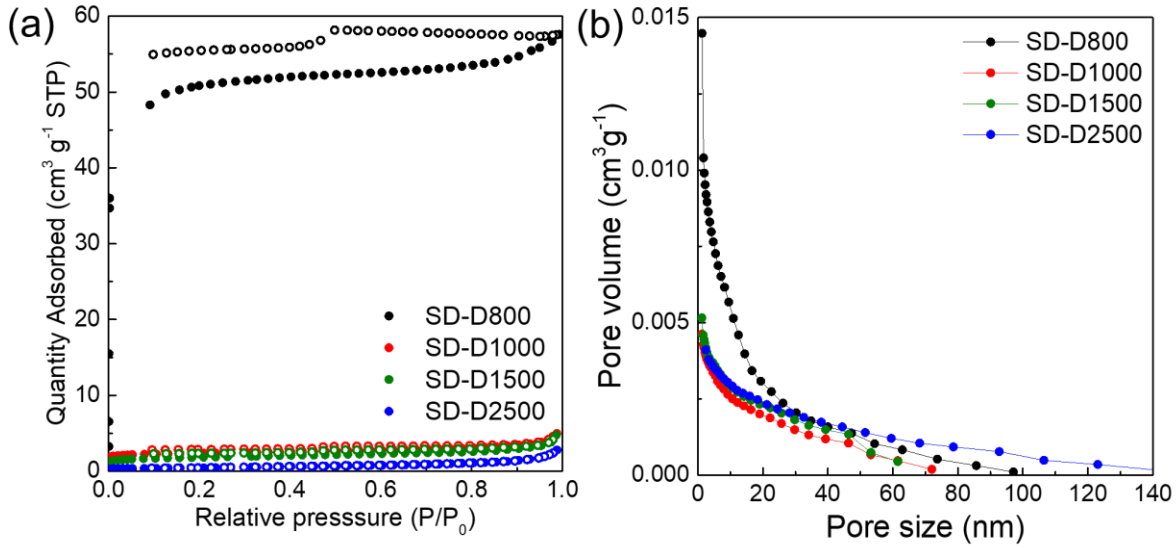


Figure 2.3 (a) $N_2$ adsorption-desorption isothermal curve and (b) the pore size distribution of carbonized CNC.

Table 2.1 The summary information about the structural properties of carbonized CNCs. The surface area and pore volume is based on the BET and BJH.

| | Surface area ($m^2$ $g^{-1}$) | Total pore volume ($cm^3$ $g^{-1}$) | Interlayer distance (nm) by XRD | Atomic percent of oxygen (%) | Atomic percent of carbon (%) | Atomic percent of $sp^2$ carbon (%) |
|---|---|---|---|---|---|---|
| SD-CNC | 0.7 | 0.0018 | – | – | – | – |
| SD-D800 | 192.6 | 0.0888 | 0.386 | 19.5 | 62.6 | 23.9 |
| SD-D1000 | 9.0 | 0.0078 | 0.385 | 8.5 | 87.5 | 39.8 |
| SD-D1500 | 6.7 | 0.0074 | 0.373 | 6.3 | 93.7 | 48.7 |
| SD-D2500 | 1.5 | 0.0043 | 0.346* | 3.4 | 96.6 | 62.8 |

* The interlayer distance of SD-D2500 is calculated from the broad hump at 25.8 °.

### *2.3.2 Microstructural analysis*

To investigate the microstructure of carbonized CNCs, the WAXD and Raman measurements were performed. In WAXD patterns (Figure 2.4a), the SD-D800 and SD-D1000 exhibited the broad two (002) and (10) peaks, indicative of the low degree of structural development. The (002) peak started to shift to right from 800 to 1500 ℃, corresponding that the structural evolution is developed with narrowing interlayer distance from 0.386 to 0.373 nm (Table 2.1) [16, 41]. On the other hand, the SD-D2500 showed two sharper peaks at 26.0 and 26.5° with the broad hump at 25.8°, which is characteristic of partly graphitized hard carbons at high temperature (usually above 3000 ℃) [16, 42, 43]. The d-spacing of SD-D2500 was calculated from broad hump at 25.8° and it is 0.346 nm. Because the minimum interlayer distance for sodium ion insertion between graphene layers is 0.37 nm, the microstructure of SD-D2500 seems to be inappropriate to the sodium ion intercalation [44]. Raman spectra were normalized with the intensity of G-band and the experimental ratio of $I_D/I_G$ ratio is represented in Figure 2.4b. Upon increasing carbonization temperature, G- and D-bands start to appear clearly with the decrease of $I_D/I_G$ ratio and SD-D2500 shows the low $I_D/I_G$ ratio below 1.0. Raman spectra were deconvoluted by peak fitting to closely examine the graphitic structure (Figure 2.5a-d). D-band at around 1350 $cm^{-1}$ is attributed to the disordered graphitic carbon such as edges of graphene layer, and G-band at around 1580 $cm^{-1}$ is assigned to the ordered graphitic carbon [16, 41, 45, 46]. TPA-band (transpolyacetylene band) around 1200 $cm^{-1}$ is attributed to the polyenes (indicative of not hexagonal structure) or ionic impurities [46]. A-band (amorphous band) is assigned to amorphous carbon, which is usually observed in the carbonization at low temperature [46]. Additionally, a small shoulder on the G-band around 1610 $cm^{-1}$ is assigned as the D'-band (It can be observed in only SD-D2500 in Figure 2.5d), which can be observed in the surface of structural developed carbons [46]. In the fitted Raman spectra, $I_D/I_G$ ratio and the percent of amorphous were calculated (Figure 2.6). The percent of amorphous indicates the summation with areas of TPA- and A-band. The SD-D800 and SD-D1000 exhibit the broad D-band with high intensity of TPA- and A-band (Figure 2.5a and 2.5b), indicating the less developed structure as mentioned in XRD. In SD-D1500, the D- and G-bands appear clearly with the decrease of TPA- and A-bands (Figure 2.5c). The high and sharp D-band of SD-D1500 attributes to the higher $I_D/I_G$ ratio of 1.5, which is interpreted as the defects for the intermediate structure before the phase conversion to polycrystalline graphite during the structure evolution of CNC [16]. Further, the $I_D/I_G$ ratio of SD-D2500 is 0.8 with the few amorphous fraction, indicating the developed graphitic structure by partially graphitization as mentioned in XRD (Figure 2.4a).

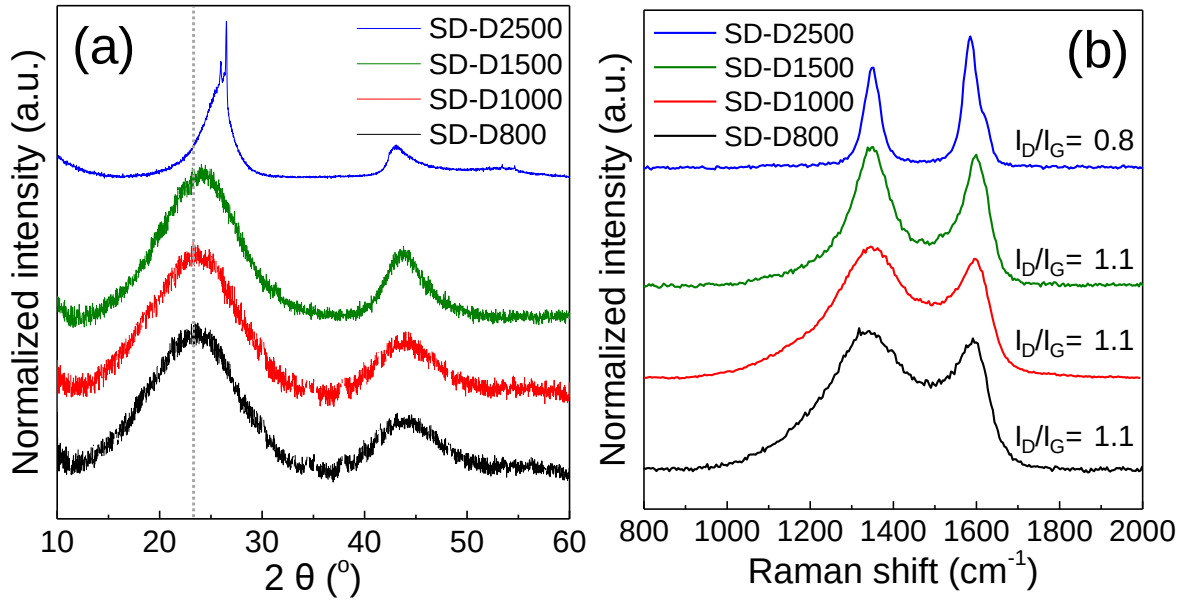


Figure 2.4 (a) WAXD patterns of the carbonized CNCs at various temperatures. The crystalline structure variation gradually takes place up to the carbonization temperature of 1500 ℃, and the highly graphitized structure can only be obtained after heat treatment at 2500 ℃. (b) Raman spectra of carbonized CNCs.

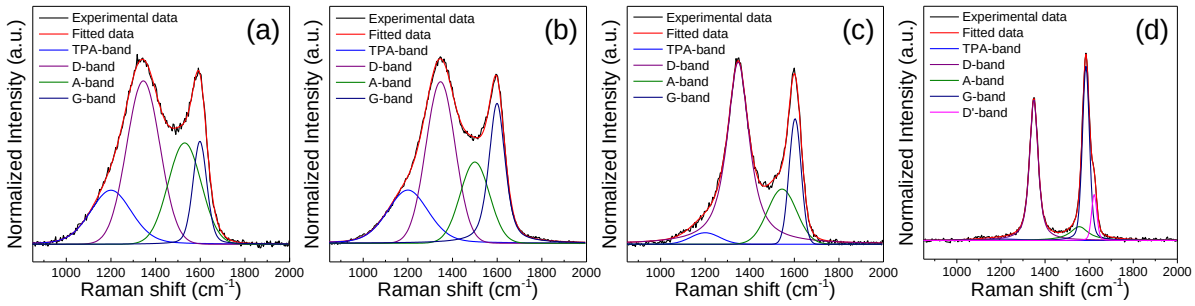


Figure 2.5 (a-d) Raman spectra of the CNCs carbonized at various temperatures and peak deconvolution results. D-band (1350 cm$^{-1}$) and G-band (1580 cm$^{-1}$) are assigned to the disordered and ordered graphitic carbons, respectively. TPA-band (1200 cm$^{-1}$) is attributed to the polyenes or ionic impurities. A-band (1500 cm$^{-1}$) is assigned to amorphous carbon. D'-band (1622 cm$^{-1}$) was also observed for the SD-D2500. The observation of D'-band suggests that highly ordered graphitic structure is formed.

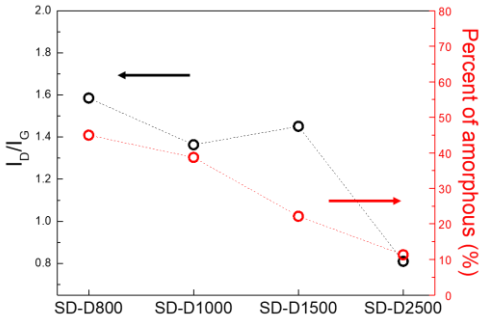


Figure 2.6 The structural parameters characterized by deconvoluting Raman spectra, respectively. Both the D- and G-bands obtained by peak deconvolution became sharp with increasing carbonization temperature as shown in Figure 2.5. The area fraction of amorphous peaks was calculated by dividing the summed area of TPA- and A-band with the total area of all the peaks, indicating the structure development with the removal of less ordered structure as reported elsewhere [16].

To confirm the $sp^2$ carbon of carbonized CNC, X-ray photoelectron spectroscopy (XPS) was performed. Figure 2.7a-d show the survey spectra, and atomic percent is represented in Table 2.1. For SD-D800, the atomic percentage of carbon and oxygen are 62.6% and 19.5%, respectively. The atomic percent of carbon increases with the decrease of heteroatoms with the increase of the carbonization temperature. In the spectra of SD-D800 and SD-D1000 (Figure 2.7a-b), the Na peak is observed due to NaOH which was used for the neutralization during the preparation of CNC [2]. But Na peak is totally removed above 1500 ℃. Carbon 1s spectra are deconvoluted by peak fitting (Figure 2.8a-d) and the calculated results are indicated in Table 2.1 and Figure 2.9. Although the Raman spectra and XRD patterns between SD-D800 and SD-D1000 are similar, there is significant difference in the fraction of $sp^2$ carbon. The carbonization temperature of 800 ℃ is too low to form $sp^2$ carbon. From 1000 ℃, the $sp^2$ carbon is further formed with the reduction of $sp^3$ carbon at higher temperature (Figure 2.9), indicating the conversion of small nano-graphitic structure to the large graphitic structure [16]. The area fraction of oxygen-containing groups, which known to contribute to the adsorption-desorption of sodium, is not significantly changed [26, 47].

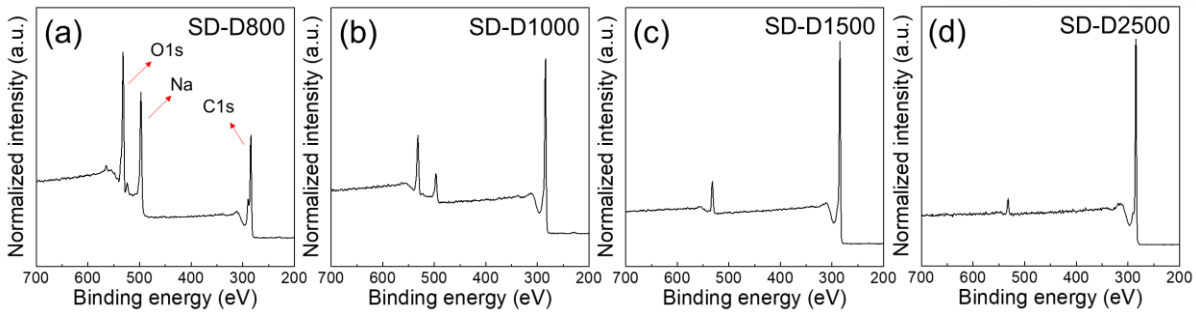


Figure 2.7 X-ray photoelectron spectroscopy (XPS) spectra of SD-D800, SD-D1000, SD-D1500 and SD-D2500, respectively. The Na peak is observed in SD-D800 and SD-D1000, but not in SD-D1500 and SD-D2500, suggesting that the ionic impurity was removed at 1500 ℃.

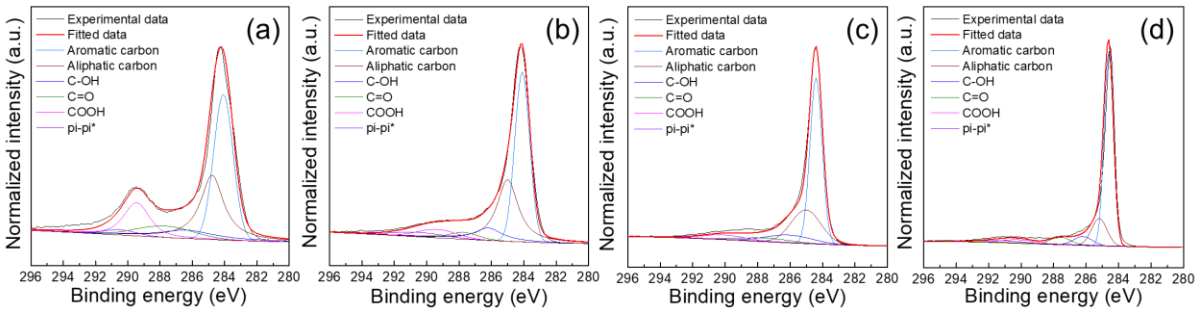


Figure 2.8 C1s XPS spectra of the CNCs carbonized at various temperatures and peak deconvolution results.

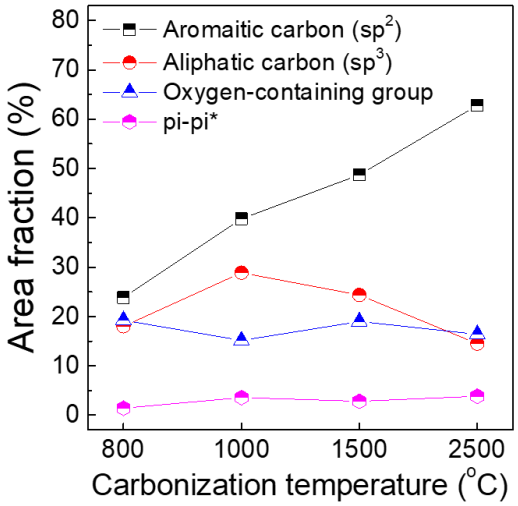


Figure 2.9 The calculated area fraction obtained by deconvoluting C1s XPS spectra of the carbonized CNCs. The atomic percentage of carbon is considered to calculate each area fraction.

The TEM images of carbonized CNCs were represented in Figure 2.10. The SD-D800 shows the nearly amorphous carbon. Although the few-layers stacked structure with only short-range order is partly observed (Figure 2.10a and 2.10e), but it is hard to observe due to the low fraction of $sp^2$ carbon. In the SD-D1000 (Figure 2.10b and 2.10f), the turbostratic structure with an average interlayer distance of about 0.38 nm is observed and contains many defects in the crystals (marked with red circles in Figure 2.10f). It is interesting that SD-D1000 exhibits the long-range-order layered structure like expanded graphite. The appearance of the long-range-order even at low carbonization temperature is attributed to the intrinsically high crystallinity of precursor, unlike other hard carbons which exhibits the only short-range ordered structure [16]. The SD-D1500 has the average d-spacing of 0.37 nm, and the intermediate structure for the fusion of graphitic structure are observed (indicated with red arrow in Figure 2.10c), as mentioned in Raman. Although the crystal structure of SD-D1500 seems to be similar with SD-D1000, SD-D1500 exhibits the relatively low fraction of defects in crystal. The defects serve as active sites that sodium can easily react due to the high binding energy, and facilitate the sodium transfer between graphene layers [48-50]. Therefore, the microstructures of SD-D1000 and SD-D1500 seem to be appropriate for sodium storage. On the other hand, in the TEM images of SD-D2500 (Figure 2.10d and 2.10h), the graphitic structure with the narrow interlayer distance (~0.34 nm) is observed with few defects in crystal due to the graphitization at high temperature, as seen in XRD. The SD-D2500 also exhibits the few layers stacked structure with the d-spacing of 0.37 nm on the only extra-surface of graphitic structure, but it is hard to observe the such structures.

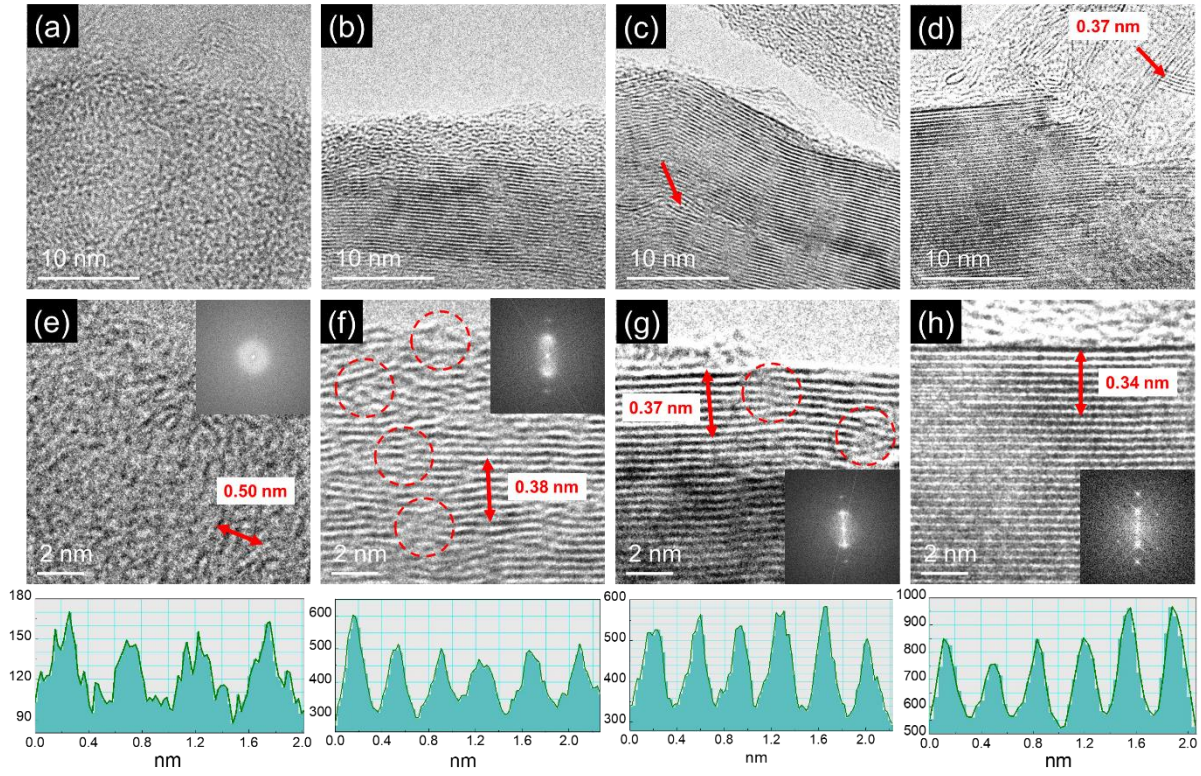


Figure 2.10 High resolution TEM images of (a) SD-D800, (b) SD-D1000, (c) SD-D1500, and (d) SD-D2500, respectively. The red arrow in (c) indicates the intermediate structure before the phase conversion to polycrystalline graphite. The red arrow in (d) represent the few layers stacked structure with the d-spacing of 0.37 nm, which is observed on the surface of graphitic structure. (e-h) The magnified images of (a-d) along with the Fast Fourier Transformation (FFT) and d-spacing images. The double-sided arrows in each image indicate the crystalline layers for the d-spacing calculation. The dashed red circles in figure (f) and (g) indicate defective crystalline sites.

To summarize the microstructure of carbonized CNC, SD-D800 is not considered as the appropriate anode material. Due to the low carbonization temperature, the fraction of oxygen-containing group is relatively high, and the fraction of $sp^2$ carbon is very low (below 25%). The SD-D2500 is also unsuitable anode material for SIB like graphite, because the interspace between graphene layers is too small as well as the low fraction of active sites. On the other hand, SD-D1000 and SD-D1500 seem to have the suitable structure for sodium intercalation between graphene layers and adsorption-desorption of sodium based on the moderate fraction of oxygen-containing groups and the appropriate interlayer distance (above 0.37 nm) as well as defects on the crystals [48-50].

### *2.3.3 Electrochemical performances of* carbonized *CNC*

In order to investigate the sodium storage mechanism of carbonized CNCs, the electrochemical performances were conducted with Na metal half-cells. Figure 2.11a shows the 1st charge-discharge profiles of all carbonized CNCs at 10 mA $g^{-1}$. Figure 2.11b indicates the capacities of each region (the irreversible, sloping above 0.2 V and plateau below 0.2 V, respectively) based on the Figure 2.11a, which is also summarized in Table 2.2. The reversible capacities of each carbonized CNC are 212, 255, 311 and 126 mAh $g^{-1}$, respectively. The irreversible capacity decreases from 111 mAh $g^{-1}$ of SD-D800 to around 50 mAh $g^{-1}$ of SD-D1500 and SD-D2500. During the 1st sodiation process, the electrolyte with $Na^+$ based salt and organic solvent decomposes at the carbon surface, resulting in the formation of SEI layer on the carbon surface [48, 51, 52]. The sodium ions consumed for the formation of SEI layer contribute to the irreversible capacity. Therefore, it is believed that reducing the exposed surface can lower the amount of irreversible sodium ions by reducing the contact area with the electrolyte [31, 33, 53]. In the research of CNC-based film carbonized at 1000 ℃ by Zhu et al., the irreversible capacity of the first cycle at 10 mA $g^{-1}$ is more than 1300 mAh $g^{-1}$ due to the high surface area (146 $m^2$ $g^{-1}$) [17]. On the other hand, the SD-D1000 in the current study, which is carbonized at the same temperature of 1000 ℃, exhibits the low surface area of 9.0 $m^2$ $g^{-1}$, resulting in the low irreversible capacity of 90 mAh $g^{-1}$ (Table 2.1 and Table 2.2). Moreover, the SD-D1500 and SD-D2500 with the lower surface area (6.7 and 1.5 $m^2$ $g^{-1}$, respectively) exhibit the lower irreversible capacities of around 54.8 and 49.3 mAh $g^{-1}$, respectively. Based on this tendency, the spray-dried CNC-based carbon is the best selection for minimal loss of sodium ion during electrochemical reaction. The reversible capacity in sloping region also decreased from 800 to 2500 ℃. With the increase of carbonization temperature, the fractions of heteroatoms and $sp^3$ carbons, which contribute to the defects, decrease as well as the reduction in the surface area and the pore volume. Because of the high binding energy between $Na^+$ and carbon in these structure, the sodium can be adsorbed in these active sites at high sodiation potentials in sloping region [27, 49]. This is related with the surface redox reactions, commonly known as the pseudo-capacitance (dominant in the sloping region) storage mechanism [54]. However, the capacity of plateau region is highest at SD-D1500 (228.4 mAh $g^{-1}$) and suddenly dropped at SD-D2500 (78.3 mAh $g^{-1}$). From 800 to 1500 ℃, the graphitic structure with the average d-spacing above 0.37 nm is developed with the further formation of $sp^2$ carbon, resulting in the increase of the capacity in plateau region. However, the sudden drop of plateau capacity of SD-D2500 is attributed to the inappropriate interlayer distance (~0.35 nm) for sodium intercalation by graphitization [26, 44]. Therefore, the sodium ion storage by the insertion between graphene layers contributes to the plateau region [34, 44, 49]. The higher initial coulombic efficiency (ICE) tends to increase with the increasing capacity of the plateau region not sloping region. Because the sloping region is related to the surface redox reactions, which might contribute to the further formation of SEI layers, but the plateau region is attributed to sodium storage in the inner structure of

carbon. Therefore, the SD-D1500, which the plateau region is dominant, exhibits the highest ICE of 85%. For the carbonized CNC-based anode, the high ICE of SD-D1500 is achieved to the collaboration effect with the low surface area and the graphitic structure, which can contribute to the plateau region.

The rate performance for evaluating the kinetic feasibility of SD-D1000 and SD-D1500 is also illustrated in figure 2.11c. Both exhibit the outstanding rate capability without a large capacity fading. At the current density of 20 mA $g^{-1}$, SD-D1000 and SD-D1500 show the reversible capacities of 250 mAh $g^{-1}$and 302 mAh $g^{-1}$, respectively. After high currencies, the C1000 and C1500 anodes recover the reversible specific capacities of 244 and 294 mAh $g^{-1}$ with the capacity fading of about 2.4 and 2.6%, respectively. Especially SD-D1500 shows superior rate capability at various current densities, which delivers the charge capacities of 301, 295, 286, 278 and 274 mAh $g^{-1}$ for current densities of 20, 50, 100, 200 and 400 mA $g^{-1}$, respectively. Based on the electrochemical performances, the carbonized CNC at 1500 ℃ is the best high-performance anode material among the carbonized CNCs. Figure 2.11 shows the voltage profiles of SD-D1500 at each current rate. The long plateau region is maintained despite the higher current density, which indicate that SD-D1500 will also have the high-energy for the full cell due to the low average oxidation voltage in the range of 0.25 – 0.37 V. Long term cycling performance of SD-D1500 at 100 mA $g^{-1}$ was performed for 500 cycles in figure 2.11e. At the current density of 100 mA $g^{-1}$, it delivers the 290 mAh $g^{-1}$ without capacity fading with CE of nearly 100% over 500 cycles. SD-D1500 exhibit the outstanding capacity retention of 98.3% over 200 cycles, and 92% over 500 cycles. Above results prove that SD-D1500 shows the excellent cycle stability as the anode material for SIB.

Table 2.2 The calculated capacity during the first discharge/charge reactions at 10 mA $g^{-1}$. The plateau region and sloping region distinguished below/above 0.2 V in galvanostatic charge/discharge curve.

| | Discharging capacity (mAh $g^{-1}$) | Charging capacity (mAh $g^{-1}$) | Irreversible capacity (mAh $g^{-1}$) | Plateau region (mAh $g^{-1}$) | Sloping region (mAh $g^{-1}$) | Coulombic efficiency (%) |
|---|---|---|---|---|---|---|
| C800 | 323.1 | 211.8 | 111.2 | 79.0 | 132.8 | 65.6 |
| C1000 | 344.9 | 255.0 | 89.8 | 133.4 | 121.7 | 74.0 |
| C1500 | 365.4 | 310.6 | 54.8 | 228.4 | 82.2 | 85.0 |
| C2500 | 175.1 | 125.8 | 49.3 | 78.3 | 47.4 | 71.8 |

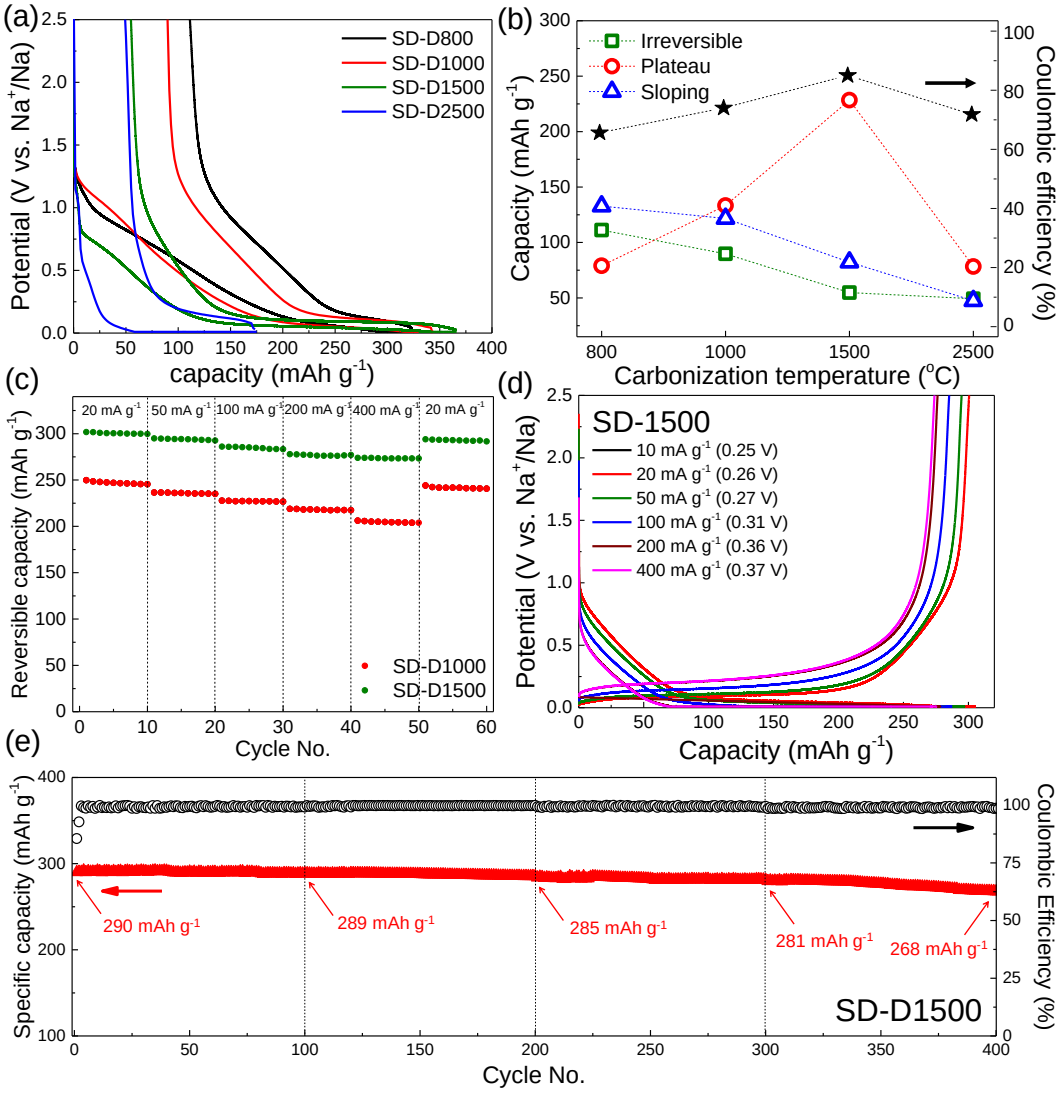


Figure 2.11 Electrochemical properties of the carbonized CNC-based anodes. The specific capacities of the anodes are calculated based on the weight fraction of the CNC on the electrode. (a) Galvanostatic charge/discharge curves of the carbonized CNC-based anodes at the current density of 10 mA $g^{-1}$. (b) Plot of irreversible capacity, sloping region (above 0.2 V), plateau region (below 0.2 V) and coulombic efficiency as a function of carbonization temperature from the voltage profiles of (a). (c) Rate capability test of the carbonized CNC-based anodes was performed at the current densities of 20, 50, 100, 200 and 400 mA $g^{-1}$. SD-D1000 and SD-D1500 show the reversible recovery at 20 mA $g^{-1}$ without capacity loss. The SD-D1500 shows the high reversible capacity of 274 mAh $g^{-1}$ at 400 mA $g^{-1}$ of high current density with few capacity fading, indicating the excellent rate capability. (d) Voltage profiles of the SD-D1500 at various current densities, showing that even at high current density, the capacity fading was marginal, and the long plateau region was maintained. (e) Cycling performance at 100 mA $g^{-1}$ of current density and its corresponding coulombic efficiency (CE) of SD-D1500 anode for 500 cycles.

Based on the electrochemical performances with the microstructure of carbonized CNCs, “adsorption-intercalation” mechanism can be verified, which the plateau region refers the sodium intercalation into the graphitic layers and the sloping region indicates the defects and nanopores on the surface of carbonized CNC [27, 49]. The detailed schematic is illustrated in the Figure 2.12a. The *ex-situ* Raman spectroscopy study was conducted after sodiation (0.01 V)/desodiation (2.5 V) to examine the reversibility of graphitic structure of carbonized CNCs. In the Figure 2.12b and 2.12c, SD-D1000 and SD-D1500 showed the slight decrease of intensity and red-shift of D-band with different extent after sodiation, since $Na^+$ occupies the defects of such as the pores, edge and surface of graphene [55, 56]. Also, both of SD-D1000 and SD-D1500 exhibited the red shift of G-band due to the weaken of resonance by sodium intercalation [55, 56]. Moreover, the structure recovery of both are excellent after desodiation. However, SD-D2500 did not show the peak shift of G-band, suggesting that the majority of the specific capacity of the C2500 is originated by Na ion adsorption (Figure 2.12d). In figure 2.12d, it is interesting that D’-band, which is only observed in SD-D2500, becomes faint after sodiation (red arrow) and is not recoved after desodiation due to the weaken vibration of the graphene surface by the formation of SEI layer. The position and intensity of the D- and G-band are recovered after desodiation, which also indicates that the good reversibility of the materials.

To summarize, the electrochemical properties are varied with the carbonization temp0erature of carbonized CNCs. From SD-D800 to SD-D2500, the microstructures with high binding energy such as defects and pores decreased, resulting in the reduction of the capacity at high sodiation potential. The capacity at low potential is attributed to the sodium intercalation and expanded up to 1500 ℃ with the increase of $sp^2$ carbon and the structural development. However, the dropped capacity at low potential is observed at SD-D2500, because the high temperature of 2500 ℃ induces the partly graphitization, resulting in the narrow interlayer distance. These results suggest that the appropriate carbonization temperature is important to produce the suitable carbon anode materials with the suitable microstructures.

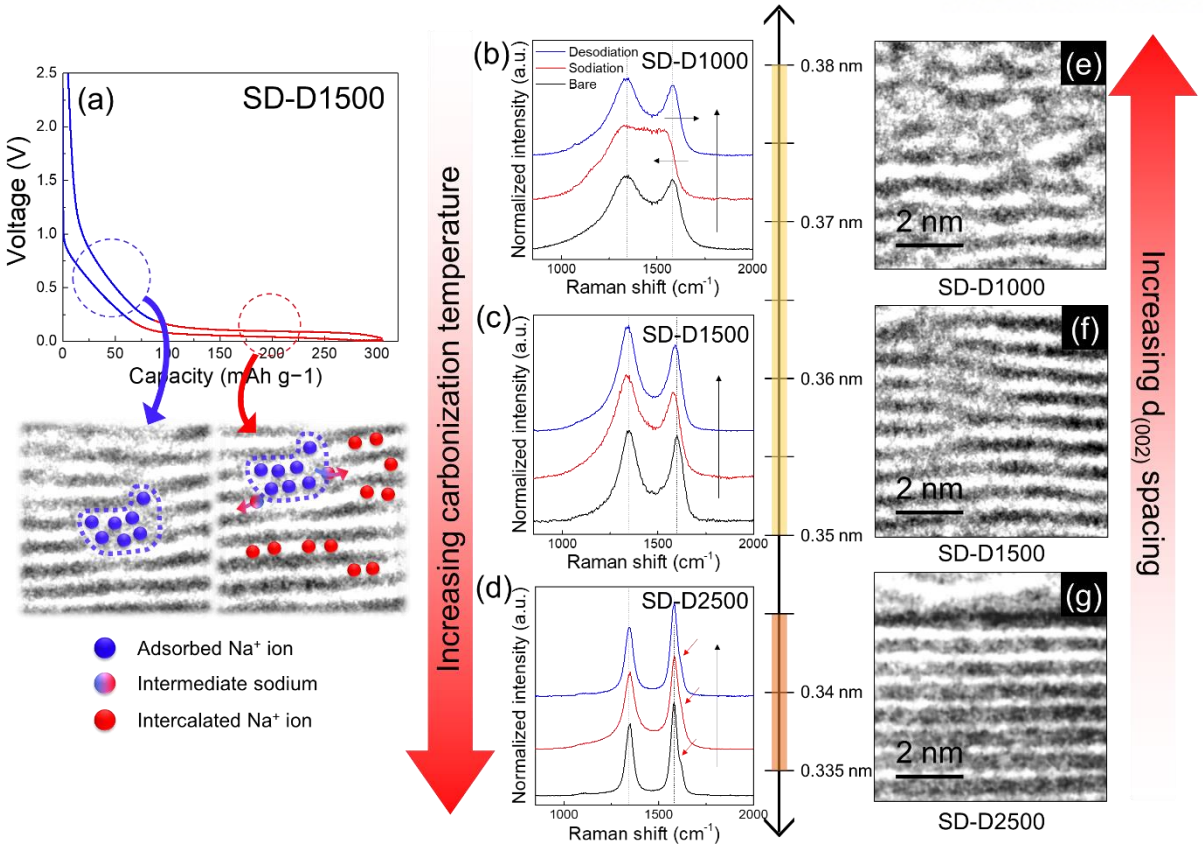


Figure 2.12 (a) Galvanostatic charge/discharge curve of SD-D1500 and schematic description of Na ion adsorption-intercalation mechanism, where the blue and red curves represent adsorption and intercalation of Na ions as sloping and plateau regions, respectively. (b)-(d) ex-situ Raman spectra of bare and cycled CNC anode at different carbonization temperatures, indicating that the Raman peaks of SD-D1000 and SD-D1500 are broadened and shifted to lower wave number upon sodiation. This suggests the effective Na ion intercalation takes place for those anodes. The structure reversibility was also confirmed by ex-situ Raman spectra after desodiation. However, SD-D2500 showed little change in peak positions, suggesting the limited intercalation of Na ions. (e)-(f) TEM images of the carbonized CNCs showing the temperature dependence of the carbon structure development.

## 2.4 Conclusion.

To prepare the high-performance anode material for SIB, spray-dried CNCs were selected as carbon precursor derived from cellulose, which is the most abundant biopolymer. Microstructures of carbonized CNCs are tunable with the carbonization temperature from 800 to 2500 ℃, and directly affects the sodium storage behaviors. The carbonized CNCs except SD-D800 exhibit the low surface area (below 10 $m^2 g^{-1}$) due to the originally low surface area (0.7 $m^2 g^{-1}$) of spray-dried CNCs, resulting in the low irreversible capacity. The decrease of sloping region is attributed to the decrease of structural parameters such as the pores, defects and heteroatoms at the higher temperature. However, plateau region increases up to 1500 ℃ because the long-range ordered structure with d-spacing above 0.37 nm is further developed. Besides, the plateau region is suddenly dropped at 2500 ℃ due to the narrow d-spacing (~ 0.35 nm) by graphitization. Therefore, it is concluded that carbonized CNCs follow "adsorption-intercalation" mechanism. Among various carbonized CNCs, SD-D1500 delivers the highest reversible capacity of 311 mAh $g^{-1}$ at 10 mA $g^{-1}$ with the highest initial coulombic efficiency of 85%. Also, it shows the excellent rate performance, which is the 274 mAh $g^{-1}$ at 400 mA $g^{-1}$ and outstanding long cycle stability. Therefore, the carbonized CNC is the best choice for anode material for SIBs that obtained from the minimal process with low-cost. This study suggests that selecting appropriate materials is important for realistic performance as well as understanding the correlation between the microstructure and electrochemical properties.

# Chapter 3. Effects of drying method and structural evolution mechanism of freeze-dried cellulose nanocrystals during carbonization

## 3.1 Introduction

Cellulose is the most abundant biopolymer available on the earth and it can be extracted from various sources such as tunicate, algae, bacteria, fungi as well as plants and woods [1, 2]. By removing the amorphous region of cellulose through the acid hydrolysis, cellulose nanocrystals (CNCs) are produced which have unique structural features such as high crystallinity (54-88%), nanoscale dimensions with rod-shape, high thermal stability and well-ordered crystal structure [1, 2]. Based on these superior properties, CNC has been widely used in many application fields, especially as nanofillers for polymer nanocomposites [3-6]. Further, there have been many attempts to use CNC as a precursor for carbon materials including carbon nanofillers because it shows highly crystallized carbon crystals even from the low-temperature carbonization due to the intrinsically ordered structure [16-18]. Eom et al. observed the ordered carbon structures maintaining the rod shape of pristine CNC after 1000 °C carbonization [16]. Zhu et al. also observed the long-range ordered carbon crystals from carbonization of CNC at 1000 °C, but the crystalline structures were not found when carbonizing regular cellulose fibers [17]. In addition, Kim et al. suggested that the carbonization of cellulose with high crystallinity resulted in more developed carbon structures [57]. However, most of the fundamental researches on thermal conversion of cellulosic materials including CNCs have been focused on the chemical decomposition, depolymerization, and the formation of ladder structure, which occurs at low temperatures below 800 °C as compared to the carbonization reaction [17-19]. Although the study of structural evolution of CNC during carbonization is still limited, it is a prerequisite to tailor the CNC-based carbon structures for desired properties.

The macroscopic morphology of CNCs is tunable by drying methods after acid hydrolysis based on the intermolecular hydrogen bonding between many hydroxyl groups on their surface. There are two representative drying methods to produce pristine CNCs: spray-drying and freeze-drying. The spray-dried CNCs (SD-CNCs) exhibit an aggregated ellipsoidal morphology in micro-scale and have low surface area because CNC domains become shrank by capillary force as they are dried with hot air gas during spray-drying [36, 37]. On the other hand, the freeze-dried CNC (FD-CNCs) shows branched morphology with high surface area and high free volume, which the porous network of CNCs is formed by the removal of solvent below triple points during freeze-drying [36, 37]. Noticeably, their macroscopic morphology is maintained even after the stabilization or carbonization process [16-18]. Hence, FD-CNCs are more considered than SD-CNCs as the promising precursor for carbon nanofillers because they are expected to have higher dispersibility in solvents and higher interaction with polymer matrix based on

the difference in a surface area [58, 59]. Further, heat can be applied more evenly on the FD-CNCs during carbonization, leading to the uniform microstructure of carbon. As such, the degree of structural conversion can vary depending on the morphology of pristine state. Therefore, the carbonization study about the structural development of FD-CNCs is needed following that of SD-CNCs in our previous paper [16].

In the current study, we carbonized FD-CNCs, which are in not aggregated morphology, unlike SD-CNCs, in the range of 1000-1500 °C to trace the structural evolution mechanism. Further, the oxidative stabilization was performed or not before carbonization to determine the effects of stabilization on the change of structure or morphology. This study will provide the fundamental research on how to tailor the carbon structure of FD-CNCs with respect to the carbonization temperature and an understanding of how the structural development of carbonized CNCs differs by morphologies in the precursor.

## 3.2 Experimental

### *3.2.1 Materials*

Spray-dried CNC was purchased from Celluforce Co. DI water and N,N-Dimethylformamide (DMF) from SamChun Company were used as a solvent.

### *3.2.2 Preparation of freeze-dried CNC*

The spray-dried CNC powders were dried at 65 ºC overnight under vacuum prior to use. For the effect of the concentration on the morphology, 20 mg and 200 mg CNC were dispersed in 20 ml DI water with concentration 0.1 and 1.0 wt.% by sonication. For freezing aqueous suspension with liquid nitrogen, various injection methods were applied such as pouring, using syringe and needle with/without nitrogen pressure, and conventional spray gun, finally air atomizing spray nozzle with pressure. The frozen CNC particles were collected in conical tube and then freeze-dried for 72 hours using freeze-dryer equipment (FDB-5502, OPERON Co.).

### *3.2.3 carbonization of freeze-dried CNC*

For the microstructural evolution of freeze-dried CNC, carbonization process was performed with pristine and stabilized FDCNC. Freeze-dried CNC was placed in a custom-made graphite crucible and carbonized as followed. First of all, for oxidative stabilization, FDCNC was stabilized at 250 ºC for 1 hour at a heating rate 5 ºC/min. And then, pristine and stabilized FDCNC were carbonized at 1000-2500 ºC. The carbonized CNCs with/without oxidative stabilization were coded as ‘FD-SX’ and ‘FD-

DX' ('S' and 'D' mean carbonization after stabilization and direct carbonization, respectively. 'X' indicates the final carbonization temperature.). For example, the carbonized CNC at 2500 °C without stabilization is called FD-D2500. To distinguish with the carbonized as-received CNC which is spray-dried, FD was added into their code names.

### *3.2.4 Characterization*

The morphology of the freeze-dried CNC (FD-CNC) and carbonized CNC was observed using scanning electron microscopy (SEM, Novanano230, FEI Co.) at an accelerating voltage of 10 kV. The samples were placed on carbon tape and coated with platinum at 20 mA for 45 s. The SEM images were analyzed and processed by image J.

The microstructure of CNC and carbonized CNCs was examined by a high-resolution transmission electron microscopy (HRTEM, JEM-2100. JEOL) operated at 200 kV accelerating voltage. The TEM images were analyzed and processed by the Digital-Micrograph tool.

Raman spectra was recorded using an Alpha 300s micro Raman spectrometer (WITec) from 10 sites of carbonized CNC and was averaged over 100 scans. The excitation wavelength was 532 nm (laser power is 0.500 mV). Raman curve fitting for the determination of spectral parameter was performed with the Peakfit software package supplied by Sigmaplot as same peak fitting condition as mentioned in the previous paper.

X-ray diffraction (XRD) analysis (Rigaku, D/MAX2500V/PC) with Cu-Kα radiation (λ=1.540598 Å). The 2 θ angle was varied from 10 o to 60 o with a step size of 0.02 o and scan speed 0.8 at voltage 40 kV and current 200 mA.

Brunauer-Emmett-Teller (BET) tests were performed on BELSORP-max (BEL Japan Inc., Japan) with $N_2$ adsoption-desorption isotherms to investigate the surface area. The pore size distributions were calculated by Barret-Joyer-Halenda (BJH) model.

## 3.3 Results and discussion

### *3.3.1 Morphology control of cellulose nanocrystals by freeze drying*

The as-received CNC used in this study was prepared by spray drying. During spray drying, the CNCs are aggregated and shrank due to the capillary forces, resulting in densely aggregated morphology macroscopically with micron size (Figure 3.1). Additionally, since the sulfate group is induced on the surface of CNC due to the use of sulfuric acid for acid hydrolysis during the preparation of CNC, the dispersed state of CNC can be stable in DI water by the formation of electrical double layer. The morphology of CNC can be controlled by the drying process after dispersion of CNC in solvent. To fix the state of dispersed CNC, the freeze drying should be performed and the process is consisted of following three steps. The aqueous suspension is injected into liquid nitrogen ($LN_2$) by various technique (step 1-injection) and, is frozen immediately (step 2-freezing), followed by the removal of only solvent (step 3-freeze drying). After drying, the space where the solvent occupied remains as pores, resulting in the formation of porous network particles. The morphology of CNC can be changed depending on the concentration, dispersed state and injection technique. In the current study, the two different concentrations of 0.1 and 1.0 wt.% were selected to examine the effect of solid concentration on the morphology of CNC. At each concentration, the difference in morphology by sonication condition (dispersed state) was investigated. The five injection techniques were also applied for freezing step. (It is illustrated in figure 3.2)

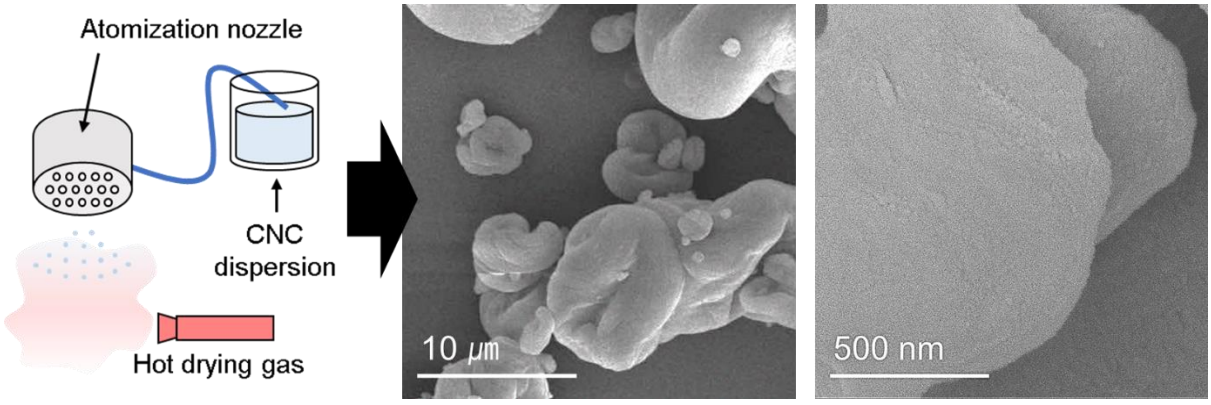


Figure 3.1 Spray-drying method and SEM images of spray-dried CNC (low and high mag), respectively.

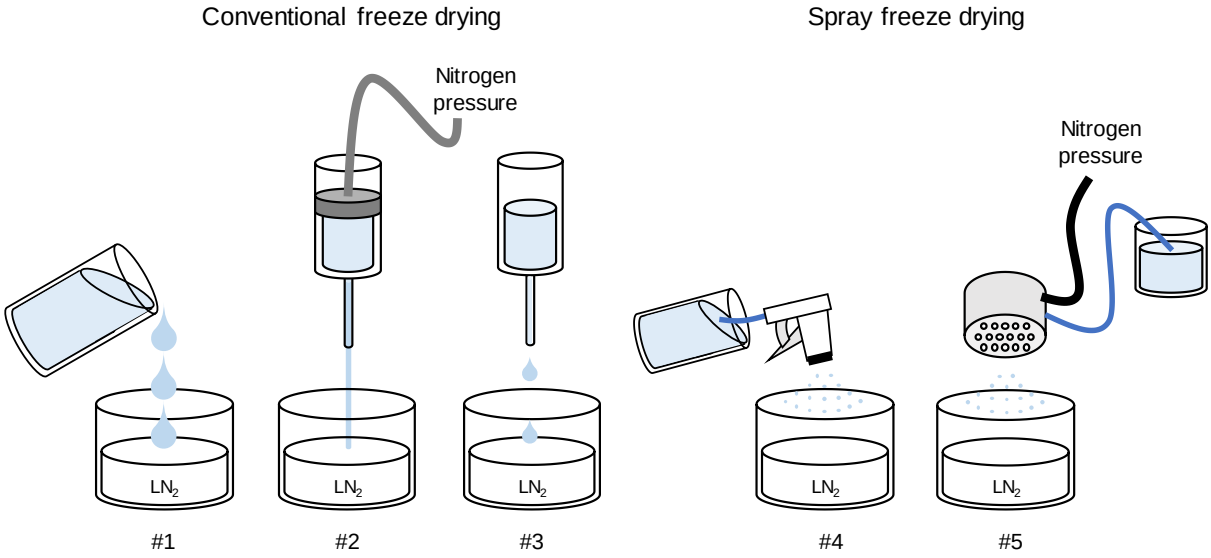


Figure 3.2 The applied injection methods to freeze CNC dispersion using the liquid nitrogen ($LN_2$). #1: Irregularly pouring the dispersion, #2: Injection using the syringe and needle with nitrogen pressure (fast injection), #3: Injection using the syringe and needle without nitrogen pressure (slow injection with the formation of droplet), #4: spray freeze drying using the conventional spray gun (resulting in irregular droplet size), #5: spray freeze drying using the air atomizing spray nozzle with nitrogen pressure (resulting in regular droplet size).

First, the effect of sonication time and type on the morphology was investigated with 0.1 wt.% aqueous suspension. The directly pouring aqueous suspension into $LN_2$ (injection technique #1) was applied as the injection method. The conditions of sonication time and type are summarized in table 3.1. There seems to be no significant difference in the morphologies of four SEM images with naked eye, even in the case of long sonication time (Figure 3.3). The agglomerate morphologies such as nanofibers with diameter of 200-300 nm as well as sheets are observed in four SEM images. Sonication time dose not have strong influence into the resulting morphology, and irregular pouring method can't produce the individual CNCs.

Table 3.1 The sonication condition to obtain the freeze-dried CNC by freezing method #1 with 0.1 wt.%.

| Freezing method | Concentration (wt.%) | Sonication type and time | Observed morphologies |
|---|---|---|---|
| #1 | 0.1 | Bath-type sonication for 24 hours, followed by horn-type sonication for 4 hours. | Nanofibers Sheets |
| #1 | 0.1 | Bath-type sonication for 48 hours, followed by horn-type sonication for 4 hours. | Nanofibers Sheets |
| #1 | 0.1 | Bath-type sonication for 24 hours, followed by horn-type sonication for 5 hours. | Nanofibers Sheets |
| #1 | 0.1 | Bath-type sonication for 144 hours, followed by horn-type sonication for 8 hours. | Nanoparticles Nanofibers Sheets |

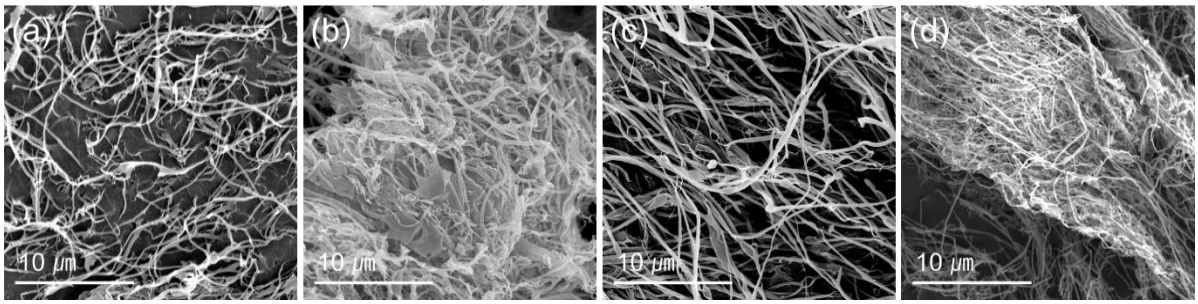


Figure 3.3 The SEM images of freeze-dried CNC obtained by the indicated method in table 3.1.

Second, various injection techniques were applied to investigate the influence of injection method with 0.1 wt.% aqueous suspension (Table 3.2). The syringe with/without $N_2$ pressure was used as an injection method (injection technique #2 and #3), resulting in the fast stream and slow drop of water, respectively. It leads to the time difference from the dispersion to the contact with $LN_2$ for freezing. The CNC nanoparticles can be observed using injection technique #2 (Figure 3.4a). However, using the method #3 (Figure 3.4b), and fibrous sheets are observed dominantly instead of nanoparticles, even the same sonication time. Due to the absence of nitrogen pressure, it takes longer time that droplet is formed at tip of needle. Thus, CNCs can aggregate already in syringe before being dropped into $LN_2$. The spray freeze drying using the conventional spray was also used for freezing, which produces the fast formation of droplets (injection technique #4). After spray freeze drying, the nanoparticle morphologies are obtained although the aggregate morphologies also observed (Figure 3.4c-d). The above results indicate that the injection technique is the most important factor instead of the sonication condition. Even if the sonication time is reduced, CNC nanoparticles are also observed using the freezing technique with the fast injection (Figure 3.4a, and 3.4c-d). It suggests that the nanoparticles can be obtained by the fast injection method which produces the further dispersed particle during injection due to the absence of the time for the aggregation.

Table 3.2 The sonication condition to obtain the freeze-dried CNC by various freezing methods with 0.1 wt.%.

| Freezing method | Sonication type and time | Observed morphologies |
|---|---|---|
| #2 | Bath-type sonication for 64 hours, followed by horn-type sonication for 8 hours. | Nanoparticles<br>Nanofibers<br>Sheets |
| #3 | Bath-type sonication for 64 hours, followed by horn-type sonication for 8 hours. | Nanofibers<br>Sheets |
| #2 | Bath-type sonication for 16 hours, followed by horn-type sonication for 8 hours. | Nanoparticles<br>Nanofibers<br>Sheets |
| #4 | Bath-type sonication for 16 hours, followed by horn-type sonication for 8 hours. | Nanoparticles<br>Nanofibers<br>Sheets |

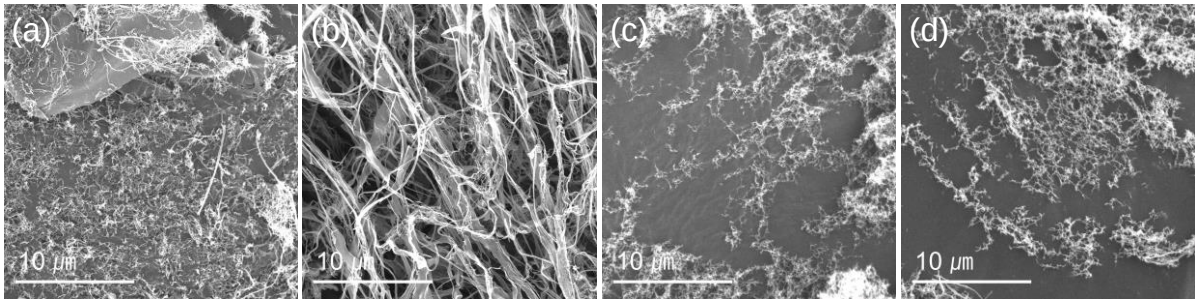


Figure 3.4 The SEM images of freeze-dried CNC obtained by the indicated method in table 3.2.

To increase yield of freeze-dried CNC, the concentration of CNC is increased up to 1.0 wt.% and dispersed, followed by freezing with the technique #4 (Figure 3.5a-b). The nanoparticles are observed (Figure 3.5c) as shown in SEM image of 0.1 wt.%. However, the aggregated morphologies such as nanofibers and sheets are also observed, and it seems due to the irregular droplet size not the sonication time. However, in figure 3.5b, the outer-morphologies of droplets with similar size are different each other. The morphologies of freeze-dried CNC depending on the sonication time are represented in figure 3.6. In the SEM images which show the nanoparticles, there are no differences. Therefore, the regular spray freezing method should be required to avoid irregular morphologies. Using the spray nozzle with nitrogen pressure (atomization), the droplets with regular and smaller size can be

sprayed (injection technique #5). With only 2 hours of sonication times using bath-type sonicator, the nanoparticles with the average diameter of 30.5 ± 7.6 nm in the microporous network is observed (Figure 3.7). The average diameter of CNCs examined in this study is 23.9 nm, suggesting that the individual CNC nanoparticles are obtained. Even though there are many functional groups on the surface of CNCs, they can be individually separated without aggregation by freeze-drying.

To summary, in the manufacturing process of CNC powder, the CNC can have different morphology depending on the drying methods after acid hydrolysis, which the two representative drying methods are spray-drying and freeze-drying [12]. Spray-drying is a method of evaporating the solvent of the CNC dispersion by hot drying gas. In this process, the CNCs become aggregated by capillary force, resulting in a compact and dense morphology. On the other hand, freeze-drying can maintain the dispersed state of CNC and minimize their aggregation by removing the solvent in the frozen state under liquid nitrogen about -196 °C. Thus, FD-CNCs have branched network morphology with high free-volume. Also, the dispersed CNC nanoparticles can be obtained from the aqueous suspension of even 1.0 wt.%, and the freezing technique is the most important factor to achieve the regular nanoparticle morphologies of CNC. The obtained spray freeze-dried CNC with technique #5 is coded as FD-CNC from next section.

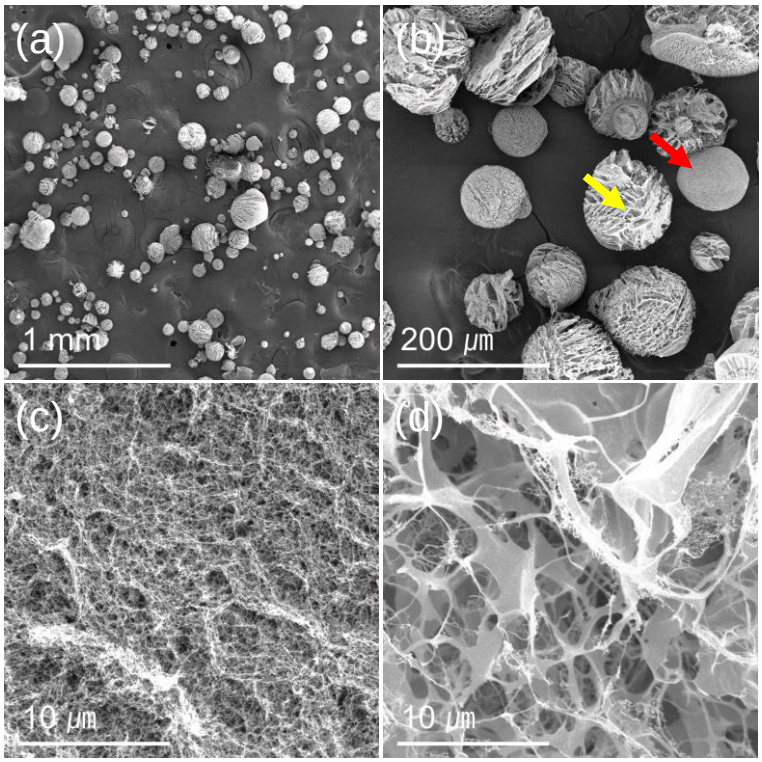


Figure 3.5 The SEM images of spray freeze-dried CNC obtained from 1.0 wt.%. (a) Low mag image, (b) the enlarged image, (c) the red arrow, and (d) the yellow arrow, respectively.

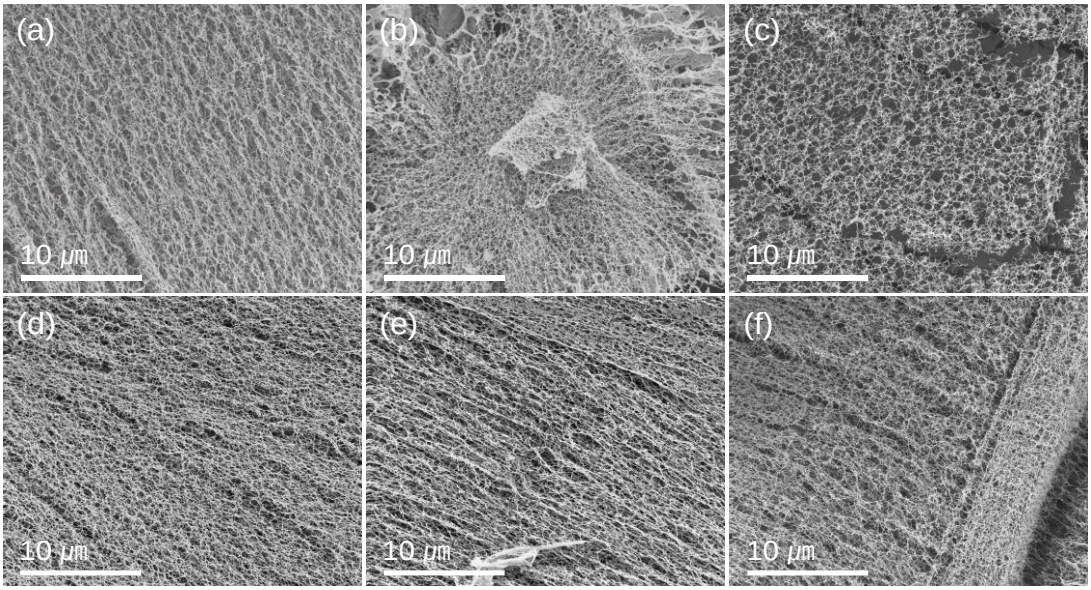


Figure 3.6 The SEM images of spray freeze-dried CNC obtained from 1.0 wt.% with various sonication times. (a) bath 2 hours, (b) bath 4 hours, (c) bath 6 hours (d) horn 2 hours, (e) horn 4 hours, (f) horn 6 hour, respectively.

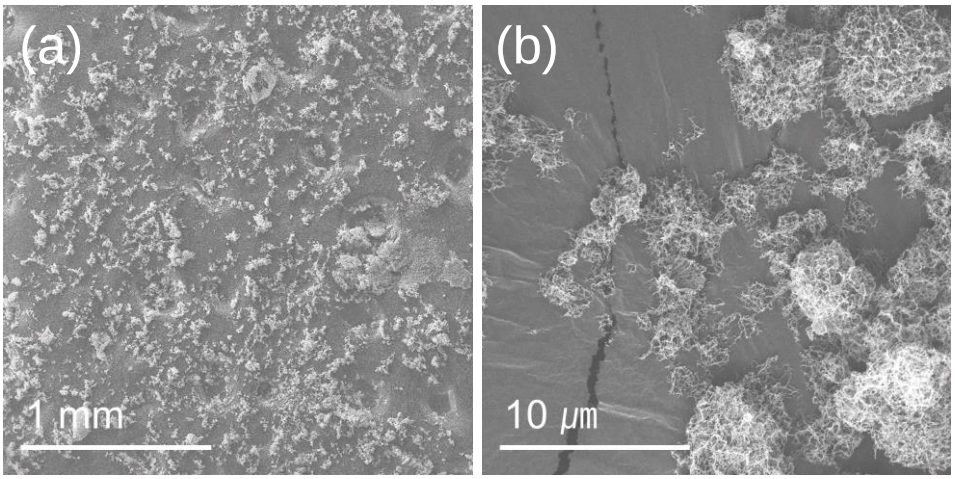


Figure 3.7 The SEM images of spray freeze-dried CNC obtained from 1.0 wt.% using spray nozzle.

### *3.3.2 Structural evolution of freeze-dried CNCs during carbonization*

Figure 3.8 and Figure 3.9 show the SEM images of pristine, stabilized and carbonized SD- and FD-CNCs, respectively. The macroscopic morphology of each CNC, dried by different methods, was preserved even after carbonization regardless of whether the oxidative stabilization was carried out or not. However, it is important to note that large pores were observed on the surface of the carbonized SD-CNCs. This is because of the emission of the volatiles from the inside of the SD-CNC agglomerates, which were formed by dehydration and depolymerization, especially above 300 °C [38, 39]. Whereas, carbonized FD-CNCs didn't show such pores on their surface since volatiles can be flown out easily due to their not aggregated morphology and high surface area. All carbonized FD-CNCs are represented in figure 3.10.

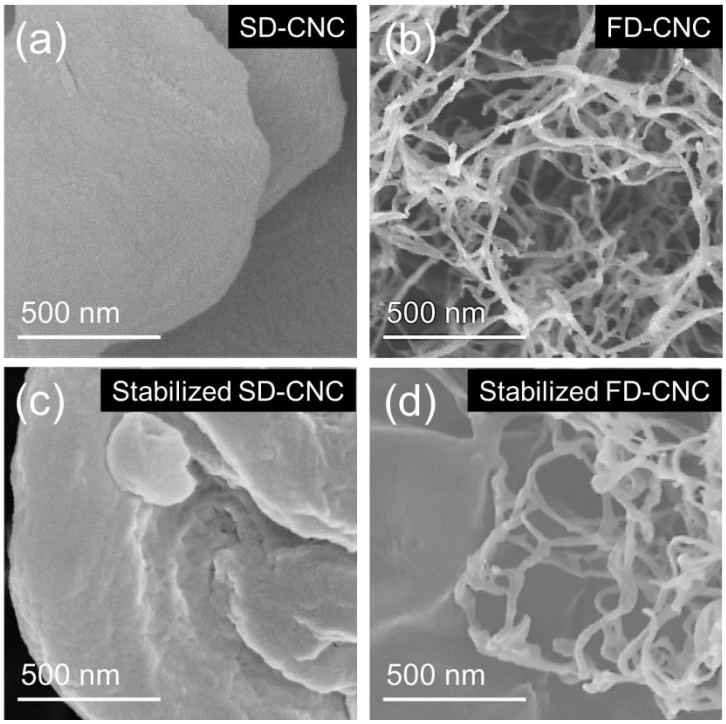


Figure 3.8 SEM images of (a) pristine SD- and (b) FD-CNCs, (c) SD- and (d) FD-CNCs after stabilization for 1 h under air.

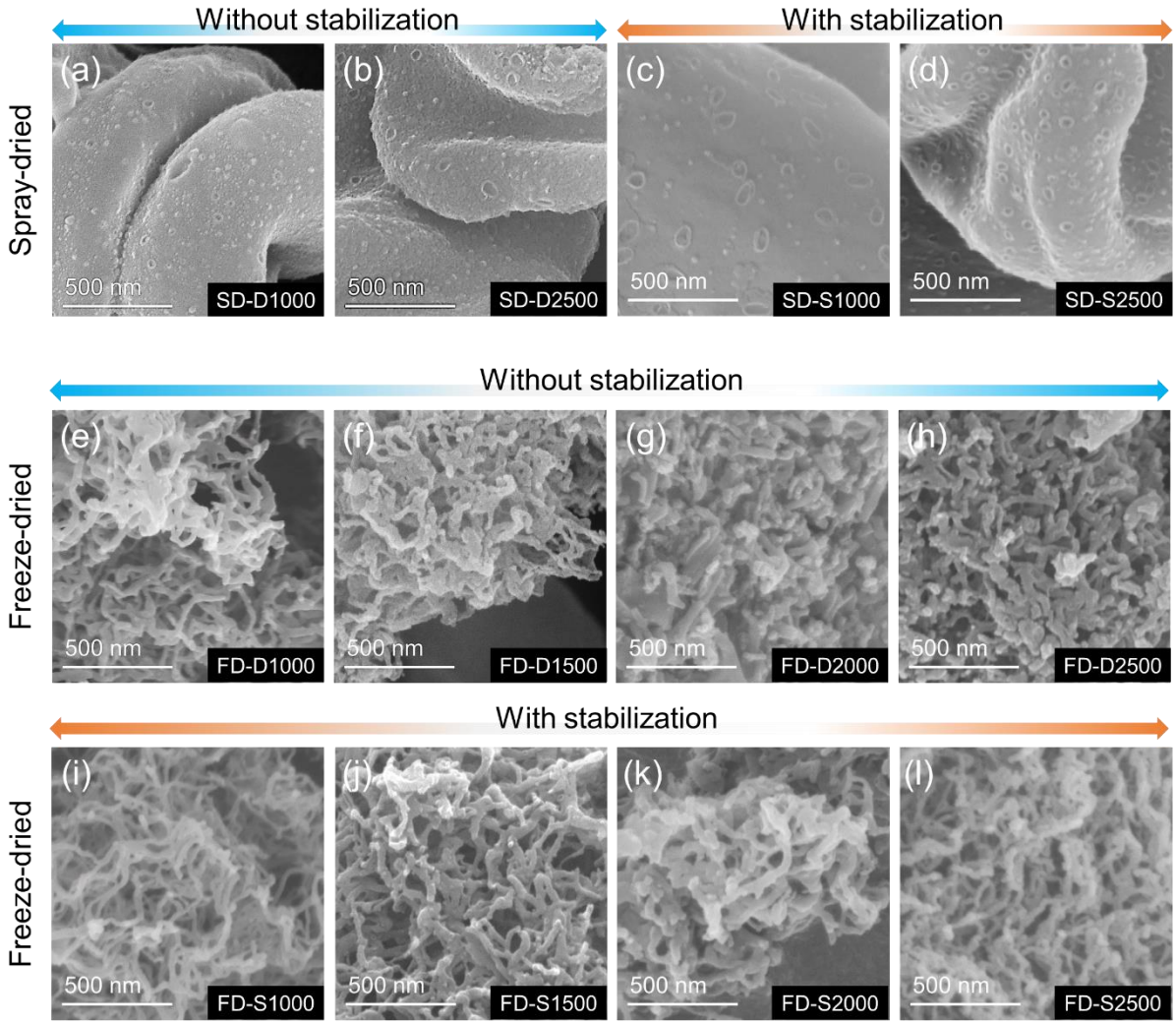


Figure 3.9 SEM images of (a-d) SD- and (e-l) FD-CNCs after carbonization with or without stabilization process.

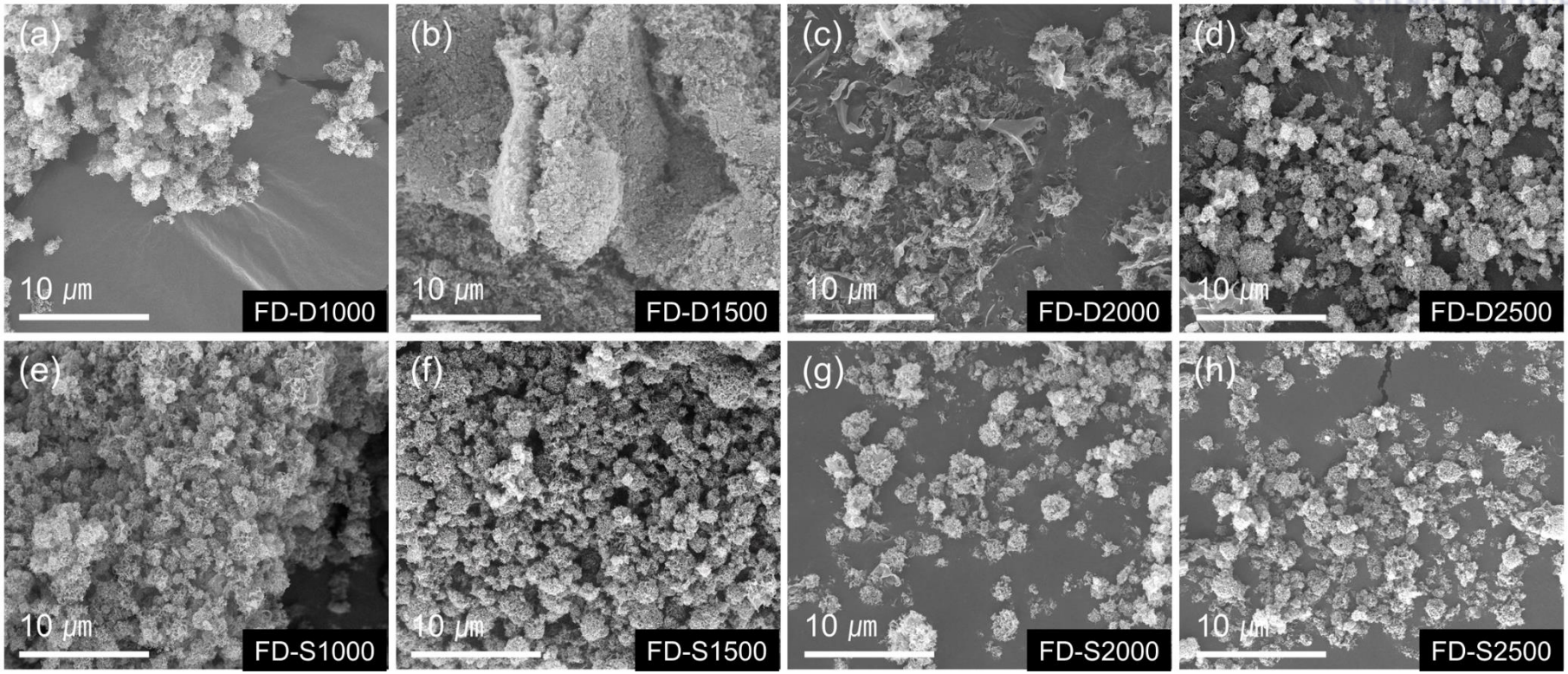


Figure 3.10 SEM images of carbonized FD-CNCs with log mag.

$N_2$ adsorption-desorption measurements were also performed to estimate the surface area and pore size distributions by BET and BJH models (Figure 3.11 and Table 3.3). FD-CNCs have the 336 times higher surface area and the 276 times higher pore volume than SD-CNCs, which is consistent with their morphology and the degree of aggregation (Figure 3.9a and 3.9e). Further, there is a difference of 36.1 and 117.1 times in surface area after direct carbonization at 1000 and 2500 °C, respectively (Figure 3.9b and 3.9h). For both SD- and FD-CNCs, the surface area increased after carbonization, and the pore diameter decreased by carbonization at 1000 °C, since many small pores were generated on their surface by the volatiles. At higher carbonization temperatures, the surface area decreased again as carbon structure develops and crystal density increases. Notably, the pore volume of FD-CNCs continuously decreased with carbonization, unlike the SD-CNCs. This is due to the large effects of heat-induced fusion between adjacent small-sized carbon domains of FD-CNCs [40]. In comparison, that effect is very slight in SD-CNCs because of the inherently agglomerated state. However, despite the high degree of fusion, the surface area and pore volume were still much higher for FD-CNCs as pristine morphology was maintained. For nanocomposites, it is well known that the high surface area of nanofillers is favorable for the dispersion in solution and formation of interphase with polymer matrix [58, 59]. As the morphology and surface area of CNCs depend on drying methods even after carbonization, it is expected that FD-CNC will be more efficient to be used as nanofiller or precursor for nano-fibrous carbon filler. Therefore, the structural evolution mechanism of FD-CNCs during carbonization was thoroughly analyzed in this paper, referring to that of SD-CNCs in previous study [16].

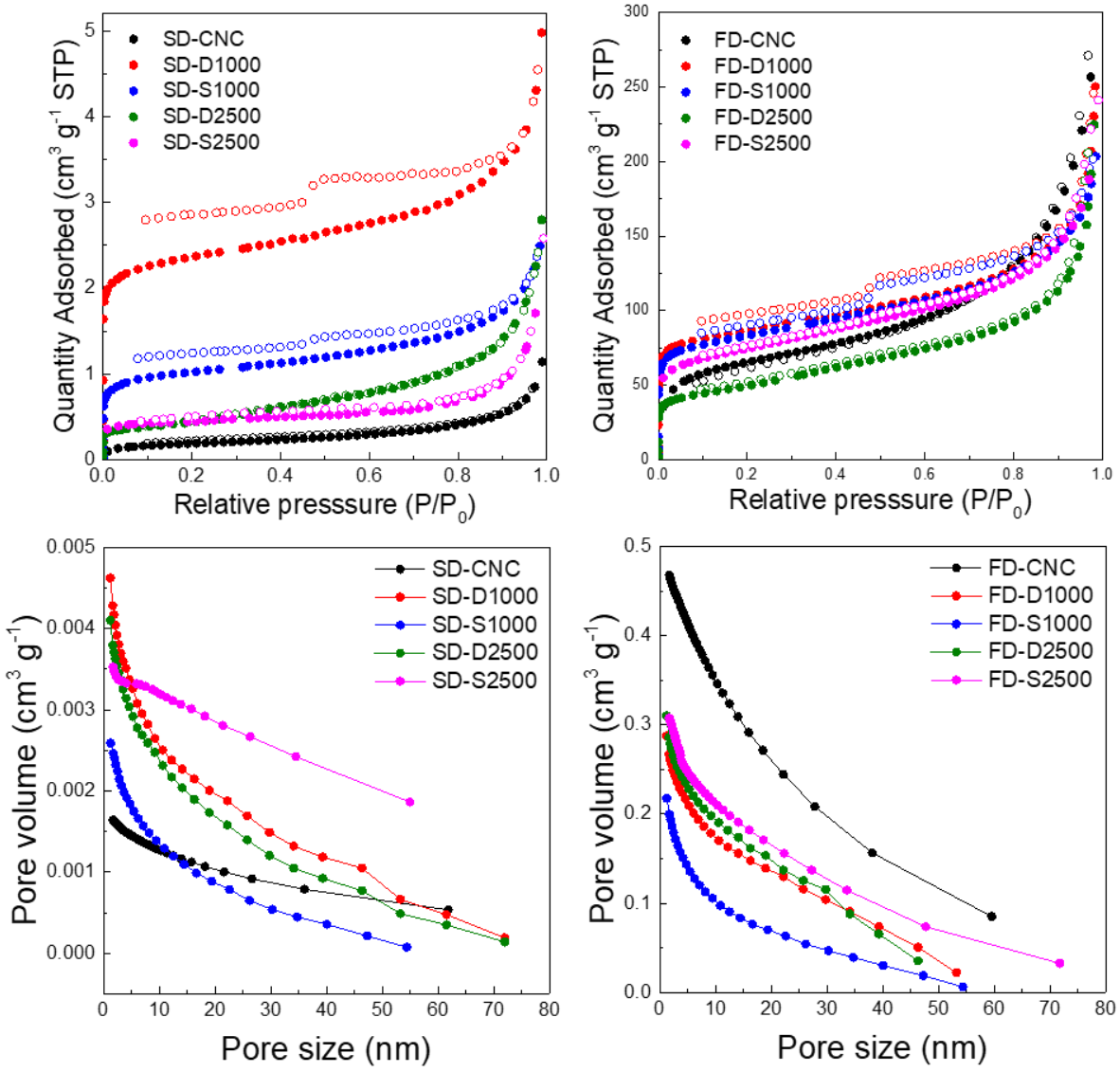


Figure 3.11 $N_2$ adsorption-desorption isothermal curve of SD- and FD-CNC before and after carbonization.

Table 3.3 Surface area, pore volume and pore size of the spray-dried and freeze-dried CNC before/after carbonization measured from BET and BJH results.

| | Spray-dried CNC | | | Freeze-dried CNC | | |
|---|---|---|---|---|---|---|
| | Surface area ($m^2/g$) | Total pore volume ($cm^3/g$) | Mean pore diameter (nm) | Surface area ($m^2/g$) | Total pore volume ($cm^3/g$) | Mean pore diameter (nm) |
| CNC | 0.7 | 0.0018 | 10.4 | 235.5 | 0.4967 | 8.4 |
| D1000 | 9.0 | 0.0078 | 3.4 | 324.6 | 0.3871 | 4.8 |
| S1000 | 3.8 | 0.0039 | 4.0 | 304.9 | 0.3148 | 4.1 |
| D2500 | 1.5 | 0.0043 | 11.5 | 175.6 | 0.3479 | 7.9 |
| S2500 | 1.7 | 0.0040 | 9.6 | 265.2 | 0.3732 | 5.6 |

Figure 3.12 shows the TEM images of pristine, stabilized, and carbonized FD-CNCs. In the pristine FD-CNCs (Figure 3.12a), the highly crystalline parts (red arrow) are observed along with the amorphous parts that have few layer-stacked structures without order (yellow arrow) and have not yet been removed by acid hydrolysis (white arrow), indicating the acid-treatment is not sufficient. Hereafter, we refer to crystalline part (red arrow) and amorphous parts (yellow and white arrows in Figure 3.12a). The structures with high crystallinity inside the CNC retain their order after oxidative stabilization, surrounded by an amorphous structure (Figure 3.12b). After carbonization at 1000 °C, the structures consist of amorphous parts and some graphitic crystals partially aggregated by point and lateral fusion, corresponding to the BJH results in Figure 3.10f (Figure 3.12c and 3.12e). In spite of depolymerization and pyrolysis reactions in the range of 300-800 °C, the observation of highly ordered carbon crystals at low carbonization temperature is a unique feature of CNCs among lots of cellulosic materials based on their high crystallinity and structural density [16-18]. Souza et al. also observed the preservation of ordered structures in stabilized CNCs at 300 °C, and rod-like highly ordered graphite in carbonized CNCs at 1000 °C, while the cellulose produced only amorphous aggregates [18]. In addition, Kim et al. confirmed that the more crystalline structures appeared after carbonization from the pristine cellulose with higher crystallinity [57]. They also asserted that the crystalline portions of the cellulose microfibrils retained their morphology after carbonization. At high carbonization temperature, the larger and thick graphitic crystals were shown as the fusion between adjacent graphite crystals by heat became more active (Figure 3.12d and 3.12f).

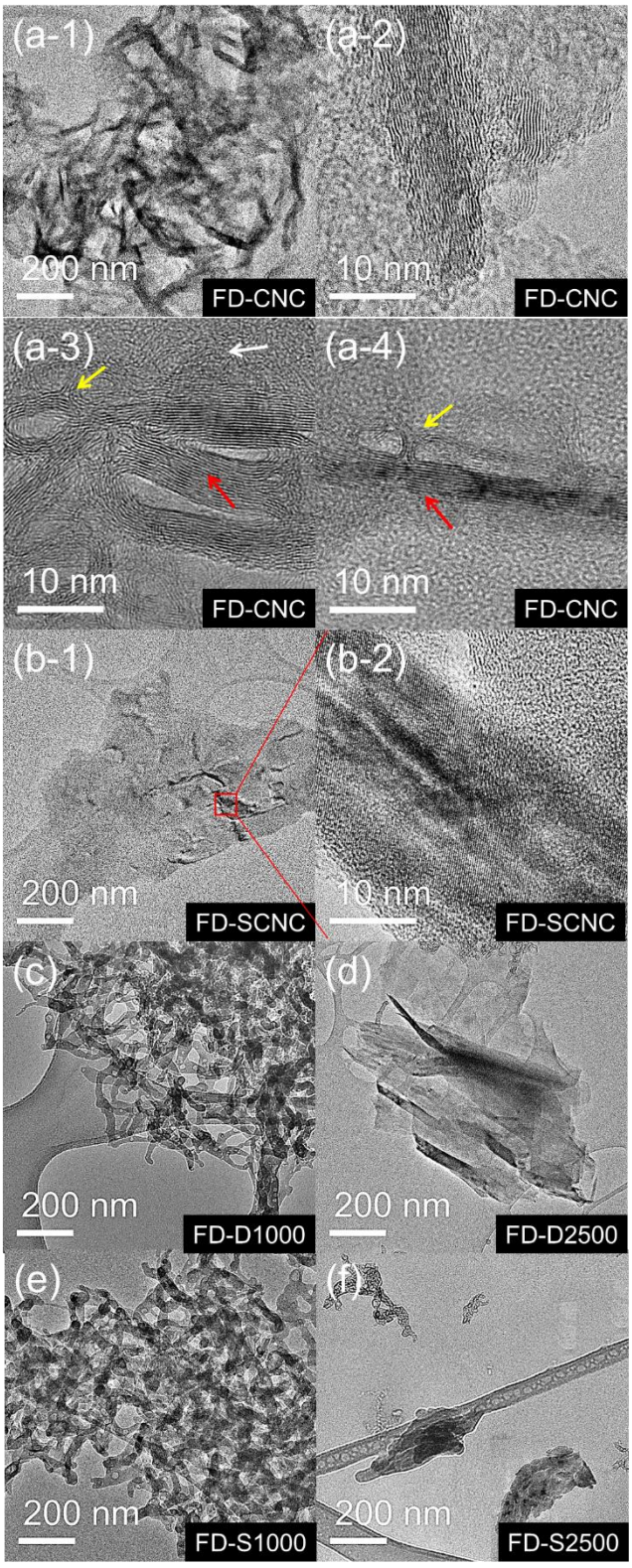


Figure 3.12 TEM images of (a) FD-CNCs, (b) stabilized FD-CNCs, and (c-f) carbonized FD-CNCs at 1000 and 2500 °C with or without stabilization process.

The TEM images with higher magnification of FD-CNCs with respect to the carbonization temperature are represented in figure 3.13 and figure 3.14. The microstructure of carbonized CNCs can be classified into four representative parts based on TEM images as follows: amorphous carbon, amorphous- (A-), turbostratic- (T-), and graphitic- (G-) components. Amorphous carbon is a weak structure without any order and usually envelops the crystal [60, 61]. A-component is a randomly arranged structure with short-range order, which is also called turbostratic nanodomain [27]. T-component is the intermediate structure of A and G-component in the structural development process. It is more ordered and thicker layered structure with smaller d-spacing than A-component, but the boundary between them is ambiguous [40, 60, 61]. Finally, G-component is highly ordered large graphitic crystals with an interlayer distance less than 0.34 nm [40, 60, 61]. Most of the structure of CNCs consists of amorphous carbon after carbonization at 1000 °C (Figure 3.13a and 3.13e), even though the graphitic structure is observed (Figure 3.14a and 3.14e). From 2000 °C, the only a few amounts of amorphous carbon are observed, and the A-component are dominant (Figure 3.13c-d and 3.14g-h). They seem to have burned out or developed into A-components during carbonization. With increasing carbonization temperature, the amounts of T- and G-components increased and coalescence between them occurred, resulting in the growth of graphitic crystals (Figure 3.14). Thus, large graphitic crystals with 0.335 nm of d-spacing, which is similar to the single graphitic structure, could be observed in 2500 °C-carbonized CNCs (Figure 3.14d and 3.14h). Importantly, there is no difference in microstructure of carbonized FD-CNCs regardless of adding stabilization process as observed by TEM images. In comparison, the direct carbonization of SD-CNCs led to an irregular morphology due to the molecular fusion whereas stabilization followed by carbonization process preserved the pristine needle-like structure of SD-CNCs [16]. Unlike SD-CNCs, the slight difference depending on stabilization in FD-CNCs is attributed to the evenly distributed heat based on their well-dispersed pristine morphology and high surface area. Therefore, adding a stabilization process or going through a stabilization temperature range as the temperature rises during carbonization may have felt similar to FD-CNCs.

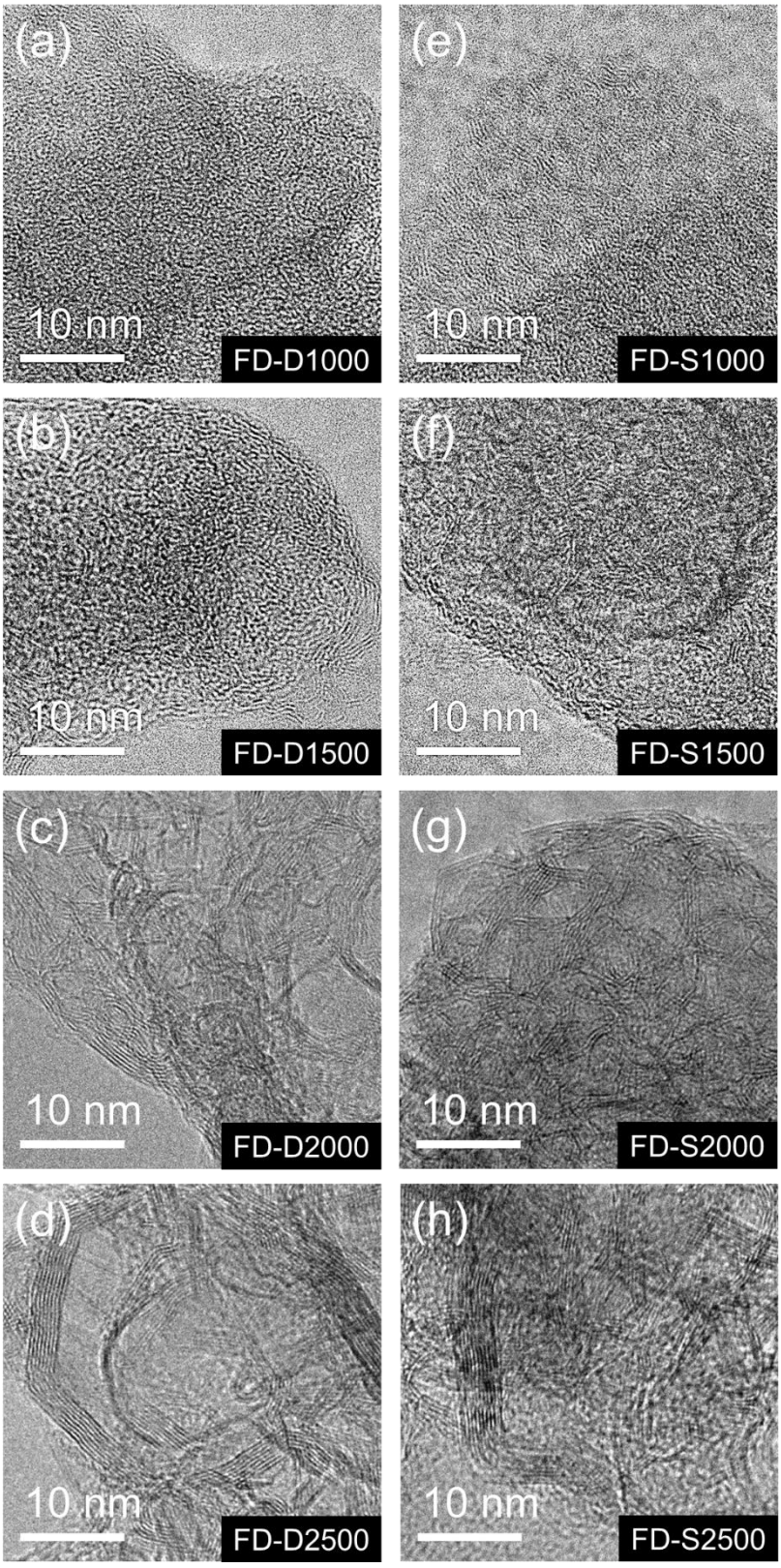


Figure 3.13 TEM images of amorphous carbon and A-component of carbonized FD-CNCs at various temperatures with or without stabilization process.

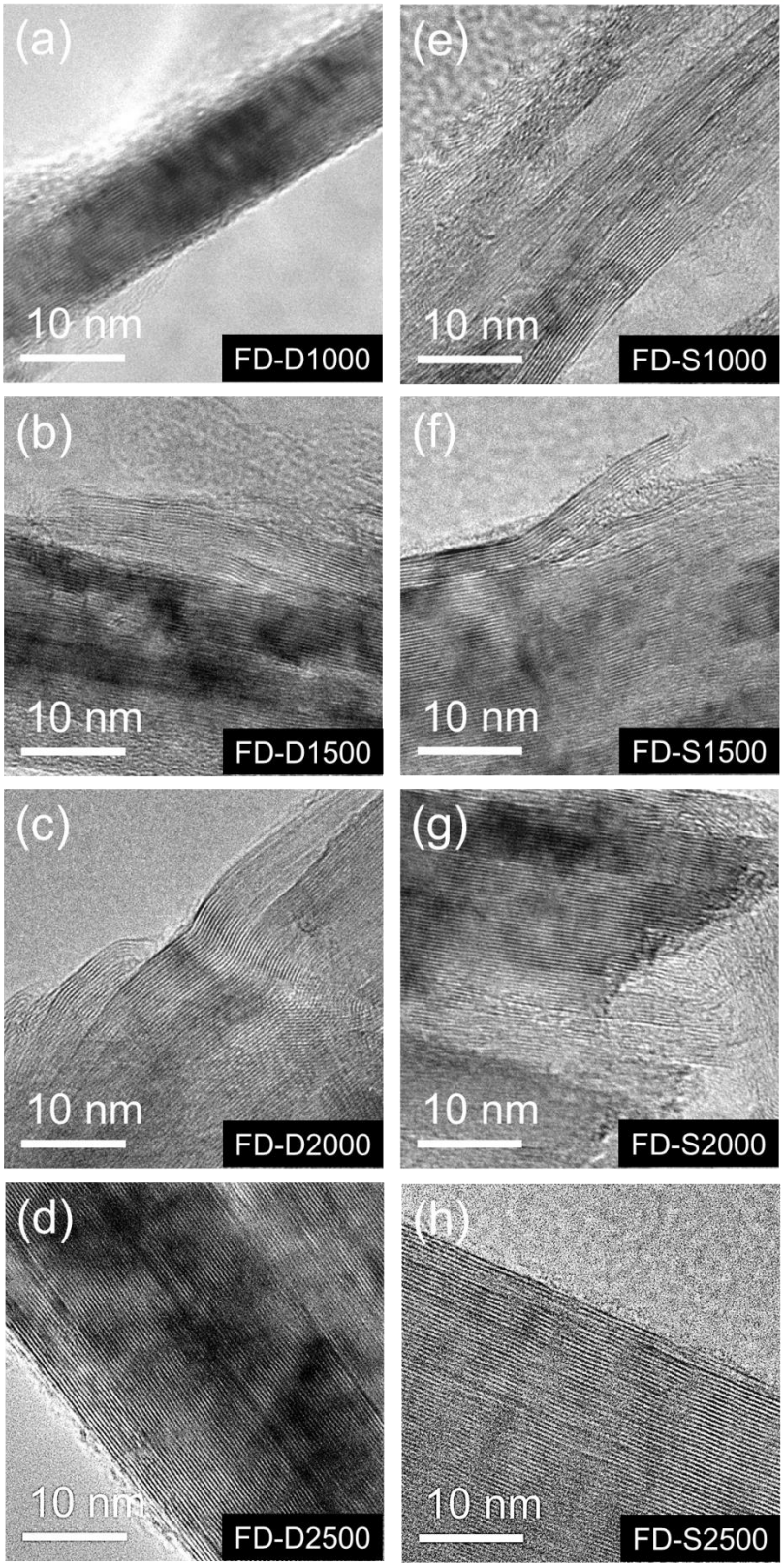


Figure 3.14 TEM images of T- and G-component of carbonized FD-CNCs at various temperatures with or without stabilization process.

The mechanism of structural change of each component during heat-treatment was investigated in detail based on TEM images. Figure 3.15 shows the variation of A-components and its related structural parameters. It is known that the stabilization process followed by pyrolysis causes dehydration and depolymerization to disrupt the structure of cellulosic materials [38, 62, 63]. Hence, A-components in carbonized FD-CNCs seem to be originated from the amorphous structure and short-ranged small crystals in pristine FD-CNCs (Figure 3.15a). Since they are weaker and have lower thermal stability than crystal parts in pristine CNCs, they become easily relaxed and turn into an amorphous carbon structure by the stabilization process or going through the stabilization temperature region, as represented by red circles in Figure 3.15b [62]. Then, they begin to develop again with carbonization from amorphous carbon without any order into randomly distributed and short-ranged disordered carbon, which is A-component (Figure 3.15c). With increasing carbonization temperature, the number of stacked layers, domain length, and order of A-component carbonic structure increases (Figure 3.15d and 3.15f). The schematics of structural evolution mechanisms of A-components in FD-CNCs are exhibited in Figure 3.14e. This is the process that becoming of A-component to T-component at high temperature and shows that highly developed A-component can also be T-component. The d-spacing of A-components of both FD-D2500 and FD-S2500 were ~0.34 nm, which is similar to that of T-components (Figure 3.15f).

The T- or G-components evolution mechanism based on TEM images and variation of structural parameters are shown in Figure 3.16. They are already existed from the low carbonization temperature before formation by the development of A-components at high temperatures. These T- or G-components are attributed to the highly crystallized structures of pristine FD-CNCs with high thermal stability, which have less relaxation by heat and can quickly be converted to carbon even if they occur [62]. Thus, the crystalline part was observed after the oxidative stabilization (Figure 3.16b), and the graphitic structure was observed after pyrolysis (Figure 3.16c). During dehydration and depolymerization in the range of 300-800 °C, the crystal size was reduced compared to that of pristine CNCs due to the shrinkage and the relaxation of the weak structures mainly on the surface or edge of the crystals [17]. However, the graphitic crystal size was actively increased above 2000 °C as the coalescence and lateral fusion between crystals occur, and the d-spacing was stea.dily decreased at the same time (Figure 3.16f). Finally, both crystals in FD-D2500 and FD-S2500 have about 50 nm of crystal thickness and about 0.335 nm of d-spacing, which is same as the interlayer distance of theoretical graphite [64, 65].

To summarize the carbonization mechanism of FD-CNCs, the structural change of each component according to the heat-treatment is illustrated in Figure 3.17. The weak and amorphous structure from the pristine state develops into amorphous carbon or A-component after carbonization,

and it becomes a large and highly ordered structure similarly to T-component when graphitization occurs at high temperature. Further, the intrinsically highly crystallized parts from the pristine state maintain its crystallinity during stabilization and pyrolysis or only are partially relaxed, so it is easy to observe the T- or G-components from low carbonization temperature, and their d-spacing decreases and graphitic crystal size increases with temperature. The structural evolution mechanism is same in FD-CNC regardless of adding stabilization process due to the individually separated morphology based on its high surface area and rapid heat diffusion to the inside of the CNC, unlike SD-CNC which confirmed in our previous study [16].

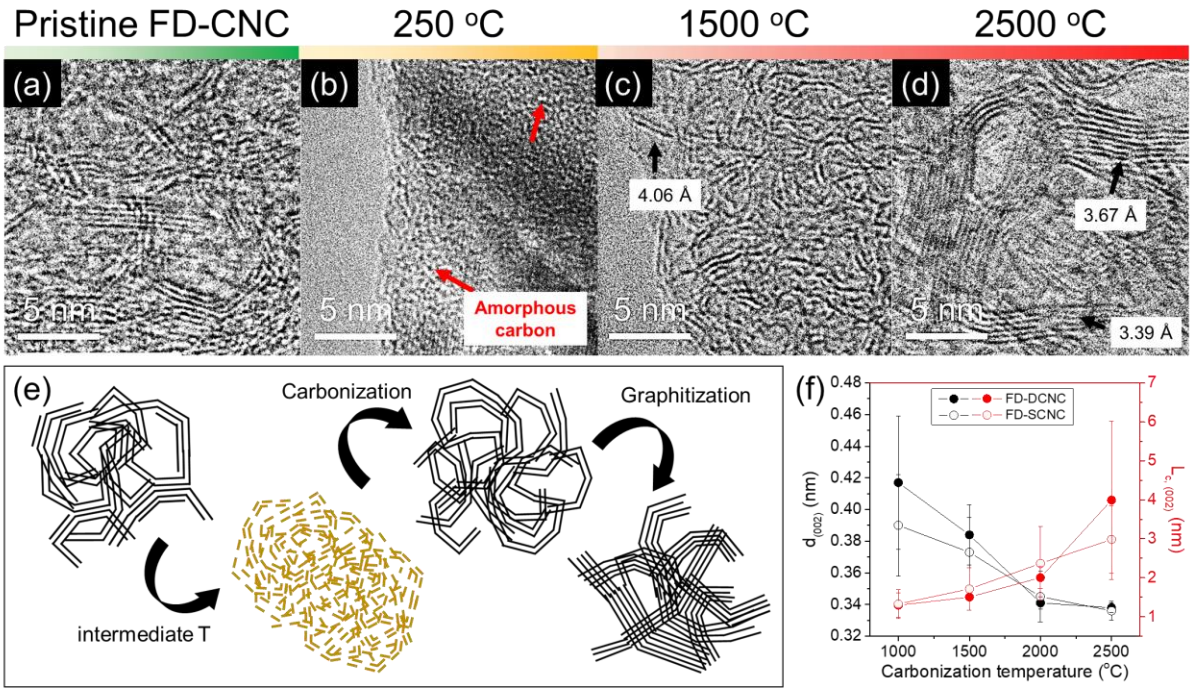


Figure 3.15 Structural evolution mechanisms of A-components in FD-CNCs during heat-treatment process. TEM images including A-components of (a) FD-CNCs, (b) stabilized FD-CNCs, and (c-d) carbonized FD-SCNCs, respectively. (e) Schematics of mechanisms of A-components based on TEM images. (f) The variation of d-spacing and crystal thickness of A-components in FD-CNCs during carbonization.

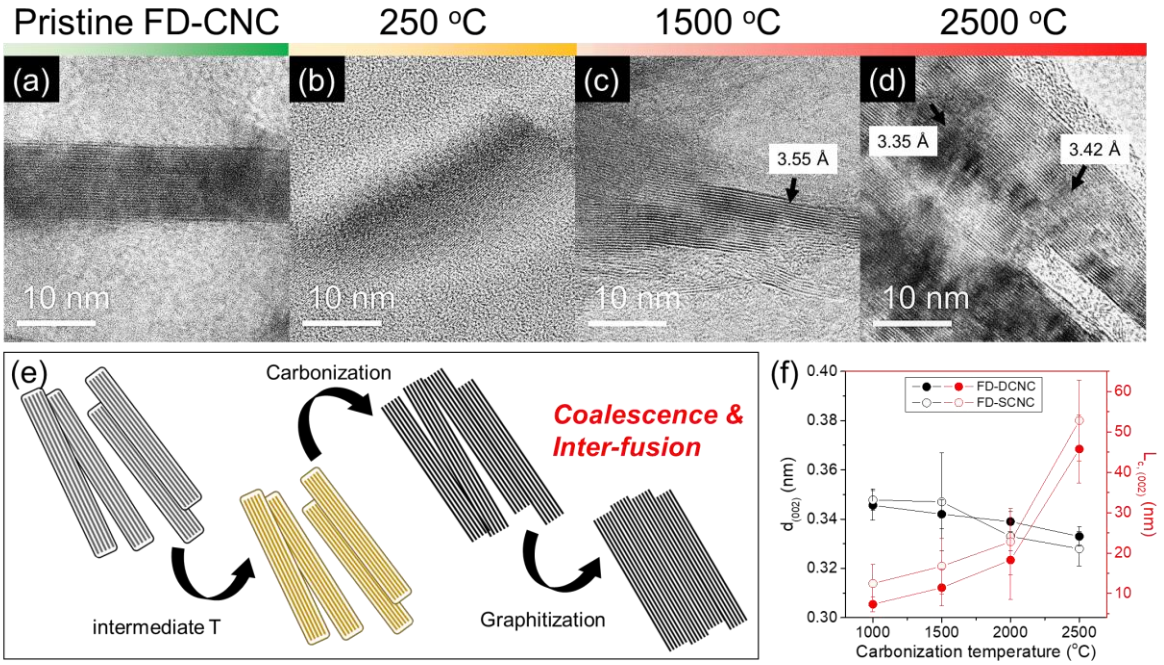


Figure 3.16 Structural evolution mechanisms of T- or G-components in FD-CNCs during heat-treatment process. TEM images including T- or G-components of (a) FD-CNCs, (b) stabilized FD-CNCs, and (c-d) carbonized FD-SCNCs, respectively. (e) Schematics of mechanisms of T- or G-components based on TEM images. (f) The variation of d-spacing and crystal thickness of T- or G-components in FD-CNCs during carbonization.

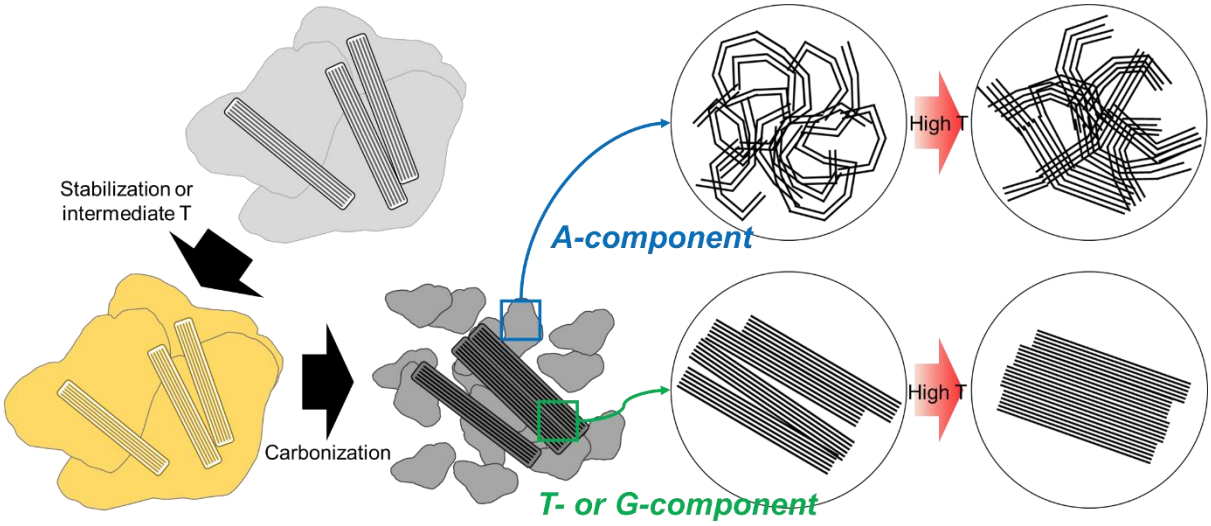


Figure 3.17 Structural evolution mechanisms of various components in FD-CNCs during heat-treatment process.

Figure 3.18 show the WAXD spectra of carbonized FD-CNCs with respect to the carbonization temperature. The intensity of two carbon peaks, (002) about 26° and (10) about 41°, was very small up to 2000 °C. However, at 2500 °C, the two sharp peaks indicating T- (26°) and G-component (26.5°) which typically appear on hard carbon become prominently observed as the intensity increase and separation of (002) carbon peak occurs [16, 42]. This is because of the dramatic developments of graphitic structure and their thickness by coalescence and inter-fusion above 2000 °C, which corresponds to the TEM images (Figure 3.16). Based on the TEM images, the peak deconvolution was performed to investigate the interlayer distance of (002) and crystal size (Lc, nm), which is represented in figure 3.18 and figure 3.19. Up to 1500 °C, amorphous carbon and A-component exist together due to the low degree of the structural development. Interestingly, small sharp peak around 26.5° is observed at 2000 °C. Also, the WAXD spectra of carbonized FD-CNC above 2000 °C with clearly distinguished (002) peaks were deconvoluted with A-, T-, and G-components. The crystal size (Lc) was calculated based on the deconvoluted spectra (Figure 3.20). For A-components, crystal size is further developed with carbonization temperature, but the growth of A-components is limited by 5 nm. However, the crystal size for T-component grows explosive from about 5 nm of 2000 °C to about 60 nm of 2500 °C. It is attributed to the A-component is further developed, followed by the fusion with T-component. For G-component, the crystal size of about 40 nm has been already formed even at 2000 °C and slightly developed with carbonization temperature. Crystal size Both FD-D2500 and FD-S2500 showed little structural difference, and the d-spacing and crystal thickness values from deconvolution also showed consistency with those obtained from the TEM images (Figure 3.14d and Figure 3.14h). Interestingly, the WAXD spectra of SD-D2500 and SD-S2500 were deconvoluted with four peaks with amorphous carbon compared to the three peaks of FD-D/S2500 (Figure 3.21). It is attributed to the irregular development of graphitic structure due to the compact morphology of SD-CNCs. The inner structure of SD-CNC undergoes the low degree of structural development compared to the outer surface of SD-CNC. However, the crystal sizes of three components for SD-D/S2500 are larger than carbonized FD-CNCs (Figure 3.20 and Figure 3.22). The crystal size of A-component for SD-D/S2500 is around 6 nm, which is twice compared to those of FD-D/S2500. Also, the crystal size of G-components for SD-D/S2500 is around 120 nm and it means that the SD-CNCs further have the change for fusion. Because the CNC particles have attached each other, the graphitic crystal can be fused with neighboring CNC particles and grow. It is also proved by the area fraction of WAXD (Figure 2.23). It suggests that the development of microstructure of carbonized CNC depends on the morphology of CNCs.

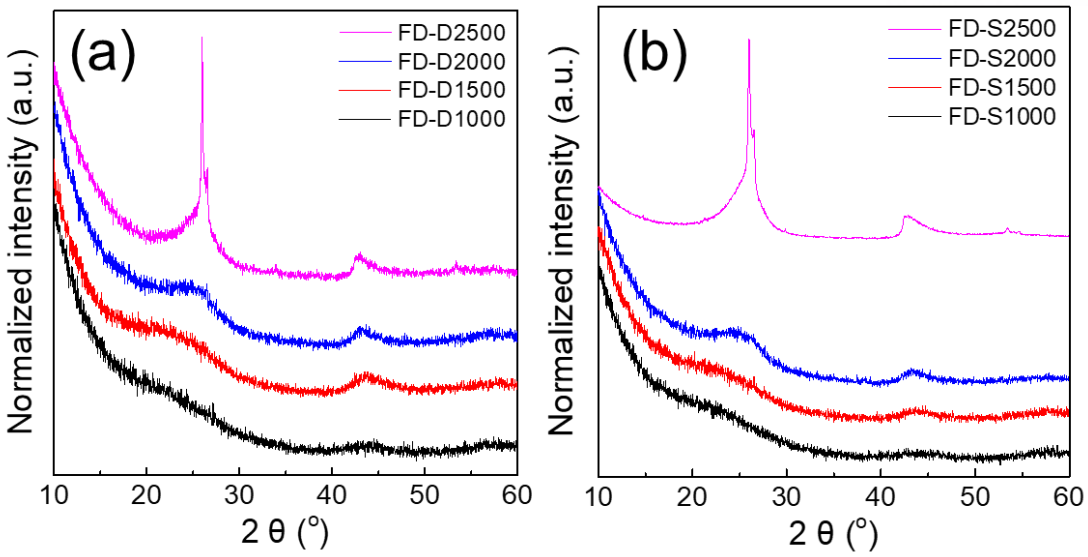


Figure 3.18 WAXD spectra of (a) FD-DCNCs and (b) FD-SCNCs carbonized at various temperatures.

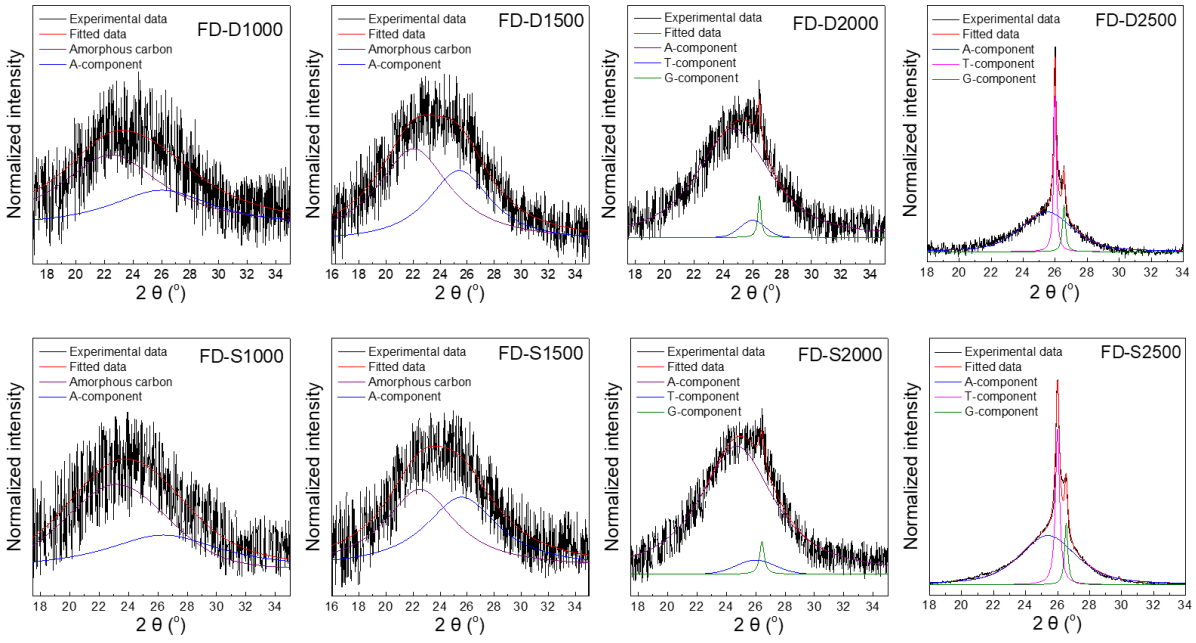


Figure 3.19 Peak deconvolution of WAXD spectra of carbonized FD-CNCs. Four peaks (amorphous carbon, A-, T-, and G-components) were used for deconvolution based on TEM images.

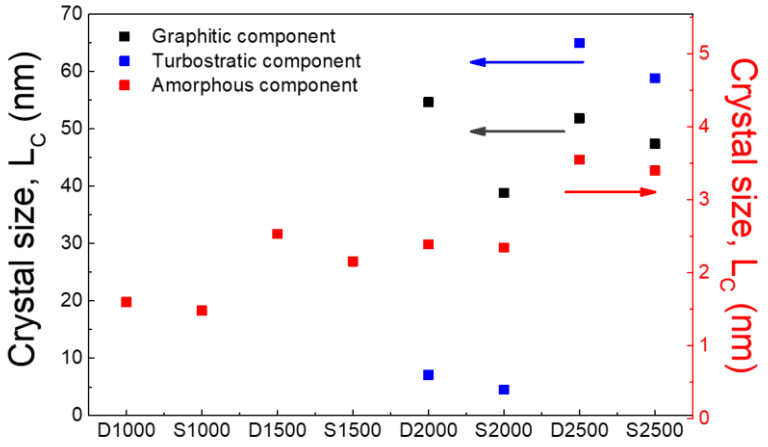


Figure 3.20 The crystal thickness of A-, T-, and G-components in carbonized FD-CNCs.

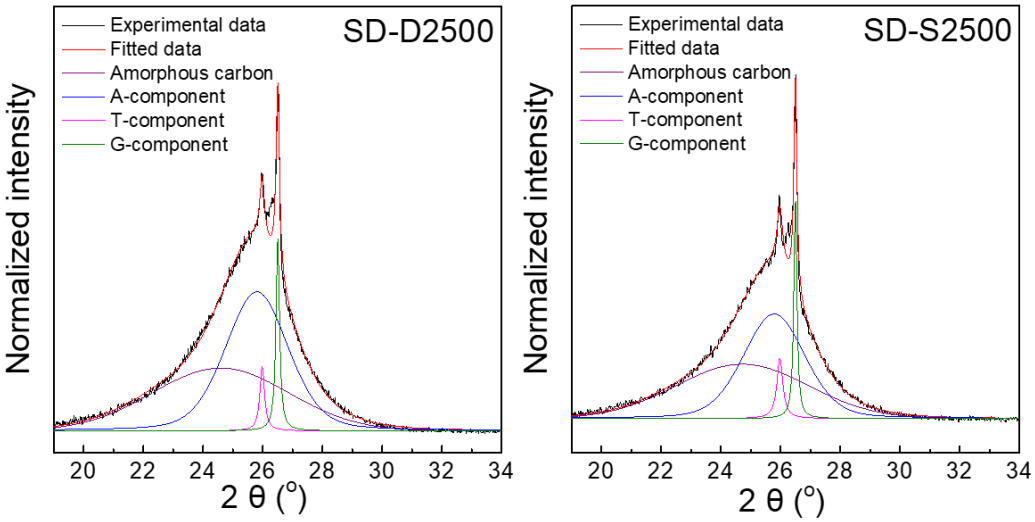


Figure 3.21 Peak deconvolution of WAXD spectra of carbonized SD-D2500 and SD-S2500. Four peaks (amorphous carbon, A-, T-, and G-components) were used for deconvolution based on TEM images.

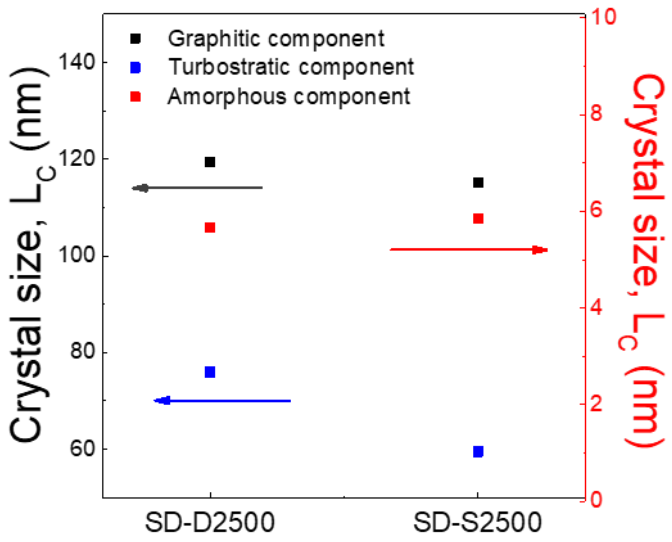


Figure 3.22 The crystal thickness of A-, T-, and G-components in carbonized SD-CNCs.

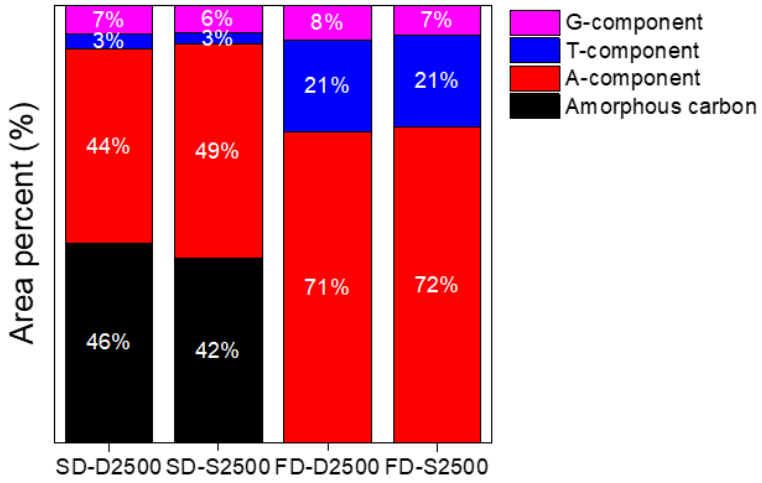


Figure 3.23 Area percent of fitted spectra of carbonized at 2500 °C.

Raman spectra of FD-DCNC and FD-SCNC were also measured in order to further analyze the microstructure on a smaller scale than the crystal (Figure 3.24a and 3.24b). Also, the 2D correlation and gradient mapping were applied to trace the microstructural change with the carbonization temperature, which can provide insight into the transition mechanism (Figure 3.24c and 3.24d). The 2D gradient maps of d($I$)/d($T$) plot the values of the 1$^{st}$ derivatives of the Raman intensity ($I$) as a function of the temperature ($T$) over the space of temperature vs. Raman shift ($cm^{-1}$), based on the area-normalized Raman spectra. The red contour lines represent positive values of d($I$)/d($T$), that is, increasing trend of the Raman intensity with temperature, and vice versa for the blue contour lines. It is important to note that the FD-DCNC and FD-SCNC didn't show an obvious difference in Raman spectra and a 2D gradient map. For both carbonized CNCs, not only D- and G-bands at around 1350 and 1580 $cm^{-1}$, respectively, noticeable changes are also observed in the vicinity of 1200 $cm^{-1}$ from TPA-band and 1500 $cm^{-1}$ from A-band during carbonization [16, 41, 45, 46]. Depending on the transition temperatures in which the changes of these bands are apparent as indicated by dashed lines in Figure 3.24c and 3.24d, the structural evolution mechanism of FD-CNC is divided into four distinct stages as follows: stage 1 (1000-1400 °C), stage 2 (1400-1800 °C), stage 3 (1800-2200 °C), and stage 4 (2200-2500 °C). In stage 1, the D- and G-bands slightly increased with little variation of TPA- and A-bands, indicating the formation of turbostratic carbon structure [16, 41, 45, 46]. However, it is interesting to note that the TPA- and A-bands decreased whereas the D- and G-bands rapidly increased in stage 2, which shows the simultaneous structural changes in graphitic and non-graphitic structures. In this stage, it is suggested that amorphous carbon is removed by heat or sacrificed as a feedstock carbon to produce polycrystalline graphitic structure by engaging in crystal growth [16, 66]. Further, the stronger intensity and higher contour in D-band than G-band is attributed to the increment of imperfect structure with lots of disorders and defects, and many edge regions based on the small size of graphitic crystals. In stage 3, D- and G-bands continuously increased whereas TPA- and A-bands became unchanged. Compared with previous stage 2, the increase of G-band is more pronounced than the D-band, which means the growth of crystallites and the development of disordered graphitic structure at an early stage of graphitization. In stage 4, the D-band decreased while G-band sharply increased due to the coalescence and the lateral inter-fusion between graphitic crystals resulted in large crystal size. These behaviors are also associated with the structural healing of defective graphitic structure and getting perfect microstructure at the later stage of graphitization.

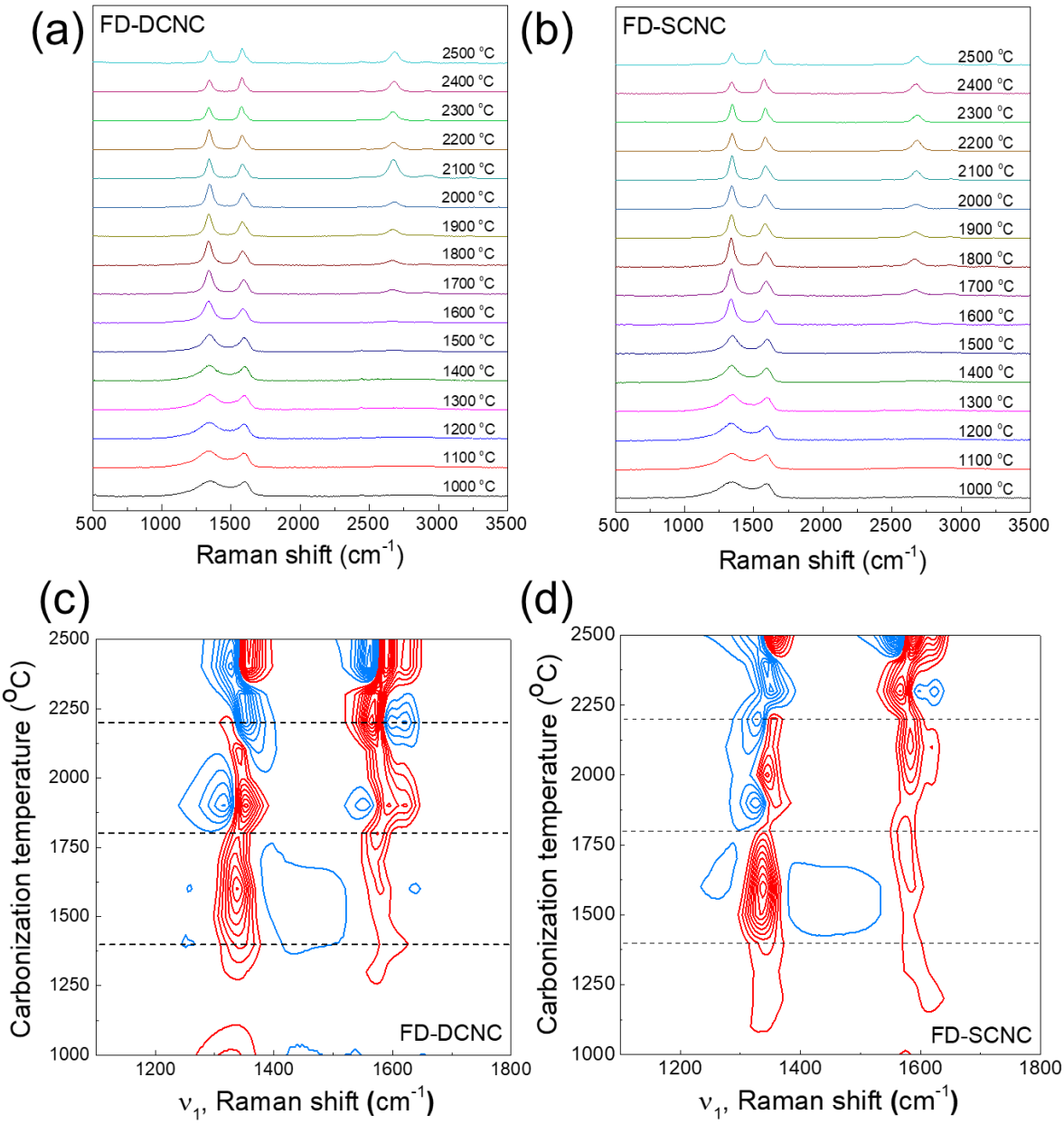


Figure 3.24 (a, b) Variation of Raman spectra and (c, d) 2D gradient maps of *d(I)/d(T)* that plots the value of the 1st derivatives of Raman intensity (*I*) with respect to carbonization temperature (*T*) for FD-DCNCs and FD-SCNCs during carbonization. The red and blue color indicate the positive and negative values of *d(I)/d(T)*, respectively. Dashed lines in 2D gradient maps indicate the transition temperatures at which noticeable change in contour map takes place.

For a detailed study of the respective carbonization stages, all the Raman spectra were deconvoluted by five bands using the aforementioned bands together with the D'-band at 1620 cm-1 (Figure 3.25). Then, the changes in various structural parameters with temperature analyzed by peak deconvolution were plotted in Figure 3.26a-d with the dashed lines representing the critical temperatures at which each structural parameter exhibits dramatic change. As above, differences between FD-DCNC and FD-SCNC were not observed in the change of these parameters. Figure 3.26a exhibits the comparison of experimental and fitted values of $I_G/I_D$ ratio with respect to the carbonization temperature. Both experimental and fitted $I_G/I_D$ ratio showed different trends for each stage as represented in the 2D gradient map (Figure 3.24). The $I_G/I_D$ values exhibited little variation in stage 1, however, they suddenly decreased due to the stronger increase of D-band than the G-band as polycrystalline disordered graphitic structure was formed in stage 2. Conversely, in stage 3 and stage 4 where the increase rate of G-band is higher than that of D-band because of graphitization, $I_G/I_D$ ratio increased. It is noteworthy that there was a deviation between the experimental and fitted $I_G/I_D$ values until stage 2, but they showed consistency from stage 3. This is because of the large influence of defect-related TPA- and A-bands overlapped with D- and G-bands, resulting in the broad Raman spectra (Figure 3.25). The deviation of both $I_G/I_D$ decreased gradually in stage 2 as the defects and amorphous structures were removed or sacrificed to make graphitic crystals, and they converged to almost the same value in stage 3, suggesting the dominant presence of graphitic structure over the non-graphitic structure.

The variations of the amorphous fraction ($A_{(A+TPA)}$) which the fraction of combined area of TPA- and A-band in the Raman spectrum and $A_G/A_D$ with temperature are represented in Figure 3.26b. The amorphous fraction was more than 40% after carbonization at 1000 °C, but it reduced until stage 2 and then maintained plateau with a low fraction of about 10%. The 10% remaining even at high temperatures of 2500 °C seems to be due to the edges of graphitic crystals or the short-ranged disordered A-components. Meanwhile, the $A_G/A_D$ ratio continues to increase with temperature, which is opposite behavior to the $I_G/I_D$ ratio in stage 2. This means that the contribution of the area is greater than the intensity of G-band, while the D band is more affected by the intensity because both bands have grown in stage 2, as identified by the red contour line in the 2D gradient map (Figure 3.24c and 3.24d). Depending on the broadness and area of the bands, the area ratio may tend to be different from the intensity ratio of G- and D-band. The reason that the influence of the area or intensity is different is attributed to the variance of structures that contribute to each band, that is, homogeneity of structures [46]. In stage 2, the graphitic structures represented by G-band is still underdeveloped resulting in many inhomogeneous small crystallites, whereas high edge density among the disordered structures represented by D-band. This is consistent with the above-mentioned interpretation that the growth of small polycrystalline graphite with the disappearance of amorphous carbon occurs in stage 2 (Figure 3.24c and 3.24d). From stage 3, both $I_G/I_D$ and $A_G/A_D$ show an increasing behavior, which is the result

of the sharper G-band with higher intensity influence because the structure becomes homogeneous as the graphitic crystal grows. Figure 3.26c exhibits the change in intensity ratio between TPA- or A-band and G-band according to the carbonization temperature. As with the trend of amorphous fraction shown in Figure 3.26b, they decreased to 1800 °C and then showed little variation with both $I_{TPA}/I_G$ and $I_A/I_G$ values below 0.15.

Figure 3.26d shows the variation of position and FWHM of G-band with temperature. Even with the same graphitic structure, position and FWHM have a different perspective on the structure. The position of G-band is related to the fraction of graphitic structure and the number of stacking layers in crystals [67]. However, the FWHM of G-band is governed by the homogeneity of graphitic structure which is influenced by various defects and crystal sizes [46, 67, 68]. As a rule, as the graphitic structure develops during carbonization, both position and FWHM of G-band decrease to 1580 $cm^{-1}$ and 13.5 $cm^{-1}$, respectively, which are reported values of theoretical graphite [46]. They exhibited a slight change in stage 1 but decreased above 1400 °C as the turbostratic-graphitic structure starts to grow. In addition, the position is almost saturated about 1580 $cm^{-1}$ and FWHM about 38 $cm^{-1}$ at temperatures above 2200 °C, which the difference from the theoretical value seems to be largely affected by the A-components as observed in TEM and XRD results (Figure 3.15 and Figure 3.19).

The presence of the stabilization process was insignificant in the difference in morphology and structural conversion of FD-CNC, which both FD-DCNC and FD-SCNC showed the same behavior depending on the carbonization temperature. Meanwhile, regarding SD-CNC, molecular fusion occurred by direct carbonization, whereas the pristine needle-like structure was preserved stabilization and subsequent carbonization. However, despite the maintenance of pristine morphology in SD-SCNC, its macroscopically highly aggregated pristine state with low surface area as compared to the FD-CNC may affect to the sensitivity to stabilization process and the less developed carbonized structure via slow heat diffusion. The fitted $I_G/I_D$ ratio of SD-S2500 and FD-S2500 were 1.0 and 1.2, and $A_G/A_D$ were 0.9 and 1.0, respectively. Further, the graphitic crystal thickness was about 10 nm in SD-S2500, while about 55 nm in FD-S2500.

Not only the internal structure of the graphitic crystals but also the edge regions were observed by TEM images as a function of carbonization temperature (Figure 3.27). At low-temperature carbonization (Figure 3.27b), the structure is more ordered than the pristine state, but edge of crystals was exposed. As temperature increased, a curvature occurs at the end of the crystal and it becomes closely folded (Figure 3.27c) and finally graphene nanoribbon shapes are formed at 2500 °C (Figure 3.27e). Harries et al. noticed that these tightly folded graphene edges are quite frequently seen in carbons, and this phenomenon occurs to reduce the surface energy of crystals [69]. This behavior has also been observed in carbonized SD-CNCs, possibly due to the high-temperature carbonization above 2000 °C (Figure 3.28).

Figure 3.29 shows the dispersibility of carbonized SD-CNC and FD-CNC for the application as a carbon nanofillers of polymer nanocomposites. The dispersion of carbonized CNC with 0.1 wt.% concentration in DMF was sonicated in bath-type sonication from 0.5 h to 3 h. With naked eyes, the color of the dispersion for SD-D2500 is lighter than the one of FD-D2500 (Figure 3.29). It leads to the high transmittance of SD-D2500 above 70% even with the sonication time of 3 hours. However, the FD-D2500 shows the very low transmittance below 5% with the only 1 hour. It is attributed that carbon particles with small size is easily dispersed in solvent due to the high surface area. Also, for carbonized SD-CNC, the particles with compact morphology can't be broken because the fusion in the compact granules during carbonization. It suggests that the carbonized FD-CNC will shows the better dispersion in polymer matrix even with the short dispersion time.

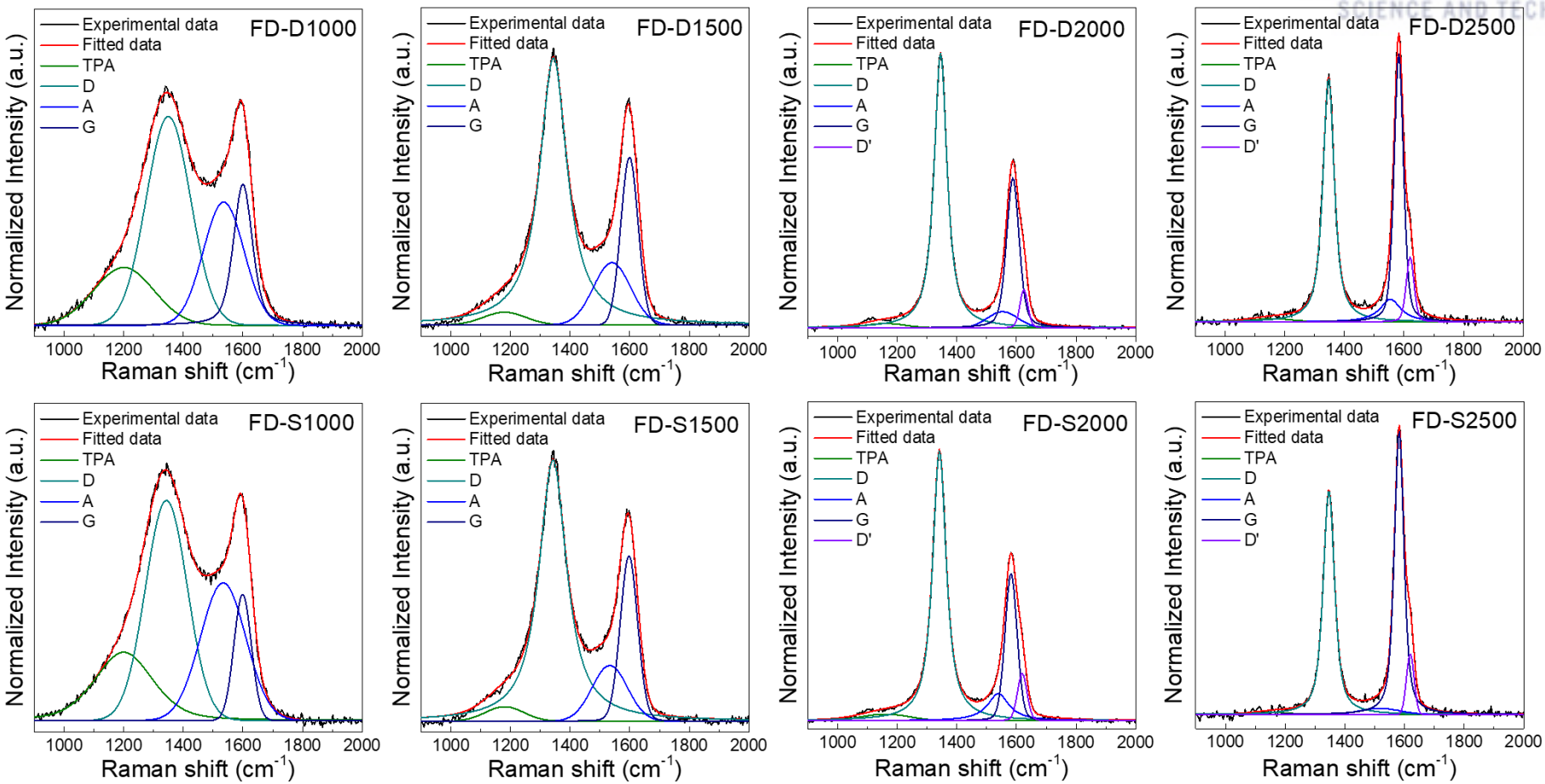


Figure 3.25 Peak deconvolution of Raman spectra based on five TPA, A, D, G, and D' bands.

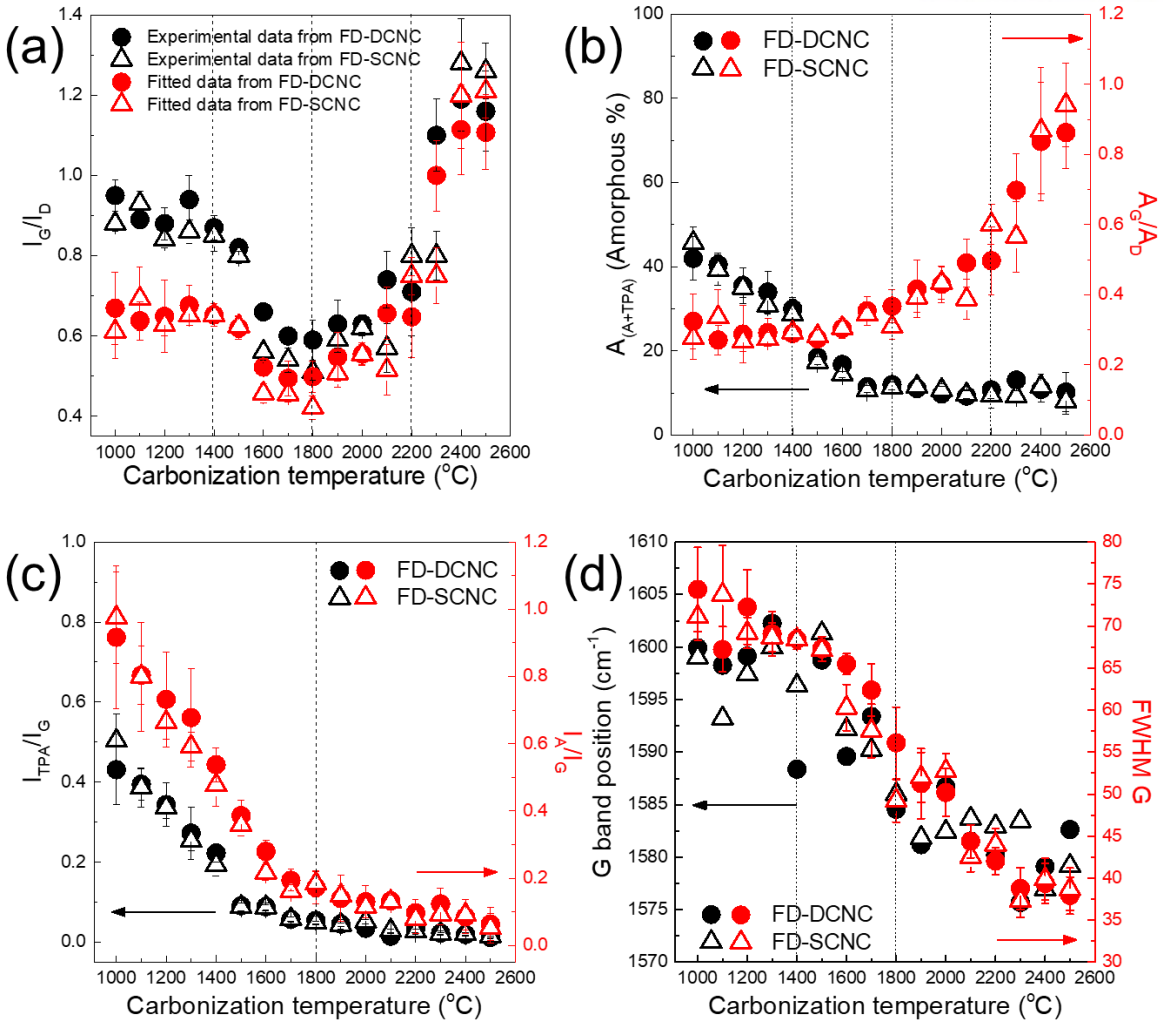


Figure 3.26 The change of structural parameters with carbonization temperature according to the deconvolution of Raman spectra: (a) $I_G/I_D$ ratios based on experimental and fitted Raman spectra, (b) $A_{(A+TPA)}$ (amorphous fraction, %) and $A_G/A_D$ ratio, (c) $I_{TPA}/I_G$ and $I_A/I_G$, and (d) position and FWHM of G band. Dashed lines in e-h indicate the critical temperatures at which each structural parameter exhibits dramatic change.

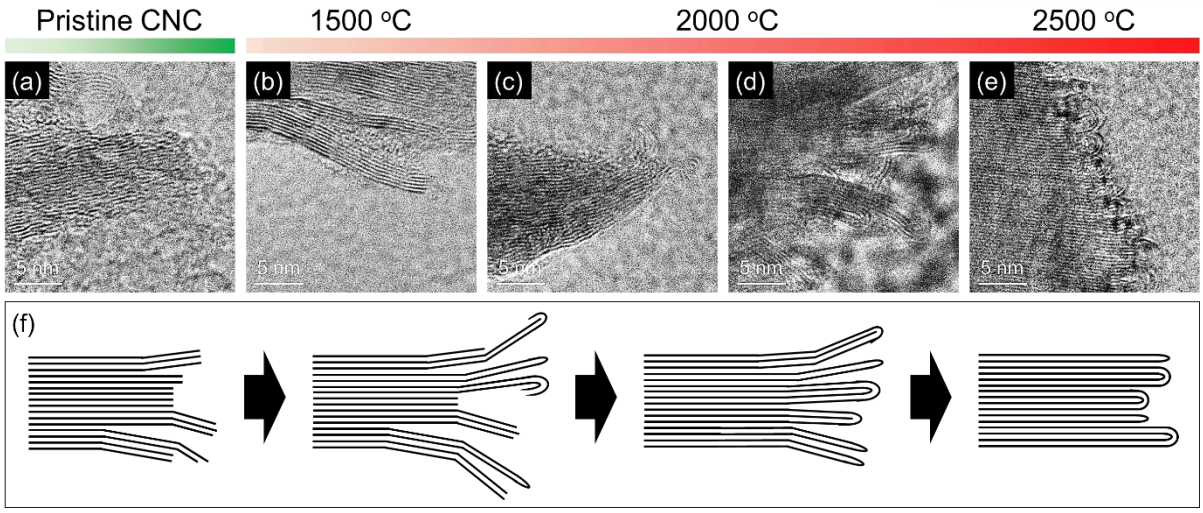


Figure 3.27 TEM images of (a) FD-CNCs and carbonized FD-CNCs at (b) 1500 °C, (c, d) 2000 °C, and (e) 2500 °C and, which are focused on the edge of graphitic crystals. (f) Structural evolution mechanism of edge regions of graphitic crystals.

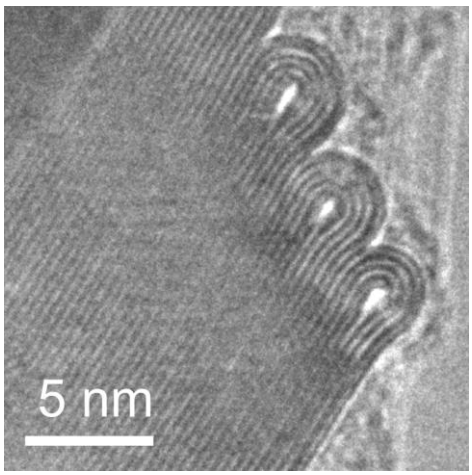


Figure 3.28 TEM image of SD-D2500, which shows the curved edge of crystals.

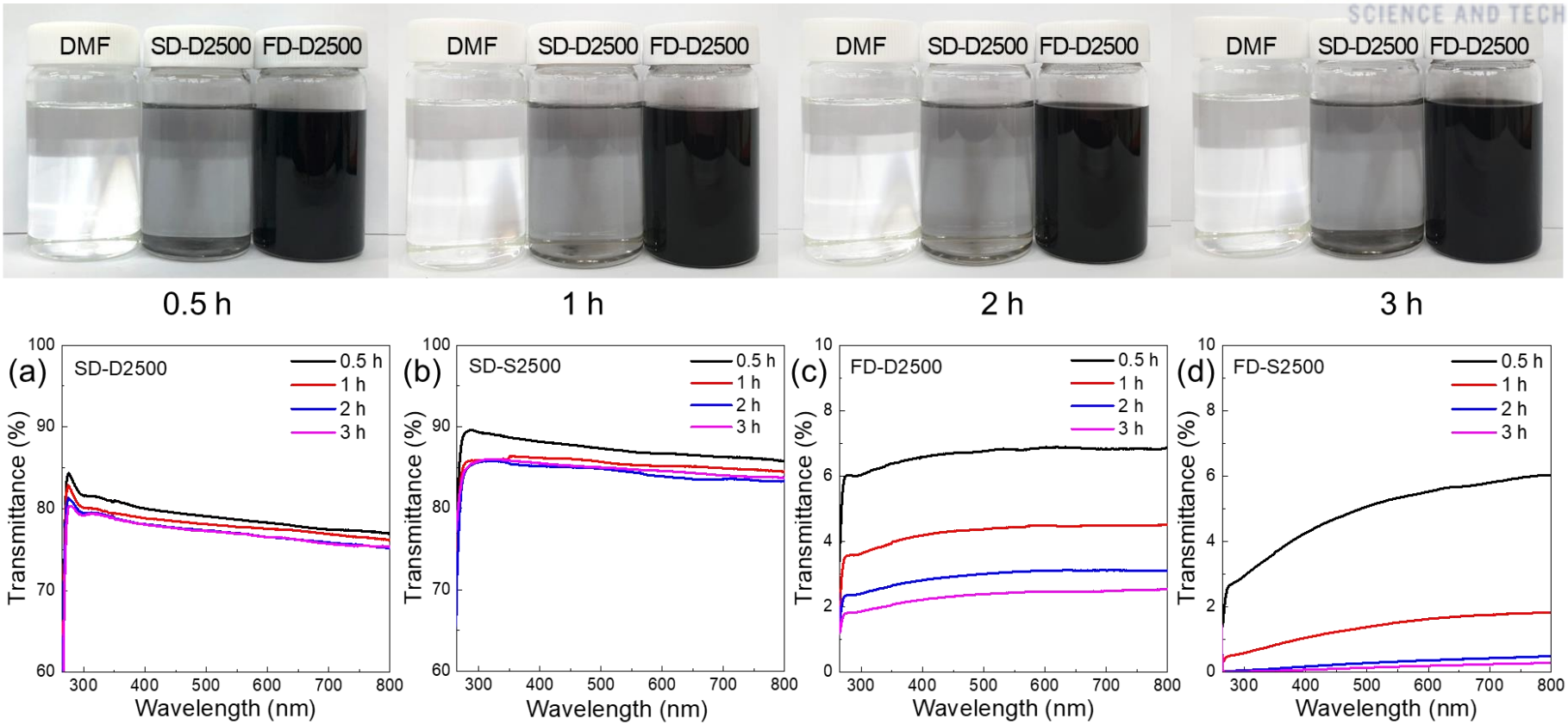


Figure 3.29 (a)-(c) The photographic images of dispersed carbonized CNCs with the sonication time and (d)-(e) The UV-vis spectra of SD-D2500 and FD0D2500.

### 3.4. Conclusion

Pristine CNC has different macroscopic morphologies depending on the drying method: SD-CNC is aggregated but FD-CNC is separated and branched with a high surface area. Their morphology affects not only that of carbonized CNCs in micro- and macro-scale but also structural development. In this study, FD-CNCs were carbonized from 1000 to 2500 °C and the behavior of A-, T-, and G-components were thoroughly analyzed, respectively, using various characterizations. Further, the structures and morphologies of carbonized FD-CNCs were compared with those of carbonized SD-CNCs, which are represented in our previous paper. During the carbonization of FD-CNCs, the weak and amorphous structure from the pristine state develops into amorphous carbon or A-component while the intrinsically highly crystallized parts become T- or G-components from the low carbonization temperature. Commonly, the $d_{002}$ of all the components decreased with the increase in crystal size with respect to the temperature. The structural evolution mechanism of FD-CNCs can be divided into four stages. In stage 1 (1000-1400 °C), the turbostratic carbon is formed that may act as nucleation points of crystals. In stage 2 (1400-1800 °C), amorphous carbon is removed by heat or sacrificed to produce small-sized carbon crystals with lots of disorders and defects, which is confirmed by a decrease in intensity of TPA- and A-bands whereas opposite trend of D- and G-bands of Raman spectrum. In stage 3 (1800-2200 °C), the increase of G-band becomes higher than that of D-band due to the growth of graphitic crystals. Finally, in stage 4 (2200-2500 °C), the microstructure is highly developed, and the graphitic crystal size dramatically increases via coalescence and lateral inter-fusion between crystals. Unlike SD-CNC, the FD-CNC showed very slight effects of oxidative stabilization on its microstructure and morphology, which may be due to the rapid heat diffusion and uniform structural change in the inner and outer parts of the CNC based on its high surface area. The current study provides an understanding of the carbonization mechanism of FD-CNCs and can be used to various application fields with tailoring the microstructure and properties.

# Chapter 4. High-performance Amorphous Polyetherimide (PEI) fiber and the effect of CNC as a nanofiller

## 4.1. Introduction

### *4.1.1 Polyetherimide (PEI)*

Polyetherimide (PEI) is a super engineering thermoplastic belonging to the polyimide (PI) family [70]. PEI, which is known by the commercial name of Ultem1000. PEI is synthesized from 4,4'-(4,4'-Isopropylidenediphenoxy) bis(phthalic anhydride) (BPADA) and 1,3-Phenylenediamine (m-PDA) by polycondensation, followed by imidization. It has the structural unit (MW: 592.61 g/mol, density: 1.27 g/cm$^3$):

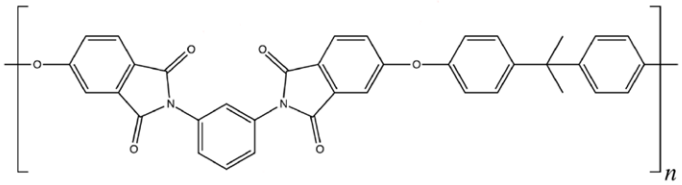

Figure 4.1 The structural unit of polyetherimide (PEI)

PEI exhibits various superior properties as high mechanical properties, dimensional stability, and thermal stability, chemical resistance, and thermos-oxidative stability. Owing to the presence of bulky and rigid benzene rings in the backbone, PEI has high glass transition temperature (217 °C) and the high relative thermal index (170 °C) with long-term heat resistance. PEI also has a relatively good processability compared to other semi-crystalline PIs due to its amorphous nature based on the meta-phenylene moieties and the aryl ether linkage between aromatic rings, resulting in a decrease in the planarity and chain packing [71-73]. Therefore, it can be easily processed through conventional processing such as extrusion, injection, blow molding, solution casting and fiber spinning. Based on these advantageous features of PEI, it has been widely used in the high-performance applications such as aircraft, aerospace and automotive industries. However, its mechanical properties are still deficient compared to the semi-crystalline PI polymers. Thus, many researchers have focused on the improvement of the mechanical properties of PEI without significantly impairing other excellent properties [71, 72, 74, 75].

To improve the mechanical properties of amorphous PEI, various methods of film stretching [76] or blending with other semi-crystalline polymers [77-79] have been applied. In addition, PEI nanocomposites have been produced using rigid nanofillers [72, 78, 80-84]. Liu et al. fabricated PEI nanocomposite films by incorporating multi-walled carbon nanotubes (MWCNTs) and in-situ polymerization to enhance their thermal and mechanical properties [72]. With the addition of 1 wt.% of MWCNTs, the tensile strength and tensile modulus were increased by 22.6 and 39.5%, respectively. Further, Pitchan et al. used acid-functionalized MWCNTs for strong interaction with PEI polymers [83]. Their mechanical properties were improved by 15% in tensile strength and 7% in tensile modulus by adding 2 wt.% of MWCNT-COOH. PEI/organoclay nanocomposites were also prepared by Dwivedi et al. to enhance dielectric and tensile properties [81]. With 2 wt.% of organoclay, a 32% increase in tensile strength and 71% increase in tensile modulus were achieved. However, even though all of the above research has succeeded in raising the properties, there is still considerable scope for further enhancement. The structural changes of amorphous PEI chains on the incorporation of nanofillers under deformation have also not been analyzed in detail.

In recent years, various kinds of cellulosic materials have been considered as attractive candidates for nanofillers in nanocomposites because they are eco-friendly and are derived from abundant resources [3-5]. Among them, cellulose nanocrystals (CNC) can be of great interest based on the unique structural features such as their rod-shape with a high aspect ratio, high crystallinity (54-88%), and well-ordered crystal structure resulting from the removal of amorphous parts through acid hydrolysis of cellulose [1-3, 6]. Their theoretical mechanical properties are reported to be as high as 206 GPa in tensile modulus along the [001] plane and 10 GPa in tensile strength [2, 4, 85]. Moreover, the large surface area and the hydroxyl groups on their surfaces are very useful for hydrogen bonding with polymer matriices [1, 2, 4]. Therefore, CNC has already been used as a nanofiller in many nanocomposite systems [4, 5, 8-14], but there have been no previously reported attempts to make PEI/CNC nanocomposites.

In the current study, the control PEI and PEI/CNC nanocomposite fibers were prepared using a dry-jet wet spinning technique, followed by a post-drawing process to achieve the improved mechanical properties. The behavior of PEI polymer chains and CNCs with respect to the draw ratio and the amounts of CNC were also discussed thoroughly using scanning electron microscopy (SEM), dynamic mechanical analysis (DMA), transmission wide-angle X-ray diffraction (WAXD) and tensile testing.

## 4.2 Experimental

### *4.2.1 Material*

Polyetherimide (PEI, Ultem1000) was purchased from SABIC innovative plastics Co. The spray-dried CNC powders were purchased from CelluForce Co. The *N,N*-Dimethylacetamide (DMAc) and DI water were supplied by SamChun Co.

### *4.2.2 Solution Preparation*

The spray-dried CNC powders were dried at 70 °C overnight in vacuum oven before use. CNC was dispersed in DI water at a concentration of 3 wt.% using bath sonication for 72 h. Then, DMAc was added in the CNC/DI water dispersion (DMAc:DI water = 9:1 w/w%) by bath sonication for 72 h to obtain the well-dispersed CNC in mixed solvent.

The as-received PEI pellets were dried at 150 °C for 5 h in vacuum oven before use. For the control PEI fiber spinning, PEI polymer was dissolved in DMAc (70 g/100 mL) at 80 °C using an overhead mechanical stirrer. To prepare the PEI/CNC solution, CNC/DMAc/DI water dispersion was added to the PEI/DMAc solution. The excess amount of solvent was evaporated by vacuum distillation at 100 °C to obtain the desired solid concentration. These steps were repeated to obtain CNC concentrations of 1, 3 and 5 wt.% with respect to the total solid weight. The prepared spinning solutions were PEI, PEI/CNC1, PEI/CNC3 and PEI/CNC5 (hereafter, assigned to as control PEI, PCICNC1, PEICNC3, and PEICNC5, respectively).

### *4.2.3 Dry-jet wet spinning and post-drawing*

The control PEI and PEI/CNC nanocomposite fibers were prepared by dry-jet wet spinning technique using a custom-designed fiber spinning unit as shown in Figure 4.2 (a). The solution maintained at 75 °C was first spun at 5.7 m/min with the air gap of about 3 mm through the spinneret (8 holes, 150 μm diameter/ hole) and then introduced to a coagulation bath of DI water at 10 °C. The as-spun fibers were collected with a take-up roller at 16 m/min at room temperature. The spin-draw ratio (SDR) of as-spun fibers was 2.8. To remove the residual DMAc, the fibers were immersed in DI water for a day at room temperature. Then, post-drawing was performed using two heating rollers at 55 ℃ and target temperature from 75 to 165 ℃, respectively (Figure 4.2 (b)). To assess the structural development of the fibers upon drawing, the fibers were post-drawn at the post draw ratio (PDR) of 1.5, 2.0, 2.5 and so on. The post-drawing proceeded until the filament broke. The total draw ratio (TDR) was determined by multiplying SDR of 2.8 with PDR. Hereafter, draw ratio (DR) indicates TDR.

### *4.2.4 Characterization*

The fracture morphologies of cross-section of fibers were observed with a field emission scanning electron microscope (FE-SEM, Nanonova 230, FEI Co.) at an accelerating voltage of 10 kV after the sputter-coating with platinum at 20 mA for 60 s.

Tensile properties of the PEI and PEI/CNC nanocomposite fibers were measured with a single filament tensile tester (FAVIMAT+, Textechno, GmbH) at a strain rate of 1%/s and at a gauge length of 1 inch with a pretension of 1.0 cN/tex. Linear density of the fiber specimens was measured by a vibroscope attached to the tensile tester before tensile testing. The effective diameters of the monofilaments were calculated based on the measured linear density and the known bulk density of PEI (1.27 g/cm$^3$). At least 20 filaments were tested for each specimen for reliability.

To investigate the glass transition temperatures and chain relaxation behaviors of fibers, dynamic mechanical analysis (DMA, Q800, TA Instrument Inc.) were performed from 50 to 250 °C with a ramping rate of 3 °C/min at a frequency of 1 Hz.

Transmission wide-angle X-ray diffraction (WAXD) was conducted at the PLS- II 6D UNIST-PAL beamline of the Pohang Accelerator Laboratory in Pohang, Republic of Korea. The energy of the X-rays was 18.986 keV corresponding to a wavelength of 0.653 Å.

## 4.3. Result and Discussion

### *4.3.1 Post-drawing condition of PEI and PEI/CNC nanocomposite fibers*

The maximum drawing ratio at each drawing temperature is represented in Figure 4.3. At the higher drawing temperature, the PEI fibers tend to be further drawn, resulting in the larger value of the maximum DR (Figure 4.3a). Interestingly, the maximum DR jumped up at drawing temperature 105, 125 and 155 ℃, respectively. These temperatures seem to be related to the transition temperature of PEI. Fukuhara and Mikio studied the thermally activated structural change of PEI over a temperature range from -204 to 201 ℃ using the ultrasonic pulse method [71]. They concluded that the temperatures of 98, 122 and 157 ℃ are considered as the transition temperatures assigned to β- (softening-glass transition), rotational vibration of main benzene rings and a local relaxation of the main chain, respectively [71]. These transition temperatures correspond with the drawing temperature at which the PEI fibers can be further drawn by providing the thermal energy for mobility of polymer chains, resulting in the higher TDR [86, 87]. However, above 160 ℃, PEI filaments started to merge because PEI started to melt due to the residue solvent. As a result, the drawn fibers at 165 ℃ can't be separated into the monofilaments.

With incorporating CNCs into PEI fibers, the maximum TDR of nanocomposite fibers is lower compared to control PEI fibers at the same temperature (Figure 4.3b). This tendency seems to be from the constraint of chain mobility by the presence of CNCs [88, 89]. During spinning, PEI chains are deformed by shear stress and oriented [90]. The oriented chains are unstable state due to the low entropy at highly oriented state [87]. Therefore, the stretched PEI chains try to return the random-coiled state as soon as the solution gets out of the spinneret holes [87]. With incorporating CNCs, CNCs can be aligned along the shear direction due to rod shape with high aspect ratio [88, 89]. As a result, they forbid the mobility of PEI chains to some extent after initial deformation during spinning like fixing [88, 89]. As well as, with incorporation of CNC, the PEI/CNC nanocomposite fibers can't be drawn at higher temperature. Maybe, CNCs act as defects in fibers, resulting in the fracture during post-drawing.

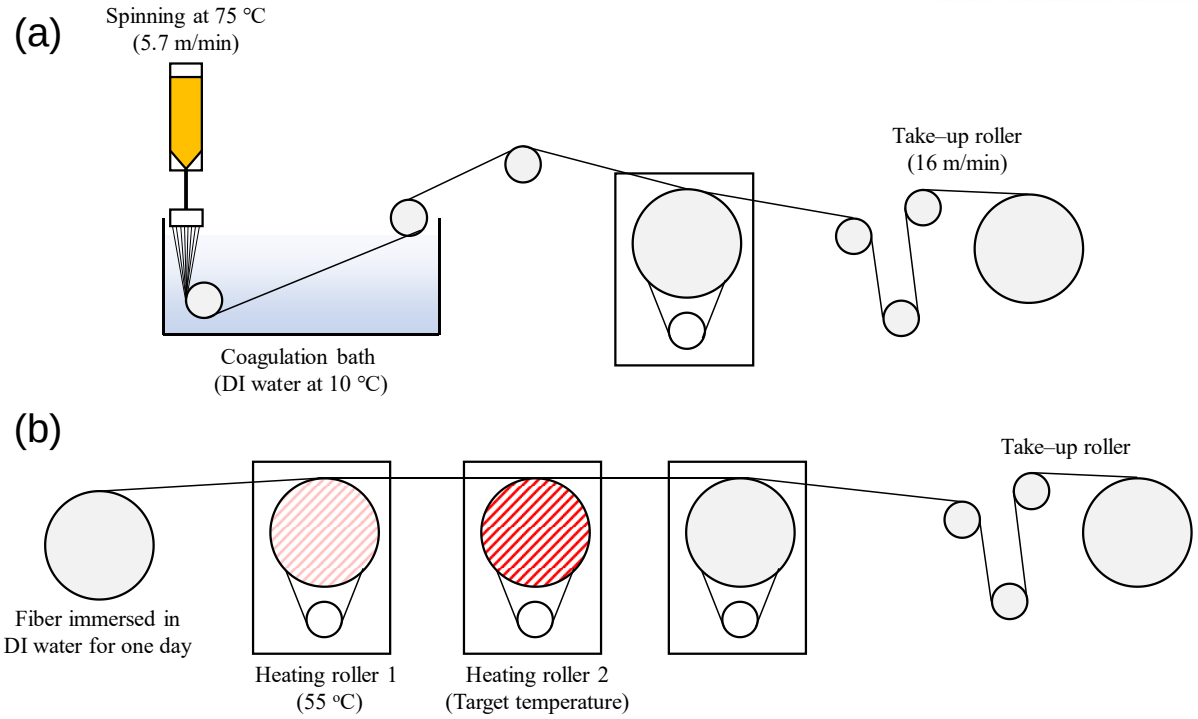


Figure 4.2 (a) The schematic descriptions of a (a) dry-jet wet spinning and a (b) post-drawing process.

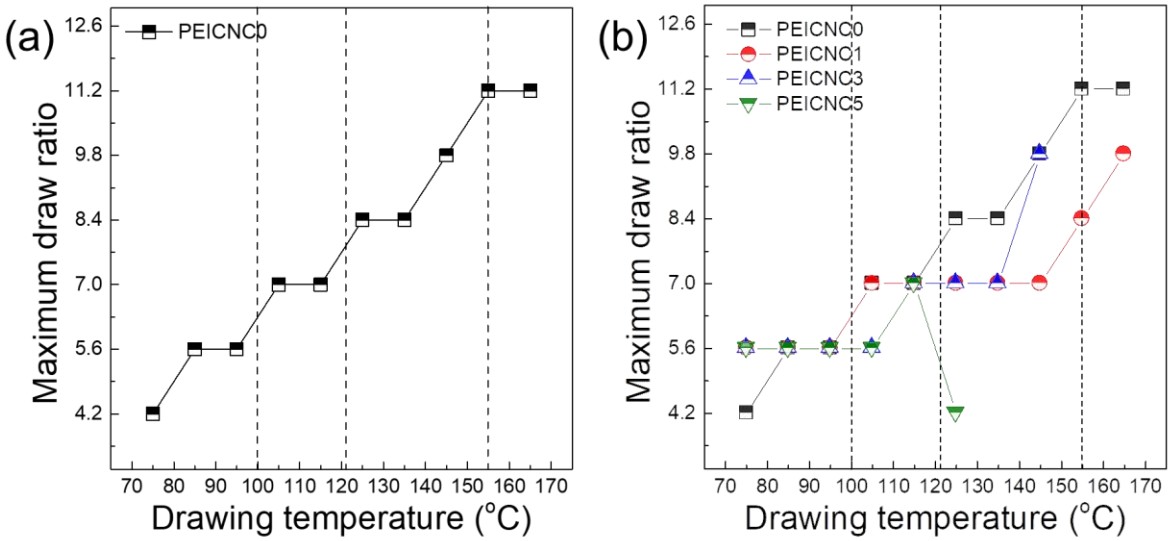


Figure 4.3 The maximum draw ratio of (a) control PEI and (b) PEI/CNC nanocomposite fibers at target temperature from 75 to 165 ℃.

### *4.3.2 The tensile properties of PEI and PEI/CNC nanocomposite fibers*

The tensile properties dependent on the content of CNC are represented in Table 4.1, 4.2, 4.3 and 4.4, respectively. With increasing DR at the same drawing temperature, the tensile strength and tensile modulus increased but the strain to failure and toughness as well as diameter decreased regardless of the contents of CNC. The more stretched state of polymer chains, the higher force is required for initial deformation, resulting in the high modulus [91, 92]. It is interesting that the tensile strength and modulus of the further drawn fibers with DR 8.4, 9.8 and 11.2 above 145 ℃ are lower or similar with those of the drawn fibers with low DR below 115 ℃. It seems to be the release of entanglement of polymer chains by the chain slippery during post-drawing at the high temperature, followed by the rapid relaxation due to the high thermal energy to provide the chain mobility [87, 90]. At the low temperature such as 75 and 85 ℃, the oriented state can be fixed to some extent without the relaxation as much as the one of high temperature [87]. Interestingly, the maximum TDR is same at 115 ℃ regardless of the content of CNC. Therefore, the drawn fibers at 115 ℃ were selected to examine the effect of CNCs into the behavior of PEI chains in fiber with various draw ratio.

The tendencies about tensile properties of drawn fibers at 115 ℃ are indicated in Figure 4.4. The stress-strain curves for each fiber are also shown in Figure 4.5. The yielding and strain hardening behavior of fibers decreases, regardless of the concentration of CNC. This may be due to the reduced occurrence of plastic deformation until the entanglement between PEI chains is released and the fibers are broken as the chains become extended by tensile force [72, 77, 93]. Consequently, the strain to failure and toughness also decreased while the tensile strength and modulus were improved about 200-300% by 2.5 times of post-drawing. On the other hand, according to the CNC amount, an increase in tensile modulus and a decrease in the tensile strength and toughness were observed. Dwivedi et al. also observed the same tendency when nanofillers were incorporated in PEI films [81, 94]. They suggested that nanofillers can lead to discontinuity among the polymeric chains in the role of a plasticizer, causing strength reduction. Tensile modulus, however, is known to be related to the crystal size and the degree of orientation of the microstructure [95]. Since the PEI used in this study is an amorphous polymer that cannot be crystallized, the improved tensile modulus is expected to be influenced by the degree of orientation of the PEI chains and CNC, and the high specific modulus (~150 GPa) of the CNC itself [4, 84, 85]. The interaction with CNC can also contribute to stiffness as it prevents deformation under tension [96]. At TDR 7.0, the tensile strength of the control and PEICNC5 fibers were 466.2 and 348.0 MPa, and the tensile moduli of those fibers were 8.1 and 9.3 GPa, respectively. Notably, the reduction rate of tensile strength and toughness was lowest in the PEICNC3 fiber compared with the control fiber, and the tensile modulus was as high as that of PEICNC5 fiber at all DR. Therefore, 3 wt.% of CNC in PEI nanocomposite fibers seems to be an appropriate amount to produce relatively high values of all

mechanical properties with strong interaction between them, which agrees well with the DMA result (It will be discussed in section 3.3.4). For comparison of the mechanical properties of these dry-jet wet spun PEI fibers and various PEI-based nanocomposite systems, each tensile strength and modulus value is exhibited in Figure 4.4d [72, 78, 80-84, 97, 98]. The properties in the current study are the highest among reported values so far, with a large difference compared to others. This is due to the processing conditions: a dry-jet wet spinning method developed by Dupont Co. for high DR, and post-drawing [99]. These data also verified the effects of DR on mechanical properties are greater than those of CNC (Figures 3.4a-c), indicating that extension of the polymeric chain, even in the amorphous polymer is very useful for enhancing properties, rather than the addition of nanofillers.

Table 4.1 Tensile properties of control PEI fiber

| Drawing Temp (°C) | Draw ratio | Diameter (um) | Tensile Strength (MPa) | Tensile Modulus (GPa) | Strain to failure (%) | Toughness (J/g) |
|---|---|---|---|---|---|---|
| As-spun: 2.8 | | 44.8 ± 0.9 | 163.4 ± 26.2 | 3.6 ± 0.1 | 184.7 ± 53.4 | 181.8 ± 68.0 |
| 75 | 4.2 | 37.7 ± 0.7 | 280.4 ± 41.2 | 6.0 ± 0.2 | 93.7 ± 28.3 | 169.5 ± 59.2 |
| 85 | 4.2 | 38.8 ± 0.4 | 267.0 ± 38.0 | 5.6 ± 0.1 | 96.8 ± 32.6 | 165.6 ± 62.9 |
| | 5.6 | 34.6 ± 0.8 | 346.3 ± 42.8 | 7.0 ± 0.3 | 50.6 ± 20.8 | 117.4 ± 54.6 |
| 95 | 4.2 | 38.4 ± 1.1 | 255.6 ± 41.7 | 5.8 ± 0.3 | 72.9 ± 30.8 | 123.3 ± 63.5 |
| | 5.6 | 33.9 ± 0.5 | 371.2 ± 35.4 | 6.9 ± 0.2 | 49.3 ± 12.8 | 118.2 ± 35.0 |
| 105 | 4.2 | 38.9 ± 0.9 | 258.7 ± 43.6 | 5.5 ± 0.3 | 82.0 ± 33.5 | 139.6 ± 68.9 |
| | 5.6 | 33.9 ± 0.5 | 361.6 ± 50.7 | 7.0 ± 0.3 | 52.7 ± 22.2 | 127.5 ± 60.4 |
| | 7.0 | 30.2 ± 0.5 | 433.6 ± 46.9 | 8.1 ± 0.3 | 28.5 ± 13.4 | 82.2 ± 44.7 |
| 115 | 4.2 | 38.7 ± 0.6 | 252.5 ± 43.7 | 5.5 ± 0.2 | 77.9 ± 32.4 | 132.0 ± 64.7 |
| | 5.6 | 33.6 ± 0.5 | 372.7 ± 40.4 | 7.1 ± 0.3 | 53.9 ± 19.2 | 132.4 ± 52.3 |
| | 7.0 | 29.9 ± 0.7 | 466.2 ± 38.9 | 8.1 ± 0.3 | 39.9 ± 10.9 | 120.9 ± 36.2 |
| 125 | 4.2 | 38.4 ± 0.6 | 253.0 ± 43.7 | 5.1 ± 0.1 | 92.1± 35.1 | 152.1 ± 67.4 |
| | 5.6 | 34.1 ± 0.8 | 345.3 ± 39.6 | 6.3 ± 0.3 | 60.6 ± 13.7 | 134.5 ± 36.5 |
| | 7.0 | 30.6 ± 0.6 | 435.3 ± 32.5 | 7.4 ± 0.3 | 41.4 ± 8.1 | 115.0 ± 26.6 |
| | 8.4 | 28.3 ± 0.5 | 568.8 ± 56.2 | 8.7 ± 0.4 | 24.2 ± 6.0 | 83.4 ± 25.6 |
| 135 | 4.2 | 37.5 ± 0.9 | 253.7 ± 38.9 | 4.9 ± 0.3 | 95.2 ± 27.7 | 151.2 ± 54.9 |
| | 5.6 | 33.1 ± 0.9 | 348.8 ± 32.4 | 6.1 ± 0.2 | 59.7 ± 11.9 | 130.5 ± 31.7 |
| | 7.0 | 30.8 ± 0.8 | 423.2 ± 42.6 | 7.3 ± 0.2 | 33.2 ± 10.8 | 87.1 ± 33.9 |
| | 8.4 | 28.7 ± 0.7 | 448.9 ± 48.1 | 7.5 ± 0.3 | 27.7 ± 8.1 | 76.2 ± 27.4 |
| 145 | 4.2 | 38.5 ± 1.9 | 263.7 ± 39.0 | 4.5 ± 0.3 | 105.7 ± 25.0 | 163.9 ± 43.1 |
| | 5.6 | 33.6 ± 1.1 | 335.2 ± 33.9 | 5.1 ± 0.3 | 67.0 ± 11.8 | 128.1 ± 31.4 |
| | 7.0 | 30.2 ± 0.7 | 409.8 ± 40.0 | 6.6 ± 0.2 | 39.3 ± 7.5 | 96.6 ± 24.1 |
| | 8.4 | 28.3 ± 0.7 | 390.4 ± 49.6 | 6.6 ± 0.6 | 26.7 ± 4.0 | 60.6 ± 12.4 |
| | 9.8 | 26.7 ± 0.6 | 421.6 ± 27.7 | 6.6 ± 0.3 | 19.6 ± 2.7 | 46.9 ± 7.7 |
| 155 | 4.2 | 38.2 ± 1.1 | 220.7 ± 39.2 | 4.4 ± 0.2 | 93.8 ± 26.1 | 129.6 ± 48.0 |
| | 5.6 | 34.0 ± 1.0 | 320.3 ± 22.3 | 4.9 ± 0.2 | 78.7 ± 10.8 | 142.5 ± 24.1 |
| | 7.0 | 30.1 ± 0.5 | 297.4 ± 27.1 | 4.9 ± 0.2 | 45.8 ± 5.9 | 77.0 ± 15.1 |
| | 8.4 | 28.4 ± 0.8 | 330.9 ± 44.0 | 5.6 ± 0.5 | 28.8 ± 4.4 | 54.4 ± 8.5 |
| | 9.8 | 25.3 ± 0.8 | 198.0 ± 8.5 | 4.7 ± 0.2 | 28.0 ± 4.5 | 35.0 ± 5.3 |
| | 11..2 | 27.0 ± 1.0 | 308.7 ± 38.5 | 5.5 ± 0.3 | 23.2 ± 2.6 | 42.2 ± 7.3 |

Table 4.2 Tensile properties of PEICNC1 fibers

| Drawing Temp (°C) | Draw ratio | Diameter (um) | Tensile Strength (MPa) | Tensile Modulus (GPa) | Strain to failure (%) | Toughness (J/g) |
|---|---|---|---|---|---|---|
| As-spun: 2.8 | | 46.1 ± 0.7 | 154.2 ± 6.6 | 4.0 ± 0.1 | 168.4 ± 10.4 | 159.2 ± 13.1 |
| 75 | 4.2 | 35.8 ± 0.6 | 232.5 ± 11.0 | 6.1 ± 0.2 | 76.0 ± 5.0 | 120.0 ± 8.1 |
| | 5.6 | 31.7 ± 0.5 | 307.4 ± 16.9 | 7.8 ± 0.3 | 37.2 ± 4.4 | 79.3 ± 10.8 |
| 85 | 4.2 | 36.1 ± 0.9 | 227.2 ± 13.8 | 6.1 ± 0.4 | 72.2 ± 7.1 | 114.0 ± 12.3 |
| | 5.6 | 31.5 ± 0.6 | 301.7 ± 17.0 | 7.8 ± 0.3 | 34.6 ± 4.8 | 73.4 ± 11.1 |
| 95 | 4.2 | 35.9 ± 0.9 | 231.9 ± 21.1 | 6.0 ± 0.4 | 78.1 ± 10.6 | 123.4 ± 19.3 |
| | 5.6 | 31.5 ± 0.4 | 290.7 ± 15.6 | 7.6 ± 0.2 | 28.6 ± 11.7 | 58.3 ± 28.0 |
| 105 | 4.2 | 36.3 ± 0.8 | 220.1 ± 13.1 | 5.8 ± 0.3 | 70.1 ± 12.0 | 100.6 ± 39.7 |
| | 5.6 | 31.0 ± 0.8 | 331.5 ± 18.7 | 8.0 ± 0.4 | 37.5 ± 2.7 | 85.2 ± 6.3 |
| | 7.0 | 28.5 ± 0.9 | 395.0 ± 24.8 | 8.5 ± 0.4 | 20.7 ± 3.9 | 53.8 ± 10.6 |
| 115 | 4.2 | 35.9 ± 1.0 | 224.8 ± 14.7 | 5.8 ± 0.3 | 70.7 ± 7.2 | 110.3 ± 13.1 |
| | 5.6 | 31.3 ± 1.1 | 313.2 ± 21.0 | 7.4 ± 0.3 | 35.3 ± 4.7 | 75.2 ± 8.9 |
| | 7.0 | 28.5 ± 0.7 | 405.5 ± 24.3 | 8.8 ± 0.5 | 19.9 ± 2.8 | 53.0 ± 9.3 |
| 125 | 4.2 | 36.0 ± 0.9 | 235.6 ± 13.4 | 5.9 ± 0.2 | 74.3 ± 10.3 | 118.3 ± 13.9 |
| | 5.6 | 32.4 ± 0.6 | 326.7 ± 17.5 | 7.3 ± 0.3 | 40.0 ± 4.0 | 87.3 ± 10.2 |
| | 7.0 | 28.7 ± 0.9 | 443.1 ± 24.3 | 8.9 ± 0.7 | 26.2 ± 3.6 | 74.7 ± 8.6 |
| 135 | 4.2 | 35.9 ± 0.8 | 257.4 ± 18.2 | 6.1 ± 0.3 | 77.4 ± 13.0 | 131.4 ± 24.0 |
| | 5.6 | 32.4 ± 0.6 | 333.5 ± 15.5 | 7.3 ± 0.3 | 42.4 ± 4.5 | 92.2 ± 10.0 |
| | 7.0 | 29.6 ± 0.9 | 414.1 ± 23.8 | 7.9 ± 0.3 | 28.6 ± 3.8 | 74.4 ± 10.6 |
| 145 | 4.2 | 37.3 ± 0.8 | 245.9 ± 16.6 | 5.5 ± 0.3 | 90.2 ± 4.2 | 140.2 ± 7.1 |
| | 5.6 | 32.8 ± 0.8 | 316.1 ± 19.0 | 6.3 ± 0.3 | 48.6 ± 6.7 | 94.5 ± 13.4 |
| | 7.0 | 29.7 ± 1.2 | 375.0 ± 21.4 | 7.2 ± 0.5 | 31.2 ± 4.4 | 71.6 ± 10.4 |
| 155 | 4.2 | 36.5 ± 1.0 | 237.3 ± 16.1 | 5.4 ± 0.3 | 85.8 ± 4.6 | 127.3 ± 5.5 |
| | 5.6 | 32.3 ± 1.3 | 297.6 ± 30.0 | 6.0 ± 0.3 | 55.2 ± 7.2 | 99.8 ± 16.6 |
| | 7.0 | 29.5 ± 1.0 | 293.2 ± 27.1 | 6.1 ± 0.4 | 34.3 ± 5.0 | 61.6 ± 10.5 |
| | 8.4 | 26.9 ± 0.4 | 404.7 ± 28.1 | 7.7 ± 0.3 | 24.4 ± 5.4 | 60.5 ± 15.3 |

Table 4.3 Tensile properties of PEICNC3 fibers

| Drawing Temp (°C) | Draw ratio | Diameter (um) | Tensile Strength (MPa) | Tensile Modulus (GPa) | Strain to failure (%) | Toughness (J/g) |
|---|---|---|---|---|---|---|
| As-spun: 2.8 | | 42.4±0.7 | 150.8±5.7 | 4.9±0.1 | 148.9±11.3 | 147.2±12.8 |
| 75 | 4.2 | 34.5±0.8 | 233.7±8.7 | 7.0±0.4 | 75.9±6.3 | 119.6±7.0 |
| | 5.6 | 31.0±0.4 | 299.1±6.0 | 8.3±0.2 | 45.9±1.9 | 93.2±3.9 |
| 85 | 4.2 | 34.9±0.7 | 228.9±8.6 | 6.9±0.3 | 80.3±9.8 | 123.3±12.2 |
| | 5.6 | 30.8±0.4 | 302.0±7.8 | 8.5±0.2 | 43.1±3.1 | 88.3±6.4 |
| 95 | 4.2 | 34.3±2.3 | 221.6±26.1 | 6.9±0.8 | 69.7±11.8 | 105.7±16.4 |
| | 5.6 | 31.1±0.4 | 293.8±4.9 | 8.2±0.2 | 39.1±6.4 | 79.3±12.1 |
| 105 | 4.2 | 35.5±0.5 | 218.5±8.0 | 6.4±0.1 | 82.1±9.5 | 120.3±11.2 |
| | 5.6 | 30.8±0.6 | 297.5±10.1 | 8.2±0.2 | 40.8±4.6 | 82.2±7.8 |
| 115 | 4.2 | 35.0±0.6 | 243.2±14.9 | 6.6±0.3 | 91.0±10.3 | 243.2±14.9 |
| | 5.6 | 30.7±0.4 | 340.0±9.7 | 8.2±0.2 | 51.6±3.7 | 114.8±9.3 |
| | 7.0 | 27.9±0.5 | 408.9±20.9 | 9.2±0.3 | 31.9±1.8 | 83.7±5.2 |
| 125 | 4.2 | 34.9±1.4 | 231.3±28.3 | 6.4±0.5 | 88.0±6.6 | 132.8±8.3 |
| | 5.6 | 30.7±0.4 | 321.9±9.9 | 7.7±0.2 | 49.3±3.3 | 101.6±5.6 |
| | 7.0 | 28.2±0.4 | 395.9±12.1 | 8.6±0.2 | 34.2±2.9 | 85.3±7.7 |
| 135 | 4.2 | 34.5±0.7 | 249.7±12.5 | 6.6±0.3 | 98.0±8.2 | 156.1±15.0 |
| | 5.6 | 30.9±0.7 | 322.2±15.9 | 7.2±0.2 | 51.6±5.3 | 103.6±12.5 |
| | 7.0 | 28.4±0.6 | 380.8±14.5 | 8.0±0.2 | 36.7±1.9 | 84.8±5.6 |
| 145 | 4.2 | 36.0±0.8 | 213.9±20.6 | 6.0±0.2 | 90.8±13.0 | 125.3±22.5 |
| | 5.6 | 32.1±1.4 | 281.9±36.4 | 6.6±0.4 | 53.4±5.0 | 92.7±16.3 |
| | 7.0 | 29.0±0.9 | 327.7±12.3 | 7.1±0.4 | 35.0±3.8 | 68.8±7.5 |

Table 4.4 Tensile properties of PEICNC5 fibers

| Drawing Temp (°C) | Draw ratio | Diameter (um) | Tensile Strength (MPa) | Tensile Modulus (GPa) | Strain to failure (%) | Toughness (J/g) |
|---|---|---|---|---|---|---|
| As-spun: 2.8 | | 43.0±0.6 | 133.0±7.2 | 4.8±0.2 | 127.9±15.8 | 115.8±16.5 |
| 75 | 4.2 | 36.3±0.9 | 196.7±13.9 | 6.6±0.3 | 64.2±8.8 | 89.3±24.4 |
| | 5.6 | 30.8±0.8 | 285.1±15.6 | 8.6±0.3 | 28.4±6.3 | 56.3±14.6 |
| 85 | 4.2 | 35.2±0.9 | 212.1±14.0 | 7.1±0.4 | 65.0±6.5 | 99.4±11.9 |
| | 5.6 | 31.4±0.8 | 273.8±14.2 | 8.3±0.3 | 30.0±7.4 | 53.8±20.7 |
| 95 | 4.2 | 35.2±1.1 | 207.0±10.7 | 6.8±0.3 | 56.8±8.7 | 85.0±12.6 |
| | 5.6 | 31.1±0.7 | 280.4±20.5 | 8.1±0.3 | 29.0±7.0 | 55.0±19.2 |
| 105 | 4.2 | 36.0±1.1 | 200.3±9.8 | 6.7±0.4 | 61.2±12.3 | 81.6±34.2 |
| | 5.6 | 30.8±0.7 | 292.4±12.4 | 8.3±0.3 | 32.2±3.7 | 65.4±7.4 |
| 115 | 4.2 | 35.7±0.7 | 203.7±13.4 | 6.8±0.2 | 62.2±9.7 | 85.9±30.8 |
| | 5.6 | 31.4±0.4 | 285.7±10.8 | 8.1±0.3 | 34.0±5.7 | 63.8±20.6 |
| | 7.0 | 28.8±0.7 | 348.0±19.5 | 9.3±0.3 | 17.3±4.4 | 38.9±11.7 |
| 125 | 4.2 | 35.1±1.1 | 203.8±21.9 | 6.5±0.5 | 60.6±17.6 | 89.5±30.2 |

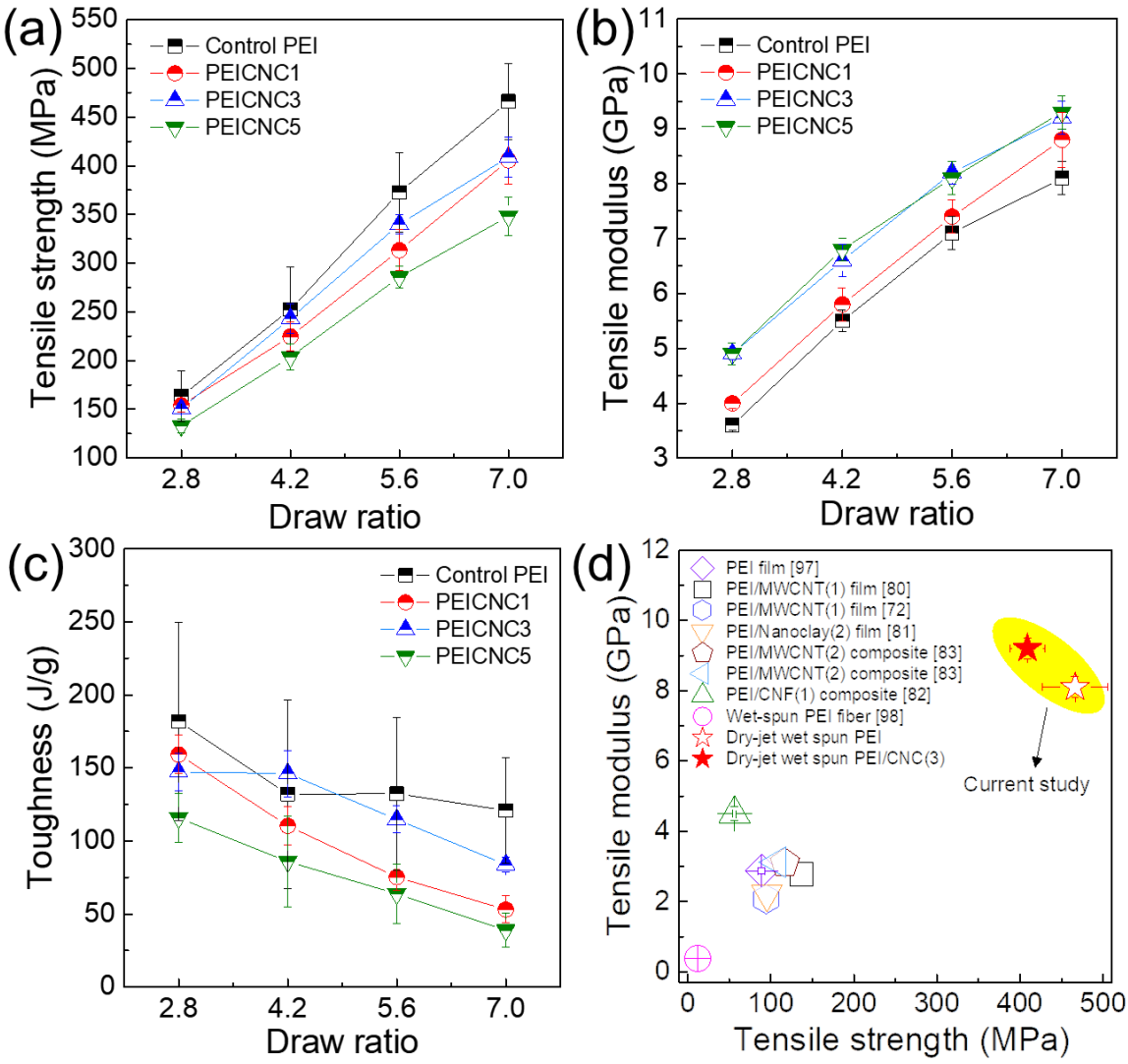


Figure 4.4 The behavior of (a) tensile strength, (b) tensile modulus and (c) toughness of drawn fibers at 115 ℃, depending on the various DR and the amount of CNCs. (d) Comparison of mechanical properties of PEI-based fibers. The numbers in legend parenthesis of d represent wt.% of nanofiller with respect to the PEI matrix.

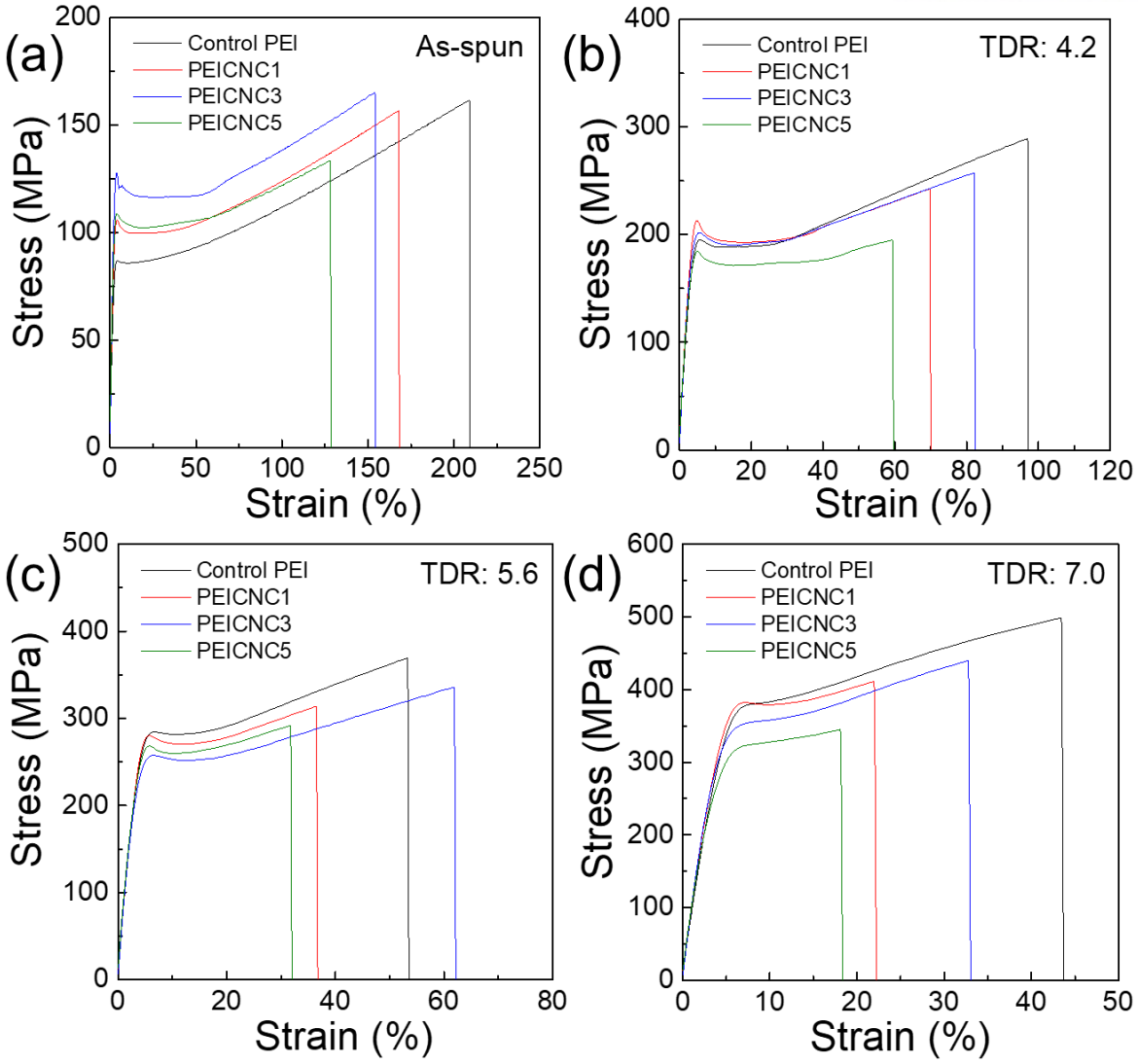


Figure 4.5 Stress-strain curves of control PEI and PEI/CNC nanocomposite fibers, which were drawn at 115 ℃. The total draw ratio is (a) 2.8 (as-spun), (b) 4.2, (c) 5.6 and (d) 7.0, respectively.

### *4.3.3 Fiber morphology of PEI and PEI/CNC nanocomposite fibers*

Figure 4.6 shows SEM images of cross-sections of dry-jet wet spun fibers with CNC contents and draw ratio. All fibers are drawn fibers at 115 ℃ and exhibit circular cross-sectional shape. In fracture images of the control PEI and PEICNC1 fibers (Figures 4.6), the crack initiation points are marked on the fiber skin as red arrows. The fracture was likely to start in the skin region and then propagated to the core due to heterogeneous stress distribution based on the irregular structure of fibers [100]. However, in the nanocomposite fibers with high contents of CNC (the two bottom lines), the specific fracture source is not observed suggesting the tensile force was evenly distributed based on the structural uniformity of fibers.

Figure 4.7 represents the magnified SEM images of the domains within the monofilament of fibers. It is important to note that the fibrous domain size was significantly increased even by the addition of 1 wt.% of CNC when compared to the control PEI fiber, due to hydrogen bonding between the carbonyl or ether groups of PEI chains and the hydroxyl groups of CNC [101-104].

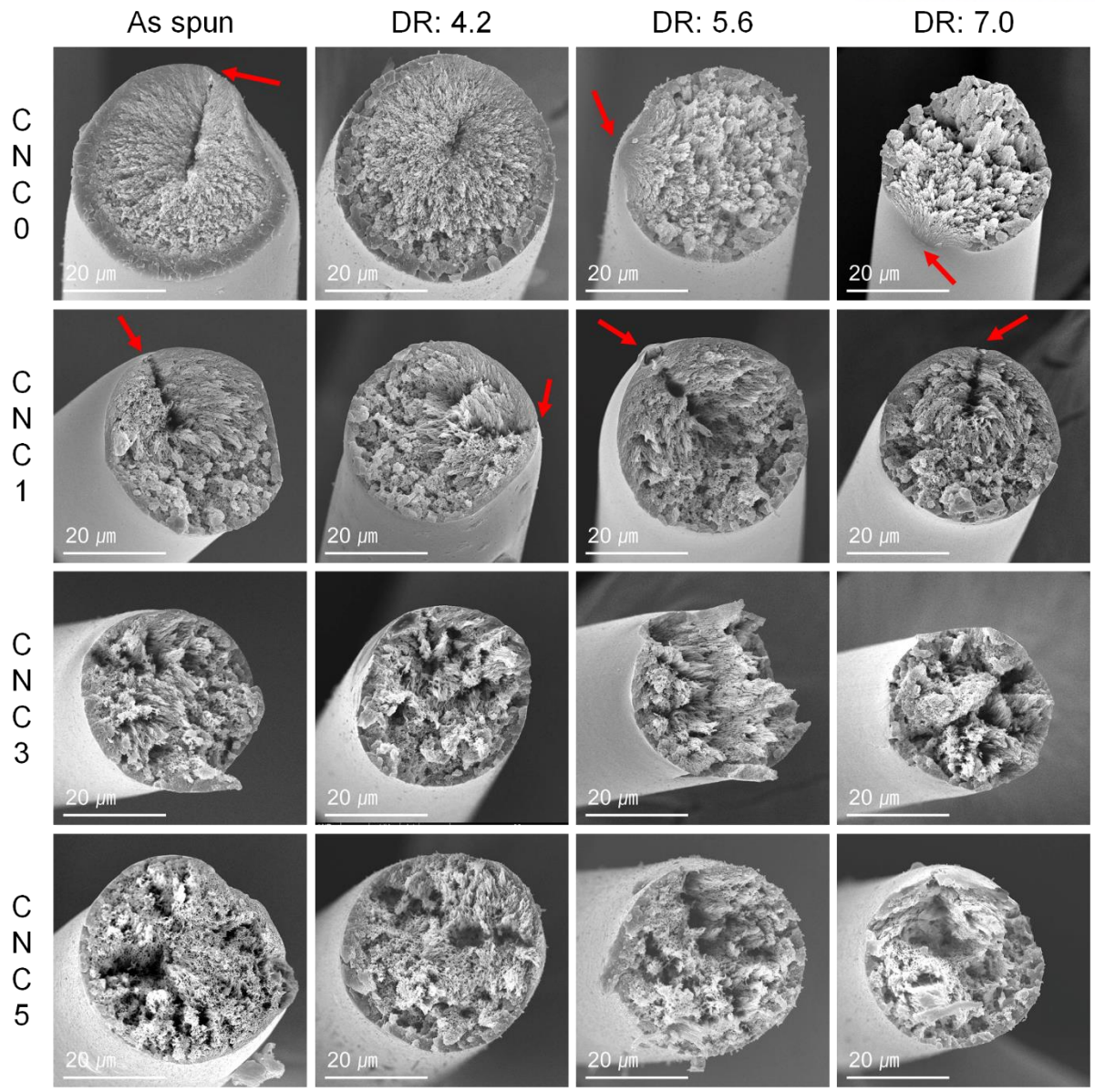


Figure 4.6 SEM image of cross-sections of control PEI and PEI/CNC nanocomposites drawn at 115 ℃. The red arrows indicate the crack initiation points on the surface of PEI fibers.

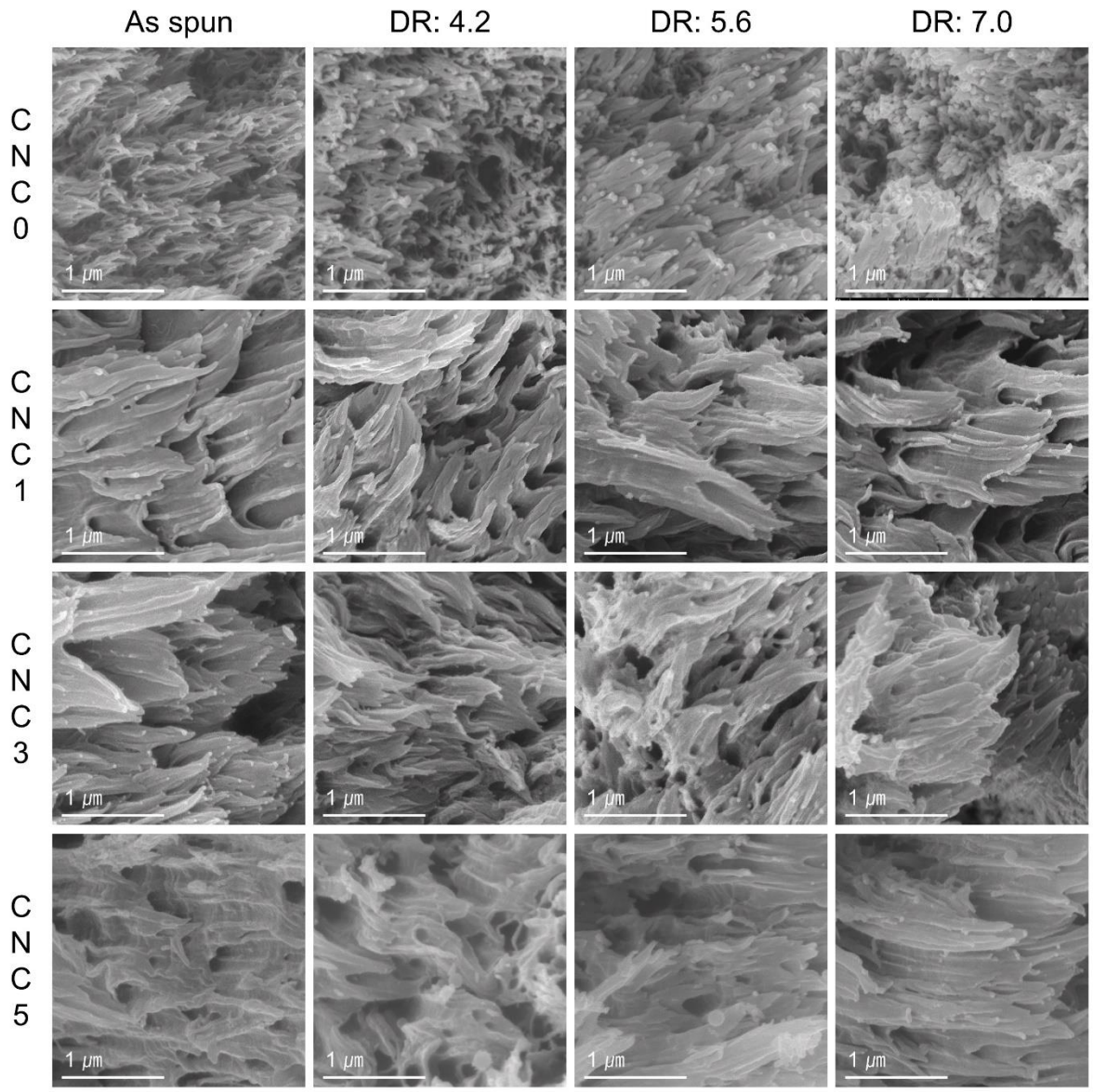


Figure 4.7 The magnified SEM image of cross-sections of control PEI and PEI/CNC nanocomposites drawn at 115 ℃.

### *4.3.4 The glass transition temperature of PEI and PEI/CNC nanocomposite fibers*

The molecular mobility as reflected by the glass transition temperature ($T_g$) can also be considered as a criterion of interaction between the polymeric chain and nanofillers [72, 105]. Figure 4.8 displays the storage modulus and loss factor curves (tan δ) of fibers with a DR of 7, showing that the magnitude of tan δ decreases and the $T_g$ increases with the amount of CNC. The $T_g$ of control and CNC5 fibers were 227.6 and 232.6 °C, and the value of tan δ at the $T_g$ were 1.82 and 0.93, respectively. These results indicate the restricted segmental motion of PEI chains by strong interaction with CNC (Figure 4.7).

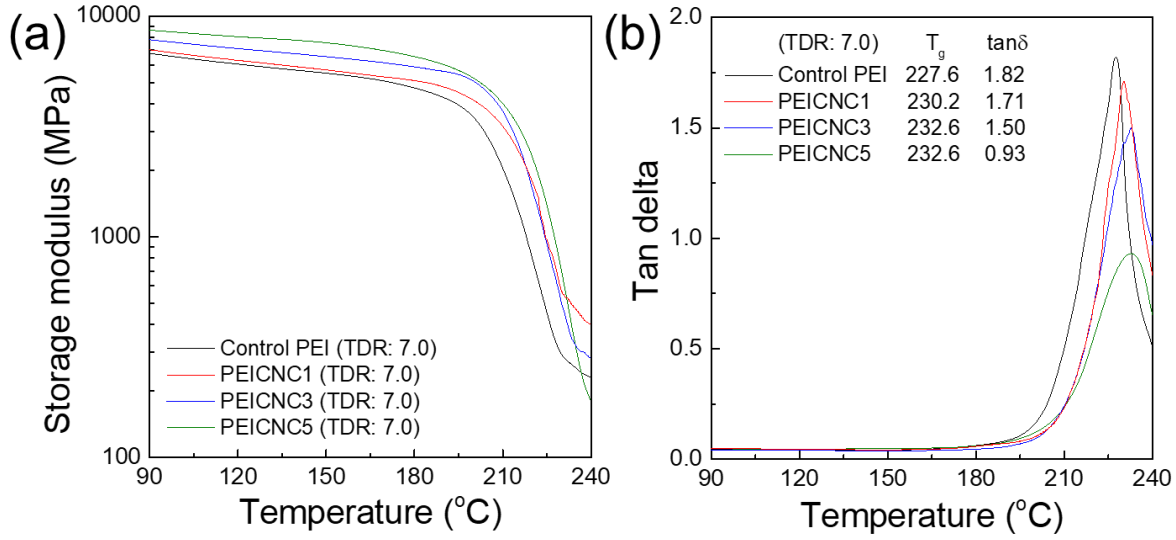


Figure 4.8 (a) Storage modulus and (b) loss factor (tan δ) curves of fibers with DR of 7.0. The $T_g$ and the magnitude of tan δ at the $T_g$ are represented in the legend of b.

### *4.3.5 Chain orientation and CNC alignment of PEI and PEI/CNC nanocomposite fibers*

To examine the orientation behavior of the PEI polymeric chain and CNC in the fibers as a function of TDR and the amount of CNC, WAXD pattern images are shown in Figure 4.9 and each peak is assigned in Figure 4.10. Three major crystal planes: (110), (200), and (004) of CNC are apparently observed [3, 85, 106, 107]. From the as-spun fiber, the (110) and (200) planes are already aligned along the fiber axis, and the (004) plane is in the transverse direction of the fibers, indicating that the CNCs can be arranged even at low TDR. Their orientation increases further upon post-drawing and the arcs which refers to each peak become small spots with high intensity. The control PEI shows four broad amorphous halos according to the intersegmental distance of chains [108]. All peaks except peak 1 are ring-shaped in the pattern images of as-spun fibers caused by the isotropic arrangement of PEI chains. Among them, peaks 2 and 3 become clearly aligned in the axial direction during drawing while peak 4 shows a slight change with respect to the TDR and the amounts of CNC. Despite the amorphous nature, it has already been confirmed that the chains can be oriented along the direction of tensile force [109-113]. Murthy et al. proved the amorphous chain segments were oriented parallel to the drawing direction and packed more densely than in the perpendicular direction [112]. They also confirmed that the density of the amorphous phase is different in the two directions. Further, Leal et al. pointed out that the amorphous polymer can have a preferred alignment direction and interchain distance between the polymeric chains by drawing [110]. Peak 1 of PEI, which is not seen in the as-spun fiber, appears after post-drawing and becomes clear with increasing TDR. This meridian peak does not originate from the molecular structure of PEI but there is a long-range order based on the highly extended state of chains with regular periodicity, as also observed in the oriented semi-crystalline polymeric chains just before crystallization [114, 115], or highly drawn amorphous polymers [113]. The small-angle X-ray scattering (SAXS) patterns in the 2D WAXD pattern images reflect the shape of the micro-voids as represented in the inset images of Figure 4.9. As the TDR increases, the SAXS pattern changes from circular to a diamond shape and the area where the SAXS intensity appears become narrow. These results arise from the change of micro-voids to an elongated shape along the fiber axis with the improvement of alignment of microstructure and micro-voids [116]. Hence, it seems that post-drawing contributes greatly to structural alignment.

Figures 3.11-3.13 show the integrated, equatorial and meridional scans of PEI-based fibers, respectively. To investigate the change in intensity of various peaks upon drawing, the integrated and equatorial scans were normalized by peak 2 and the meridional scan was normalized by peak 4 of PEI. In all the spectra, the intensity of sharp CNC peaks increases with respect to the amount of CNC. In particular, as shown in the 2D pattern images (Figure 4.9), CNC(200) is more obvious in the equatorial scan while the CNC(004) is more obvious in the meridional scan based on its orientation. The change of peaks is not well observed in the equatorial scan because the intensity of peak 4 and CNC(004) are

too small compared to peak 2 (Figure 4.12). In the meridional scan (Figure 4.13), the peak intensity in the range of 10-30 ° of 2θ decreases and that of CNC(004) increases dramatically with CNC content. Given that the change in peak 4 with CNC content in the equatorial scan is very subtle, it is thought that the orientation of the (110) and (200) planes of CNC to the axial direction has a significant effect on the intensity reduction in the 10-30 ° range, rather than the influence of PEI. On the basis of post-drawing, the relative intensity of peak 4 compared to peak 2 increases, suggesting the alignment of fiber structures.

Azimuthal scans of peak 2 of PEI with CNC(110) of fibers are shown in Figure 4.14, and those of peak 3 with CNC(200) are shown in Figure 4.15. Since the PEI and CNC peaks in each figure appear at the same 2θ position in the WAXD spectrum, the azimuthal scan also shows their superimposed spectra. Both azimuthal peaks in Figures 4.14 and 4.15 are observed at 90° of azimuthal angle due to the alignment along the fiber axis. On the other hand, the azimuthal angle of the meridian CNC(004) peak is 180°, which is normal to the fiber axis (Figure 4.16). It is noticeable that the azimuthal peak of CNC(004), which is related to the orientation of CNC alone, is much sharper than the peak from PEI mixed with CNC. Based on these results, their calculated Hermann's orientation factors are also several times different in the PEI nanocomposite fibers, as exhibited in Table 4.5 [117]. This means that the degree of orientation of the crystalline phase, CNC, is much higher than that of the amorphous PEI. With increasing DR and CNC amounts, all azimuthal peaks mentioned above become sharper and each PEI and CNC peaks in the overlapped spectrum become distinguishable as the difference of orientation between amorphous and crystalline phase increases.

For detailed analysis of the orientation of PEI polymeric chains, the overlapped spectra observed in the equatorial direction were deconvoluted (Figure 4.17) [118]. In addition, the orientation factors of each PEI ($f_{PEI}$) and CNC ($f_{CNC}$) after deconvolution are shown in Table 4.6 and Figure 4.18. The change of the degree of orientation of the overall spectrum (before deconvolution) according to the DR is easily observed while a very slight change by CNC amounts in the fibers. After deconvolution, it is confirmed that the CNCs are arranged continuously along the fiber axis with increasing DR and the amounts of CNC, which is in accord with the change of $f_{CNC(004)}$. However, the behavior of $f_{PEI}$ with the CNC amounts is noticeably different from that of $f_{CNC}$. The value of $f_{PEI}$ is highest in the control fiber and is dramatically reduced by the addition of 1 wt.% of CNC. Although $f_{PEI}$ increases slowly again to the 5 wt.% of CNC, the value is still lower than in the control fibers at all DR, indicating the negative effect of CNC on the arrangement of PEI chains. It is already known from the previous study that amorphous orientation is interrupted by a crystalline phase [119]. Hence, it is thought that the amorphous PEI chain around the rigid crystalline CNC with highly anisotropic arrangement cannot be aligned as chains in the control fiber no matter how they interact, as shown in Figure 4.19. Another point to note is that the value of $f_{CNC}$ is much higher than that of $f_{PEI}$, and it starts to develop from quite a high value

as a function of DR and CNC amounts. Also, the rapid development of crystalline orientation along the fiber axis was observed as compared with the slower development of amorphous orientation, which is common behavior for flexible chain polymers [120, 121]. In order to compare the degree of orientation of each phase under tensile deformation, the behavior of $f_{PEI}$ and $f_{CNC}$ for CNC5 fibers is exhibited in figure 4.20. Peaks 2 and 3 of PEI show a low orientation factor of 0.01-0.18 even after drawing to a maximum extent, but CNC is highly oriented, with $f_{CNC(110)}$ increasing from 0.46 to 0.61 and $f_{CNC(200)}$ from 0.63 to 0.75 upon drawing. The difference in molecular orientation is a common phenomenon not only in PEI/CNC nanocomposites but also in other mixed systems of amorphous and crystalline phases [122]. This is attributed to their two main structural differences: entanglement and molecular cohesion [123]. Firstly, entanglement in the amorphous phase limits segmental extensibility, especially in the entanglement junctions [120, 121]. When tensile force is applied, the entanglement junctions which act as physical crosslinking points of polymeric chains can be released, causing discontinuity of the structure. Secondly, high intermolecular cohesion with a high packing density of crystal phase can retard the molecular segmental relaxation toward an isotropic and disordered state. Also, they can alleviate relative slippage among stretched segments and thus be helpful to increase molecular orientation. On the other hand, the low cohesive energy density of the amorphous phase may explain the small sensitivity to change and difficulty of chain alignment. From these results, it can be seen that the increase of the orientation in overall spectrum as a function of DR (Figures 3.18a and 3.18d) as well as the increase of tensile modulus with the amount of CNC (Figure 4.4b) is due to the effect of CNC, not the alignment of PEI chains.

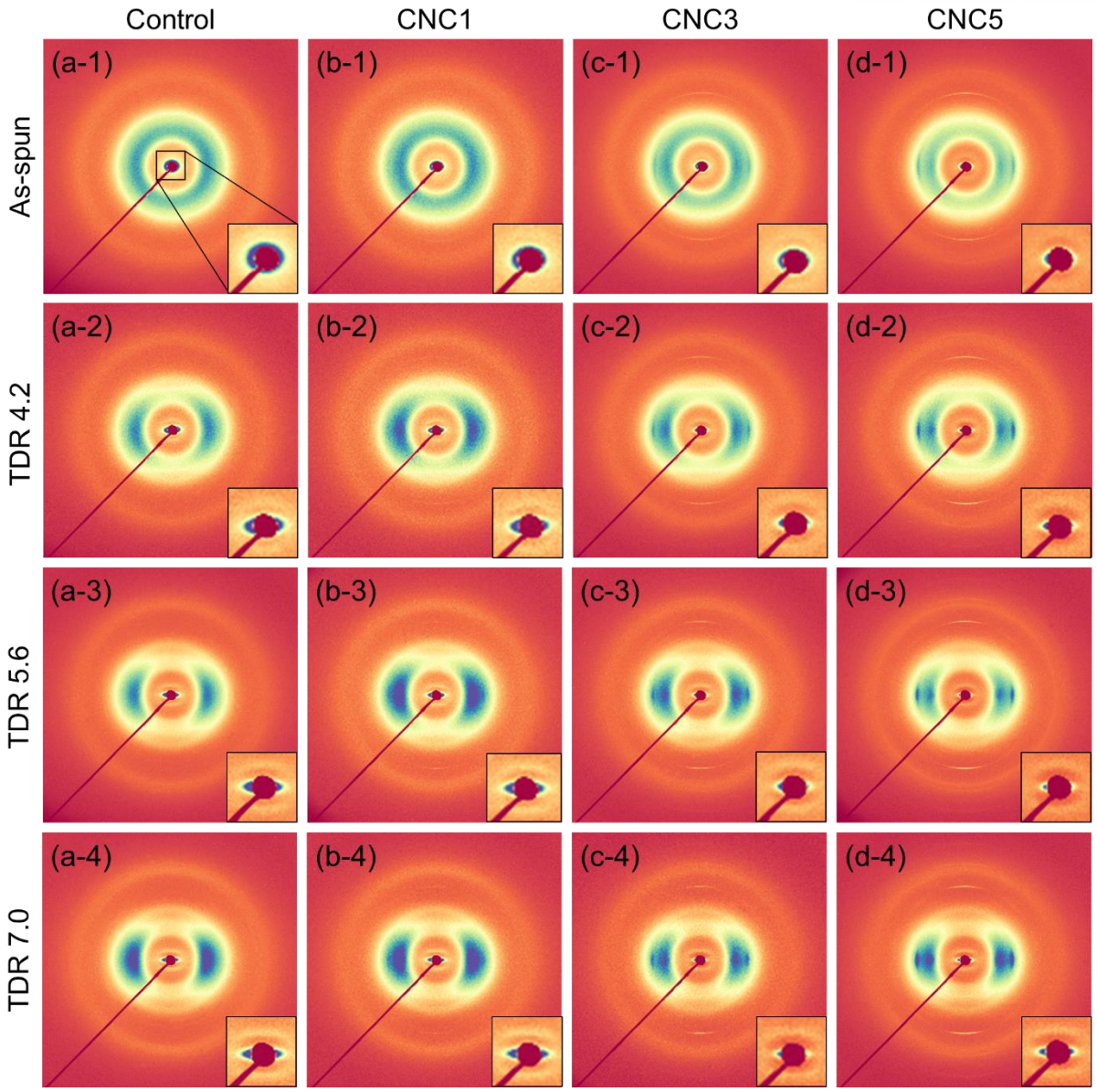


Figure 4.9 2D WAXD pattern images of (a) control PEI, (b) CNC1, (c) CNC3 and (d) CNC5 fibers. Images are arranged in order with TDR of 2.8 (as-spun), 4.2, 5.6 and 7.0 from top to bottom. The inset images indicate the magnification of SAXS range in the pattern images.

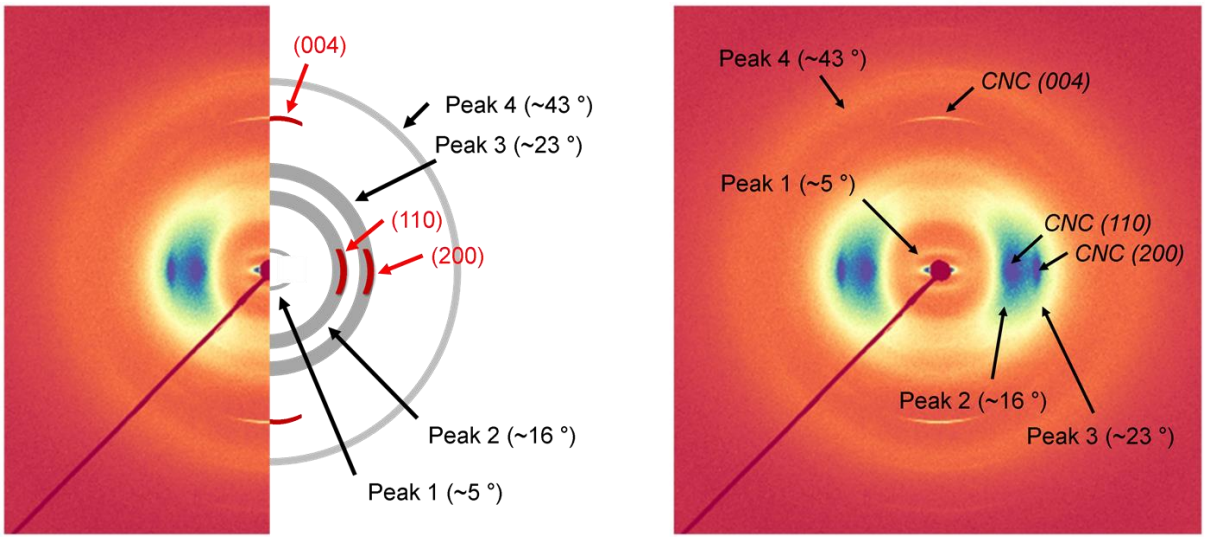


Figure 4.10 Peak assignments shown in the 2D WAXD pattern images. The assignments with black color indicate the broad peaks from the amorphous PEI polymer and red color indicate the crystal planes of CNC.

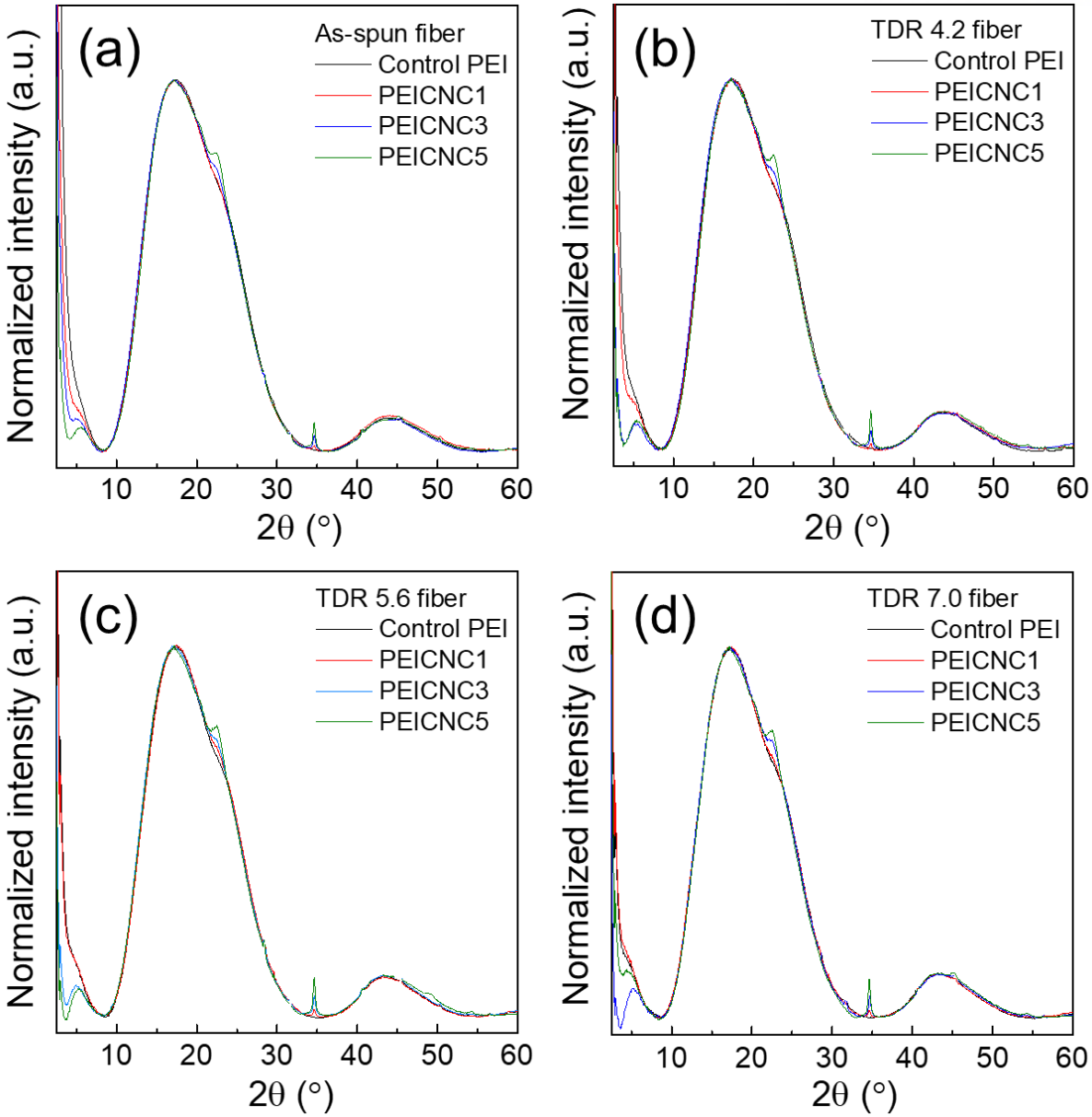


Figure 4.11 The 2D WAXD integrated scans of the PEI and PEI/CNC fibers at various TDRs of (a) 2.8 (as-spun), (b) 4.2, (c) 5.6 and (d) 7.0.

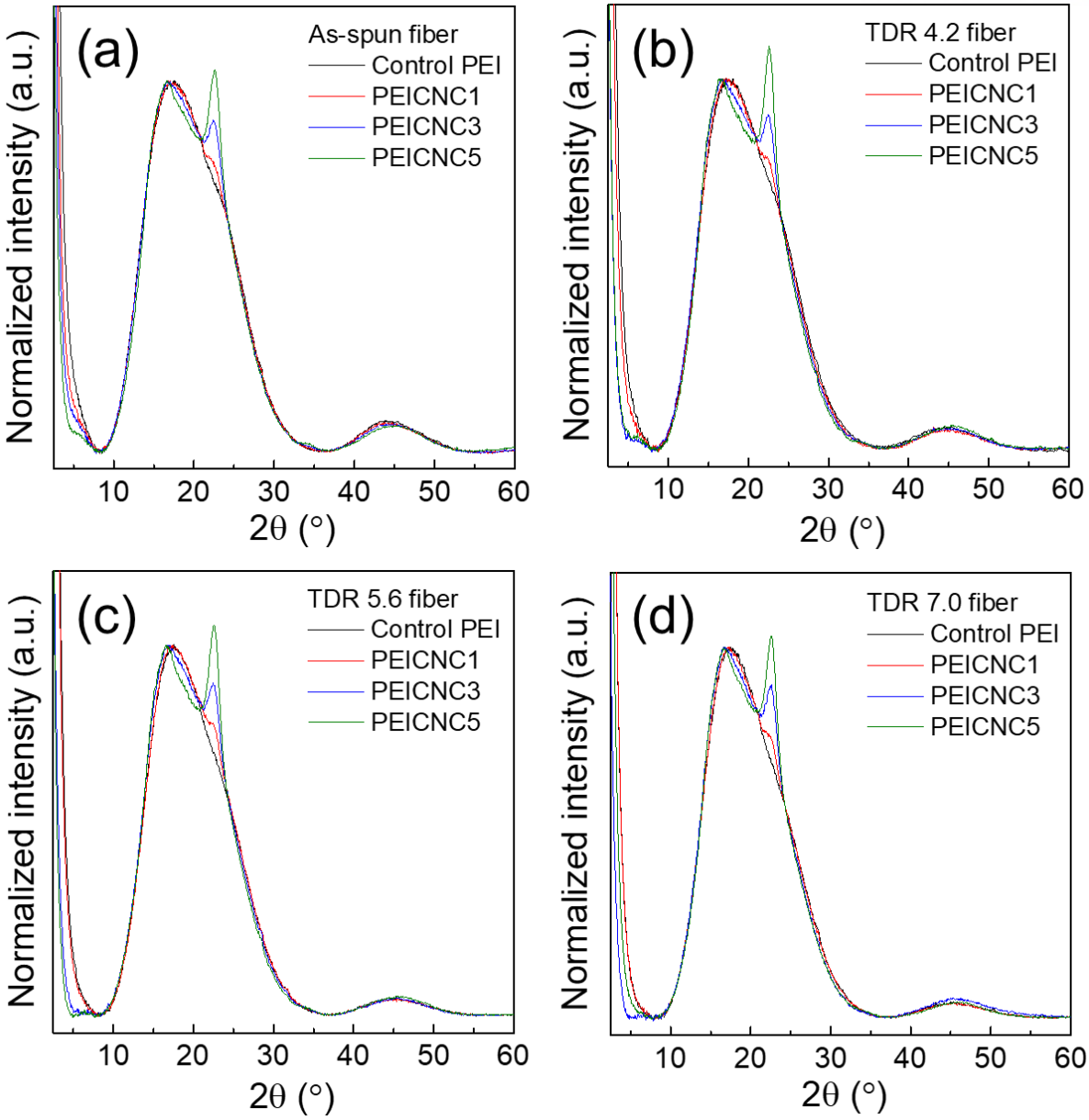


Figure 4.12 The 2D WAXD equatorial scans of the PEI and PEI/CNC fibers at various TDRs of (a) 2.8 (as-spun), (b) 4.2, (c) 5.6 and (d) 7.0.

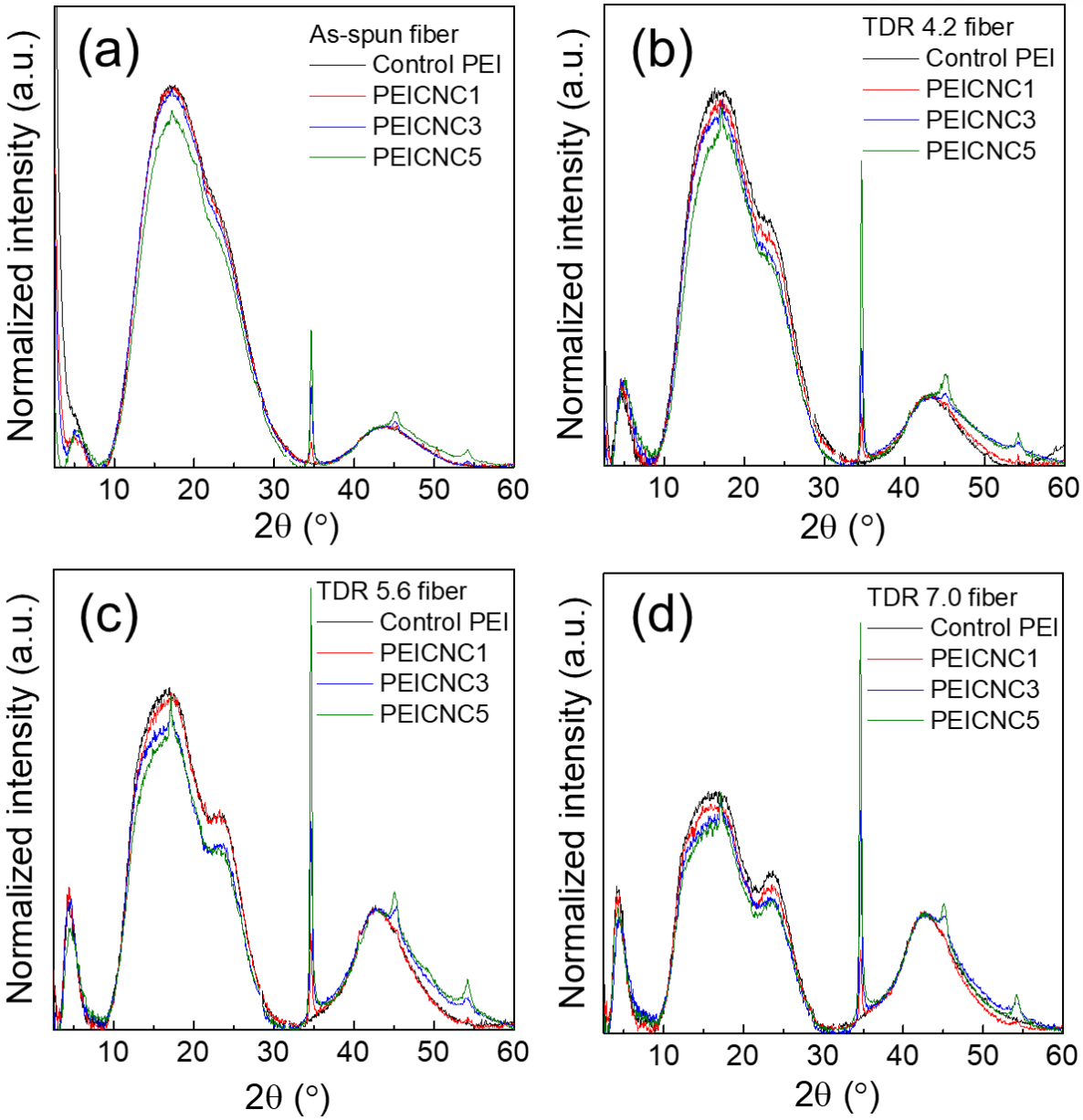


Figure 4.13 The 2D WAXD meridional scans of the PEI and PEI/CNC fibers at various TDRs of (a) 2.8 (as-spun), (b) 4.2, (c) 5.6 and (d) 7.0.

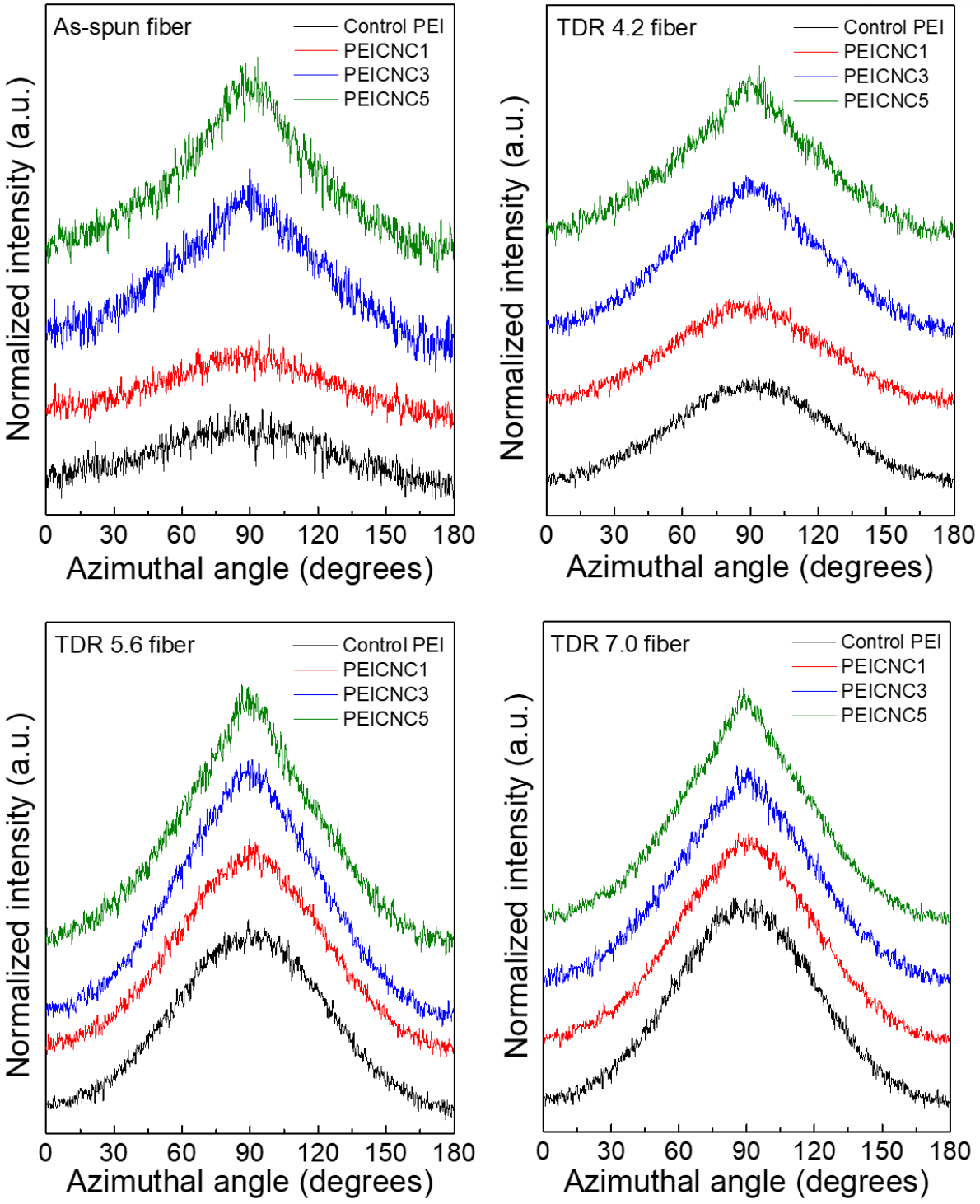


Figure 4.14 The 2D WAXD azimuthal scans of peak 2 of PEI and CNC(110) planes in PEI-based fibers at various TDR.

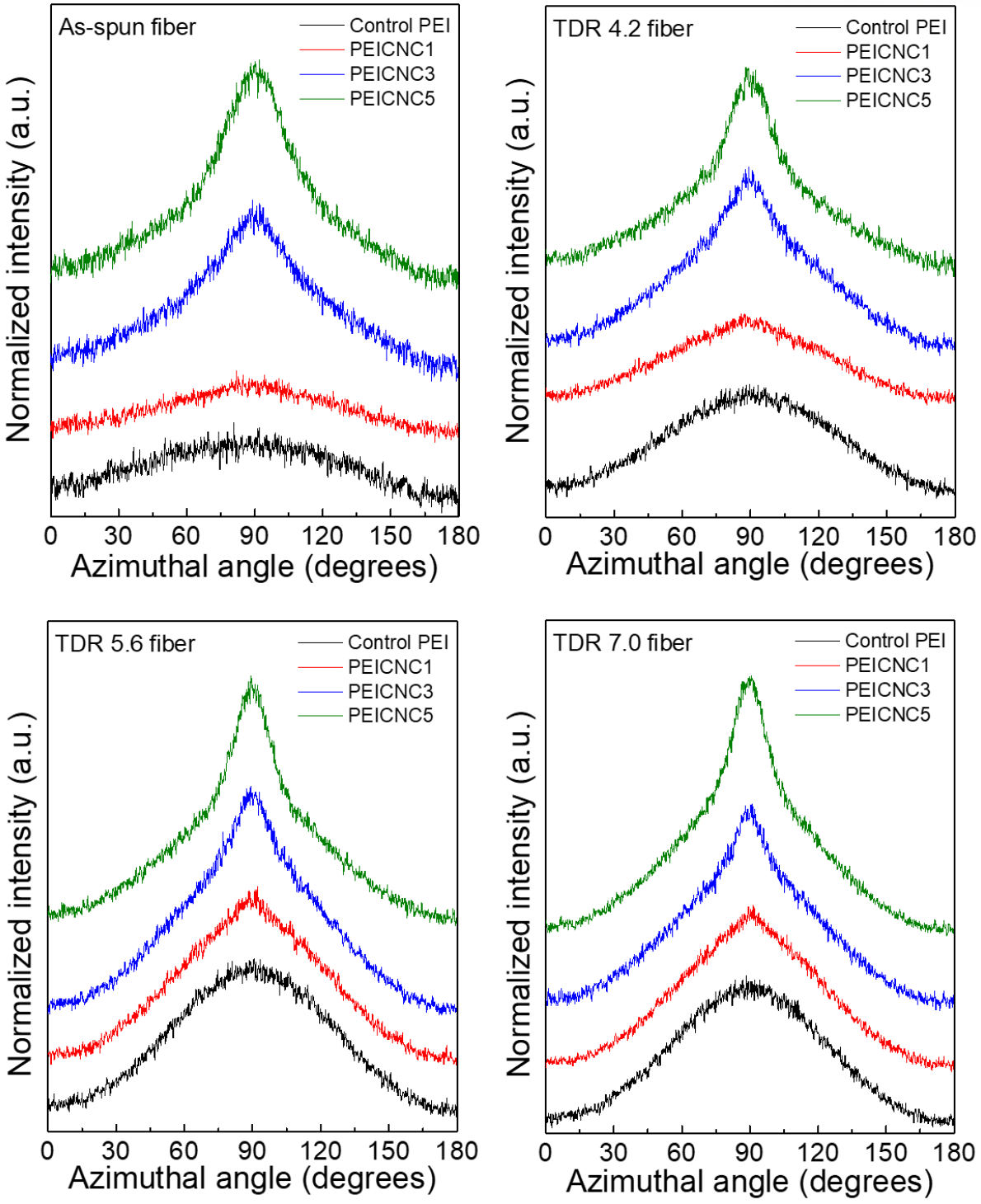


Figure 4.15 The 2D WAXD azimuthal scans of peak 3 of PEI and CNC(200) planes in PEI-based fibers at various TDR.

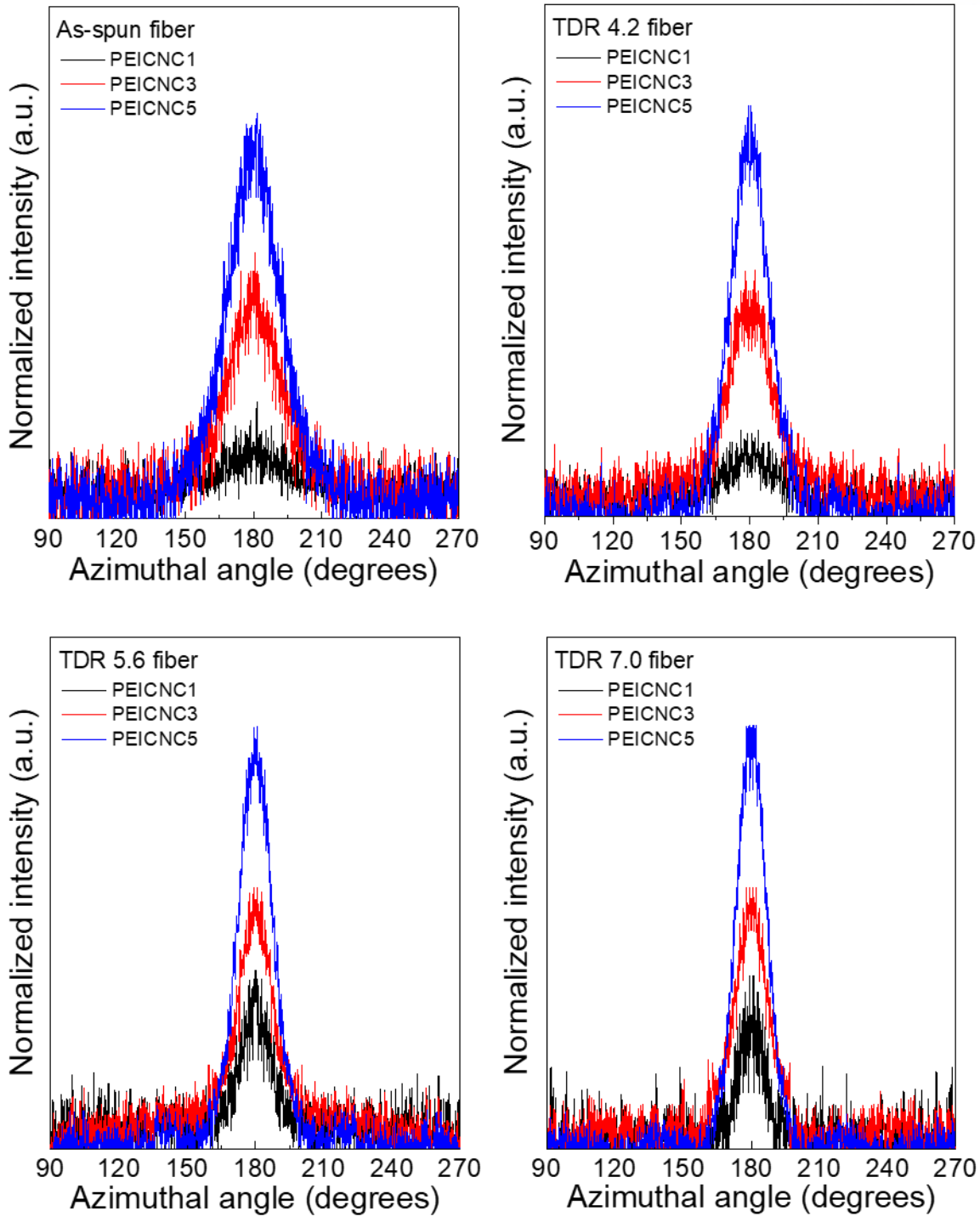


Figure 4.16 The 2D WAXD azimuthal scans of CNC(004) planes of PEI-based fibers at various TDR.

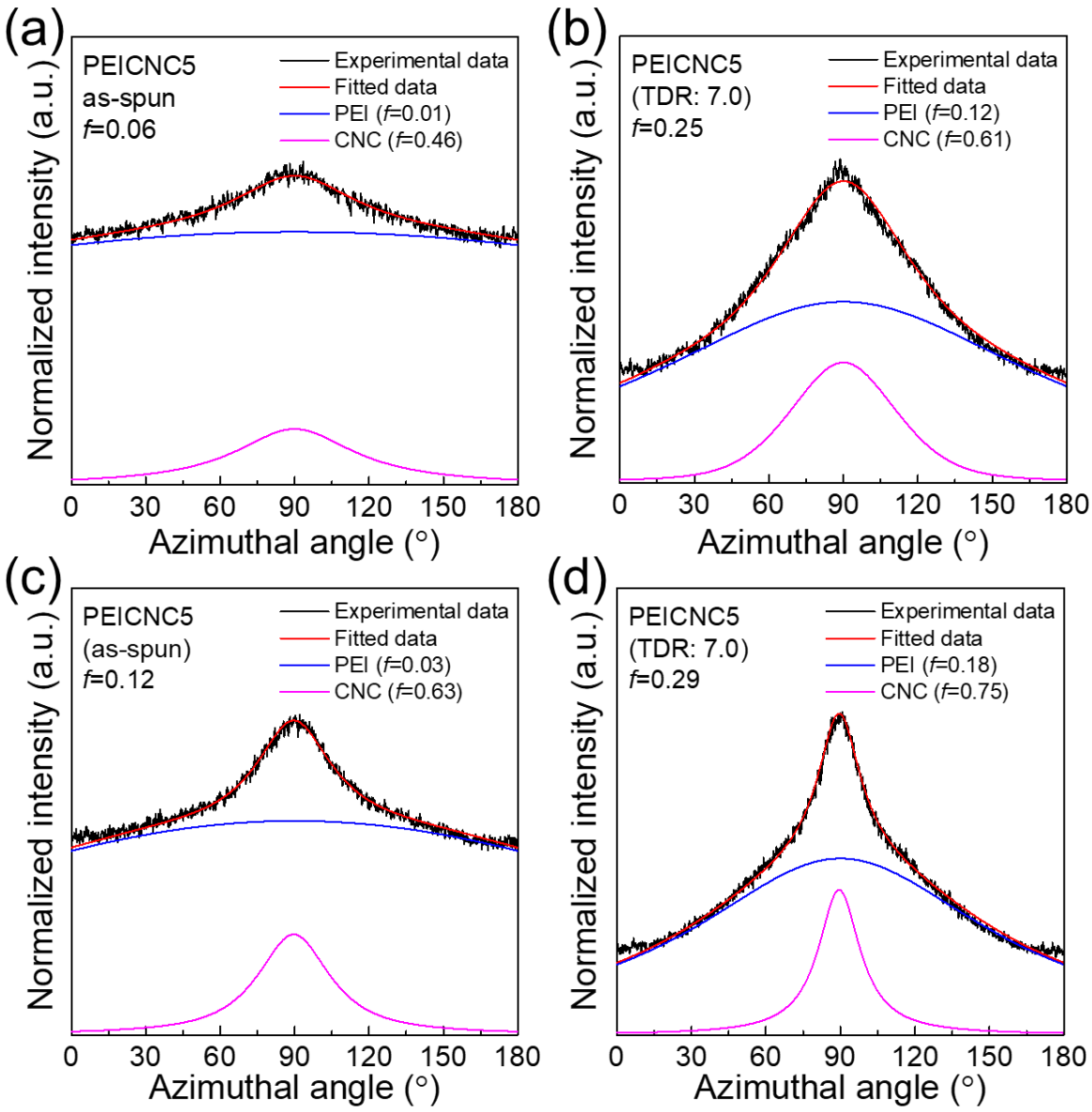


Figure 4.17 The deconvoluted 2D WAXD azimuthal scans from (a, b) peak 2 of PEI and CNC(110) and (c, d) peak 3 of PEI and CNC(200) of CNC5 fibers. The calculated Hermann's orientation factor of total spectrum and each deconvoluted spectrum were exhibited in the legend of figure.

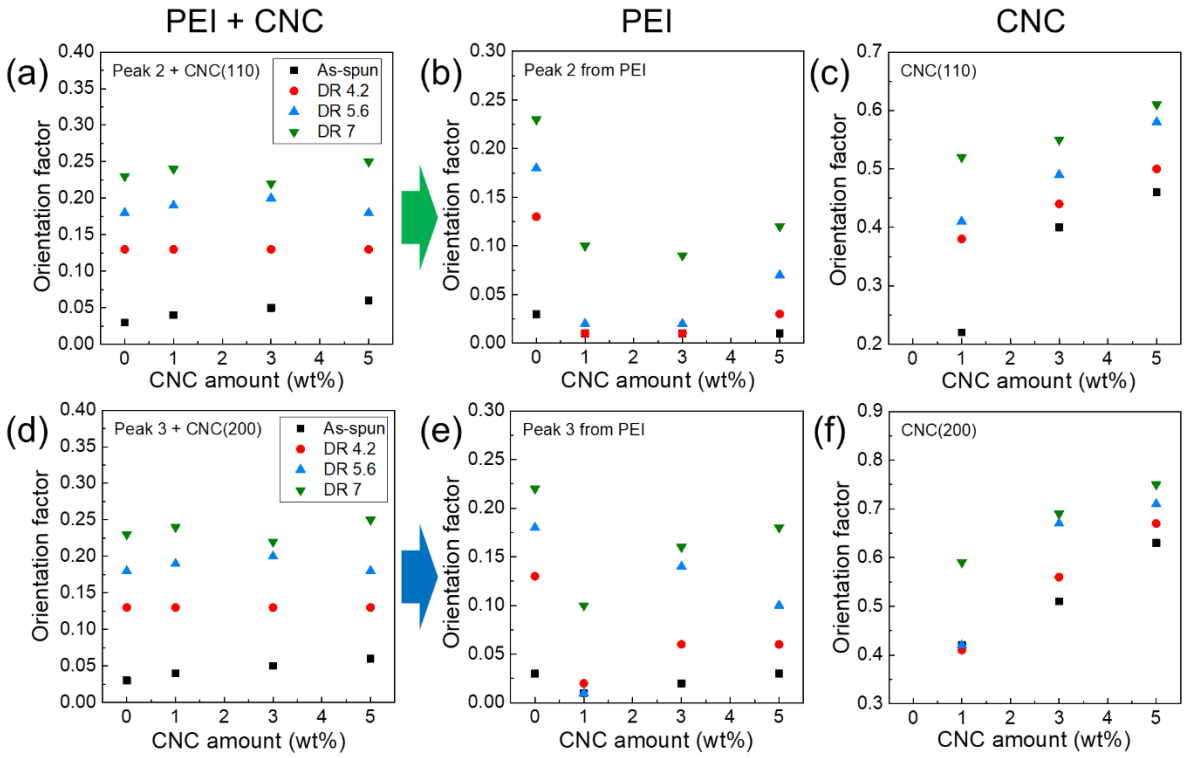


Figure 4.18 The change of Hermann's orientation factor from the (a, d) overall azimuthal spectrum, and the deconvoluted (b, e) PEI and (c, f) CNC spectra. The orientation factors in the upper row are calculated from the azimuthal scans of (a-c) peak 2 and CNC(110), and the bottom row are from (d-f) peak 3 and CNC(200).

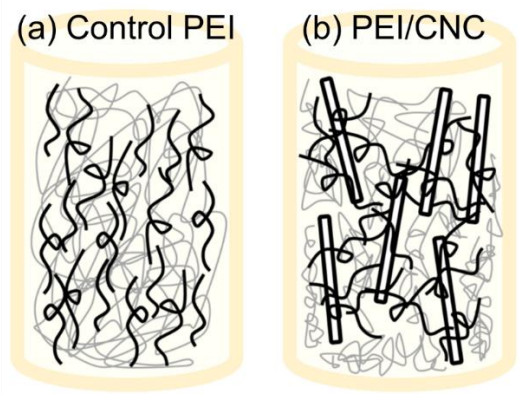


Figure 4.19 The schematic descriptions of chain alignment for the (a) control PEI and (b) PEI/CNC nanocomposite fibers.

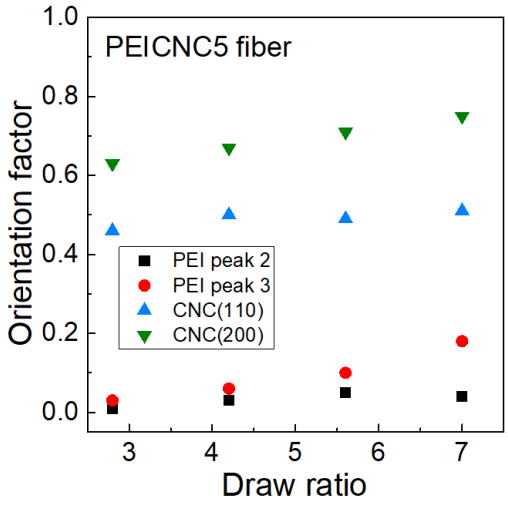


Figure 4.20 The change of Hermann's orientation factors of the various deconvoluted PEI and CNC peaks shown in the equatorial direction in the 2D pattern image depending on the TDR.

Table 4.5 The calculated Hermann's orientation factors of the PEI and PEI/CNC fibers from 2D WAXD azimuthal scans at various DR.

| | **Control** | | **CNC1** | | | **CNC3** | | | **CNC5** | | |
|---|---|---|---|---|---|---|---|---|---|---|---|
| | Peak 2 | Peak 3 | Peak 2 + CNC (110) | Peak 3 + CNC (200) | CNC (004) | Peak 2 + CNC (110) | Peak 3 + CNC (200) | CNC (004) | Peak 2 + CNC (110) | Peak 3 + CNC (200) | CNC (004) |
| **DR 2.8*** | 0.03 | 0.03 | 0.04 | 0.05 | 0.10 | 0.05 | 0.09 | 0.55 | 0.06 | 0.12 | 0.67 |
| **DR 4.2** | 0.13 | 0.13 | 0.13 | 0.14 | 0.20 | 0.13 | 0.17 | 0.60 | 0.13 | 0.19 | 0.76 |
| **DR 5.6** | 0.18 | 0.18 | 0.19 | 0.20 | 0.65 | 0.20 | 0.23 | 0.68 | 0.18 | 0.23 | 0.78 |
| **DR 7.0** | 0.23 | 0.22 | 0.24 | 0.24 | 0.67 | 0.24 | 0.24 | 0.75 | 0.25 | 0.29 | 0.86 |

* As-spun

Table 4.6 The calculated Hermann's orientation factors of the peaks shown in the equatorial direction of PEI and PEI/CNC fibers from 2D WAXD azimuthal scans at various DR.

| | **Peak 2 + CNC (110)** | | | | | | |
|---|---|---|---|---|---|---|---|
| | **Control** | **CNC1** | | **CNC3** | | **CNC5** | |
| | PEI | PEI | CNC | PEI | CNC | PEI | CNC |
| **DR 2.8 (as-spun)** | 0.03 | 0.01 | 0.22 | 0.01 | 0.40 | 0.01 | 0.46 |
| **DR 4.2** | 0.13 | 0.01 | 0.38 | 0.01 | 0.44 | 0.03 | 0.50 |
| **DR 5.6** | 0.18 | 0.02 | 0.41 | 0.02 | 0.49 | 0.07 | 0.58 |
| **DR 7.0** | 0.23 | 0.10 | 0.52 | 0.09 | 0.55 | 0.12 | 0.61 |
| | **Peak 3 + CNC (200)** | | | | | | |
| | **Control** | **CNC1** | | **CNC3** | | **CNC5** | |
| | PEI | PEI | CNC | PEI | CNC | PEI | CNC |
| **DR 2.8 (as-spun)** | 0.03 | 0.01 | 0.42 | 0.02 | 0.51 | 0.03 | 0.63 |
| **DR 4.2** | 0.13 | 0.02 | 0.41 | 0.06 | 0.56 | 0.06 | 0.67 |
| **DR 5.6** | 0.18 | 0.01 | 0.42 | 0.14 | 0.67 | 0.10 | 0.71 |
| **DR 7.0** | 0.22 | 0.10 | 0.59 | 0.16 | 0.69 | 0.18 | 0.75 |

## 4.4 Conclusion

Control PEI and PEI/CNC nanocomposite fibers with the highest mechanical properties reported so far were fabricated by dry-jet wet spinning and post-drawing. Also, the behavior of their mechanical properties and the structural changes of the fibers were observed with respect to the DR and the amount of CNC. Both the tensile strength and modulus were increased upon drawing, while the strength decreased, and the modulus increased with increasing CNC amounts. Notably, the increase of tensile modulus was not due to the alignment of PEI chains but to the alignment of CNC and the high specific modulus of CNC itself, since CNC disturbs the chain orientation along the fiber axis. Further, CNC, which is a crystalline material, already showed a high degree of orientation in the as-spun fibers, and it developed rapidly with drawing. In comparison, the amorphous PEI chains showed much lower orientation factor even after drawing to a maximum extent, which is attributed to chain entanglements and low cohesive energy density. This study provides an understanding of the effects of CNC on PEI polymeric chains and can be applied to other systems consisting of amorphous polymers and crystalline nanofillers, based on their structural differences.

## References

1. George, J.; Sabapathi, S. N., Cellulose nanocrystals: synthesis, functional properties, and applications. *Nanotechnology, science and applications* **2015,** *8*, 45-54.

2. Habibi, Y.; Lucia, L. A.; Rojas, O. J., Cellulose Nanocrystals: Chemistry, Self-Assembly, and Applications. *Chem. Rev.* **2010,** *110* (6), 3479-3500.

3. Moon, R. J.; Martini, A.; Nairn, J.; Simonsen, J.; Youngblood, J., Cellulose nanomaterials review: structure, properties and nanocomposites. *Chem. Soc. Rev.* **2011,** *40* (7), 3941-3994.

4. Mariano, M.; El Kissi, N.; Dufresne, A., Cellulose Nanocrystals and Related Nanocomposites: Review of some Properties and Challenges. *J Polym Sci Pol Phys* **2014,** *52* (12), 791-806.

5. Dufresne, A., Processing of Polymer Nanocomposites Reinforced with Polysaccharide Nanocrystals. *Molecules* **2010,** *15* (6), 4111-4128.

6. Lu, P.; Hsieh, Y. L., Preparation and properties of cellulose nanocrystals: Rods, spheres, and network. *Carbohydr. Polym.* **2010,** *82* (2), 329-336.

7. Sebe, G.; Ham-Pichavant, F.; Ibarboure, E.; Koffi, A. L. C.; Tingaut, P., Supramolecular Structure Characterization of Cellulose II Nanowhiskers Produced by Acid Hydrolysis of Cellulose I Substrates. *Biomacromolecules* **2012,** *13* (2), 570-578.

8. Chang, H. B.; Chien, A. T.; Liu, H. C.; Wang, P. H.; Newcomb, B. A.; Kumar, S., Gel Spinning of Polyacrylonitrile/Cellulose Nanocrystal Composite Fibers. *Acs Biomaterials Science & Engineering* **2015,** *1* (7), 610-616.

9. Chen, S.; Schueneman, G.; Pipes, R. B.; Youngblood, J.; Moon, R. J., Effects of Crystal Orientation on Cellulose Nanocrystals-Cellulose Acetate Nanocomposite Fibers Prepared by Dry Spinning. *Biomacromolecules* **2014,** *15* (10), 3827-3835.

10. Liu, D. G.; Li, J. L.; Sun, F. X.; Xiao, R. M.; Guo, Y.; Song, J. W., Liquid crystal microphase separation of cellulose nanocrystals in wet-spun PVA composite fibers. *Rsc Adv* **2014,** *4* (58), 30784-30789.

11. Rojas, O. J.; Montero, G. A.; Habibi, Y., Electrospun Nanocomposites from Polystyrene Loaded with Cellulose Nanowhiskers. *J. Appl. Polym. Sci.* **2009,** *113* (2), 927-935.

12. Uddin, A. J.; Araki, J.; Gotoh, Y., Toward "Strong" Green Nanocomposites: Polyvinyl Alcohol Reinforced with Extremely Oriented Cellulose Whiskers. *Biomacromolecules* **2011,** *12* (3), 617-624.

13. Urena-Benavides, E. E.; Kitchens, C. L., Wide-Angle X-ray Diffraction of Cellulose Nanocrystal-Alginate Nanocomposite Fibers. *Macromolecules* **2011,** *44* (9), 3478-3484.

14. Wanasekara, N. D.; Santos, R. P. O.; Douch, C.; Frollini, E.; Eichhorn, S. J., Orientation of cellulose nanocrystals in electrospun polymer fibres. *J Mater Sci* **2016,** *51* (1), 218-227.

15. Grunert, M.; Winter, W. T., Nanocomposites of cellulose acetate butyrate reinforced with cellulose nanocrystals. *J. Polym. Environ.* **2002,** *10* (1-2), 27-30.

16. Eom, Y.; Son, S. M.; Kim, Y. E.; Lee, J.-E.; Hwang, S.-H.; Chae, H. G., Structure evolution mechanism of highly ordered graphite during carbonization of cellulose nanocrystals. *Carbon* **2019,** *150*, 142-152.

17. Zhu, H. L.; Shen, F.; Luo, W.; Zhu, S. Z.; Zhao, M. H.; Natarajan, B.; Dai, J. Q.; Zhou, L. H.; Ji, X. L.; Yassar, R. S.; Li, T.; Hu, L. B., Low temperature carbonization of cellulose nanocrystals for high performance carbon anode of sodium-ion batteries. *Nano Energy* **2017,** *33*, 37-44.

18. Souza, D. R. D.; de Mesquita, J. P.; Lago, R. M.; Caminhas, L. D.; Pereira, F. V., Cellulose nanocrystals: A versatile precursor for the preparation of different carbon structures and luminescent carbon dots. *Ind Crop Prod* **2016,** *93*, 121-128.

19. Cho, S. Y.; Yun, Y. S.; Jin, H. J., Carbon nanofibers prepared by the carbonization of self-assembled cellulose nanocrystals. *Macromol Res* **2014,** *22* (7), 753-756.

20. Kim, H.; Hong, J.; Yoon, G.; Kim, H.; Park, K. Y.; Park, M. S.; Yoon, W. S.; Kang, K., Sodium intercalation chemistry in graphite. *Energ Environ Sci* **2015,** *8* (10), 2963-2969.

21. Moriwake, H.; Kuwabara, A.; Fisher, C. A. J.; Ikuhara, Y., Why is sodium-intercalated graphite unstable? *Rsc Adv* **2017,** *7* (58), 36550-36554.

22. Stevens, D. A.; Dahn, J. R., The mechanisms of lithium and sodium insertion in carbon materials. *J. Electrochem. Soc.* **2001,** *148* (8), A803-A811.

23. Choi, S. H.; Nam, G.; Chae, S.; Kim, D.; Kim, N.; Kim, W. S.; Ma, J.; Sung, J.; Han, S. M.; Ko, M.; Lee, H. W.; Cho, J., Robust Pitch on Silicon Nanolayer-Embedded Graphite for Suppressing Undesirable Volume Expansion. *Adv Energy Mater* **2019,** *9* (4).

24. Kim, H.; Hong, J.; Park, Y. U.; Kim, J.; Hwang, I.; Kang, K., Sodium Storage Behavior in Natural Graphite using Ether-based Electrolyte Systems. *Adv. Funct. Mater.* **2015,** *25* (4), 534-541.

25. Ko, M.; Chae, S.; Ma, J.; Kim, N.; Lee, H. W.; Cui, Y.; Cho, J., Scalable synthesis of silicon-nanolayer-embedded graphite for high-energy lithium-ion batteries. *Nature Energy* **2016,** *1*.

26. Wen, Y.; He, K.; Zhu, Y. J.; Han, F. D.; Xu, Y. H.; Matsuda, I.; Ishii, Y.; Cumings, J.; Wang, C. S., Expanded graphite as superior anode for sodium-ion batteries. *Nature Communications* **2014,** *5*.

27. Bommier, C.; Surta, T. W.; Dolgos, M.; Ji, X. L., New Mechanistic Insights on Na-Ion Storage in Nongraphitizable Carbon. *Nano Lett.* **2015,** *15* (9), 5888-5892.

28. Saurel, D.; Orayech, B.; Xiao, B. W.; Carriazo, D.; Li, X. L.; Rojo, T., From Charge Storage Mechanism to Performance: A Roadmap toward High Specific Energy Sodium-Ion Batteries through Carbon Anode Optimization. *Adv Energy Mater* **2018,** *8* (17).

29. Sun, J.; Lee, H. W.; Pasta, M.; Yuan, H. T.; Zheng, G. Y.; Sun, Y. M.; Li, Y. Z.; Cui, Y.,

A phosphorene-graphene hybrid material as a high-capacity anode for sodium-ion batteries. *Nature Nanotechnology* **2015,** *10* (11), 980-U184.

30. Datta, D.; Li, J. W.; Shenoy, V. B., Defective Graphene as a High-Capacity Anode Material for Na- and Ca-Ion Batteries. *Acs Appl Mater Inter* **2014,** *6* (3), 1788-1795.

31. Shen, F.; Zhu, H. L.; Luo, W.; Wan, J. Y.; Zhou, L. H.; Dai, J. Q.; Zhao, B.; Han, X. G.; Fu, K.; Hu, L. B., Chemically Crushed Wood Cellulose Fiber towards High-Performance Sodium-Ion Batteries. *Acs Appl Mater Inter* **2015,** *7* (41), 23291-23296.

32. Simone, V.; Boulineau, A.; de Geyer, A.; Rouchon, D.; Simonin, L.; Martinet, S., Hard carbon derived from cellulose as anode for sodium ion batteries: Dependence of electrochemical properties on structure. *Journal of Energy Chemistry* **2016,** *25* (5), 761-768.

33. Li, Y. M.; Xu, S. Y.; Wu, X. Y.; Yu, J. Z.; Wang, Y. S.; Hu, Y. S.; Li, H.; Chen, L. Q.; Huang, X. J., Amorphous monodispersed hard carbon micro-spherules derived from biomass as a high performance negative electrode material for sodium-ion batteries. *J Mater Chem A* **2015,** *3* (1), 71-77.

34. Xiao, L. F.; Lu, H. Y.; Fang, Y. J.; Sushko, M. L.; Cao, Y. L.; Ai, X. P.; Yang, H. X.; Liu, J., Low-Defect and Low-Porosity Hard Carbon with High Coulombic Efficiency and High Capacity for Practical Sodium Ion Battery Anode. *Adv Energy Mater* **2018,** *8* (20).

35. Luo, W.; Bommier, C.; Jian, Z. L.; Li, X.; Carter, R.; Vail, S.; Lu, Y. H.; Lee, J. J.; Ji, X. L., Low-Surface-Area Hard Carbon Anode for Na-Ion Batteries via Graphene Oxide as a Dehydration Agent. *Acs Appl Mater Inter* **2015,** *7* (4), 2626-2631.

36. Abdallah, W.; Kamal, M. R., Influence of process variables on physical characteristics of spray freeze dried cellulose nanocrystals. *Cellulose* **2018,** *25* (10), 5711-5730.

37. Peng, Y. C.; Gardner, D. J.; Han, Y. S., Drying cellulose nanofibrils: in search of a suitable method. *Cellulose* **2012,** *19* (1), 91-102.

38. Brunner, P. H.; Roberts, P. V., The Significance of Heating Rate on Char Yield and Char Properties in the Pyrolysis of Cellulose. *Carbon* **1980,** *18* (3), 217-224.

39. Fu, Y. H.; Zhang, N. Y.; Shen, Y. F.; Ge, X. L.; Chen, M. D., Micro-mesoporous carbons from original and pelletized rice husk via one-step catalytic pyrolysis. *Bioresour. Technol.* **2018,** *269*, 67-73.

40. Burket, C. L.; Rajagopalan, R.; Foley, H. C., Overcoming the barrier to graphitization in a polymer-derived nanoporous carbon. *Carbon* **2008,** *46* (3), 501-510.

41. Cho, B. G.; Lee, S.; Hwang, S. H.; Han, J. H.; Chae, H. G.; Park, Y. B., Influence of hybrid graphene oxide-carbon nanotube as a nano-filler on the interfacial interaction in nylon composites prepared by in situ interfacial polymerization. *Carbon* **2018,** *140*, 324-337.

42. Honda, H.; Kobayashi, K.; Sugawara, S., X-Ray Characteristics of Non-Graphitizing-Type Carbon. *Carbon* **1968,** *6* (4), 517-+.

43. Ōya, A.; Marsh, H., Phenomena of catalytic graphitization. *J Mater Sci* **1982,** *17* (2), 309-322.

44. Cao, Y. L.; Xiao, L. F.; Sushko, M. L.; Wang, W.; Schwenzer, B.; Xiao, J.; Nie, Z. M.; Saraf, L. V.; Yang, Z. G.; Liu, J., Sodium Ion Insertion in Hollow Carbon Nanowires for Battery Applications. *Nano Lett.* **2012,** *12* (7), 3783-3787.

45. Chae, H. G.; Minus, M. L.; Rasheed, A.; Kumar, S., Stabilization and carbonization of gel spun polyacrylonitrile/single wall carbon nanotube composite fibers. *Polymer* **2007,** *48* (13), 3781-3789.

46. Sadezky, A.; Muckenhuber, H.; Grothe, H.; Niessner, R.; Poschl, U., Raman micro spectroscopy of soot and related carbonaceous materials: Spectral analysis and structural information. *Carbon* **2005,** *43* (8), 1731-1742.

47. Hong, K. L.; Qie, L.; Zeng, R.; Yi, Z. Q.; Zhang, W.; Wang, D.; Yin, W.; Wu, C.; Fan, Q. J.; Zhang, W. X.; Huang, Y. H., Biomass derived hard carbon used as a high performance anode material for sodium ion batteries. *J Mater Chem A* **2014,** *2* (32), 12733-12738.

48. Kim, K.; Lim, D. G.; Han, C. W.; Osswald, S.; Ortalan, V.; Youngblood, J. P.; Pol, V. G., Tailored Carbon Anodes Derived from Biomass for Sodium-Ion Storagel. *Acs Sustainable Chemistry & Engineering* **2017,** *5* (10), 8720-8728.

49. Qiu, S.; Xiao, L. F.; Sushko, M. L.; Han, K. S.; Shao, Y. Y.; Yan, M. Y.; Liang, X. M.; Mai, L. Q.; Feng, J. W.; Cao, Y. L.; Ai, X. P.; Yang, H. X.; Liu, J., Manipulating Adsorption-Insertion Mechanisms in Nanostructured Carbon Materials for High-Efficiency Sodium Ion Storage. *Adv Energy Mater* **2017,** *7* (17).

50. Stevens, D. A.; Dahn, J. R., High capacity anode materials for rechargeable sodium-ion batteries. *J. Electrochem. Soc.* **2000,** *147* (4), 1271-1273.

51. Ota, H.; Sakata, Y.; Inoue, A.; Yamaguchi, S., Analysis of vinylene carbonate derived SEI layers on graphite anode. *J. Electrochem. Soc.* **2004,** *151* (10), A1659-A1669.

52. Prabakar, S. J. R.; Jeong, J.; Pyo, M., Nanoporous hard carbon anodes for improved electrochemical performance in sodium ion batteries. *Electrochim. Acta* **2015,** *161*, 23-31.

53. Li, H. B.; Shen, F.; Luo, W.; Dai, J. Q.; Han, X. G.; Chen, Y. N.; Yao, Y. G.; Zhu, H. L.; Fu, K.; Hitz, E.; Hu, L. B., Carbonized-leaf Membrane with Anisotropic Surfaces for Sodium-ion Battery. *Acs Appl Mater Inter* **2016,** *8* (3), 2204-2210.

54. Simon, P.; Gogotsi, Y.; Dunn, B., Where Do Batteries End and Supercapacitors Begin? *Science* **2014,** *343* (6176), 1210-1211.

55. Hardwick, L. J.; Ruch, P. W.; Hahn, M.; Scheifele, W.; Kotz, R.; Novak, P., In situ Raman spectroscopy of insertion electrodes for lithium-ion batteries and supercapacitors: First cycle effects. *J. Phys. Chem. Solids* **2008,** *69* (5-6), 1232-1237.

56. Huang, S. F.; Li, Z. P.; Wang, B.; Zhang, J. J.; Peng, Z. Q.; Qi, R. J.; Wang, J.; Zhao, Y. F., N-Doping and Defective Nanographitic Domain Coupled Hard Carbon Nanoshells for High Performance Lithium/Sodium Storage. *Adv. Funct. Mater.* **2018,** *28* (10).

57. Kim, D. Y.; Nishiyama, Y.; Wada, M.; Kuga, S., Graphitization of highly crystalline cellulose. *Carbon* **2001,** *39* (7), 1051-1056.

58. Liu, Z. L.; Peng, W. X.; Zare, Y.; Hui, D.; Rhee, K. Y., Predicting the electrical conductivity in polymer carbon nanotube nanocomposites based on the volume fractions and resistances of the nanoparticle, interphase, and tunneling regions in conductive networks. *Rsc Adv* **2018,** *8* (34), 19001-19010.

59. Zare, Y.; Rhee, K. Y., Development and modification of conventional Ouali model for tensile modulus of polymer/carbon nanotubes nanocomposites assuming the roles of dispersed and networked nanoparticles and surrounding interphases. *J. Colloid Interface Sci.* **2017,** *506*, 283-290.

60. Burket, C. L.; Rajagopalan, R.; Foley, H. C., Synthesis of nanoporous carbon with pre-graphitic domains. *Carbon* **2007,** *45* (11), 2307-2310.

61. Oya, A.; Marsh, H., Phenomena of Catalytic Graphitization. *J Mater Sci* **1982,** *17* (2), 309-322.

62. Collard, F. X.; Blin, J., A review on pyrolysis of biomass constituents: Mechanisms and composition of the products obtained from the conversion of cellulose, hemicelluloses and lignin. *Renew Sust Energ Rev* **2014,** *38*, 594-608.

63. Dumanli, A. G.; Windle, A. H., Carbon fibres from cellulosic precursors: a review. *J Mater Sci* **2012,** *47* (10), 4236-4250.

64. Yoo, E.; Kim, J.; Hosono, E.; Zhou, H.; Kudo, T.; Honma, I., Large reversible Li storage of graphene nanosheet families for use in rechargeable lithium ion batteries. *Nano Lett.* **2008,** *8* (8), 2277-2282.

65. Zhou, X. S.; Yin, Y. X.; Wan, L. J.; Guo, Y. G., Facile synthesis of silicon nanoparticles inserted into graphene sheets as improved anode materials for lithium-ion batteries. *Chem. Commun.* **2012,** *48* (16), 2198-2200.

66. Osswald, S.; Havel, M.; Gogotsi, Y., Monitoring oxidation of multiwalled carbon nanotubes by Raman spectroscopy. *Journal of Raman Spectroscopy* **2007,** *38* (6), 728-736.

67. Wang, H. T.; Wang, Y.; Li, T.; Wu, S.; Xu, L. H., Gradient distribution of radial structure of PAN-based carbon fiber treated by high temperature. *Prog Nat Sci-Mater* **2014,** *24* (1), 31-34.

68. Ferrari, A. C.; Robertson, J., Resonant Raman spectroscopy of disordered, amorphous, and diamondlike carbon. *Phys Rev B* **2001,** *64* (7).

69. Harris, P. J. F., Structure of non-graphitising carbons. *Int. Mater. Rev.* **1997,** *42* (5), 206-218.

70. Johnson, R. O.; Burlhis, H. S., Polyetherimide - a New High-Performance Thermoplastic Resin. *Journal of Polymer Science-Polymer Symposia* **1983,** (70), 129-143.

71. Fukuhara, M., Temperature dependency of elastic moduli and internal dilational and shear frictions of polyetherimide. *J. Appl. Polym. Sci.* **2003,** *90* (3), 759-764.

72. Liu, T. X.; Tong, Y. J.; Zhang, W. D., Preparation and characterization of carbon

nanotube/polyetherimide nanocomposite films. *Compos. Sci. Technol.* **2007,** *67* (3-4), 406-412.

73. White, S. A.; Weissman, S. R.; Kambour, R. P., Resistance of a Polyetherimide to Environmental-Stress Crazing and Cracking. *J. Appl. Polym. Sci.* **1982,** *27* (7), 2675-2682.

74. Ghosh, A.; Sen, S. K.; Banerjee, S.; Voit, B., Solubility improvements in aromatic polyimides by macromolecular engineering. *Rsc Adv* **2012,** *2* (14), 5900-5926.

75. White, D. M.; Takekoshi, T.; Williams, F. J.; Relles, H. M.; Donahue, P. E.; Klopfer, H. J.; Loucks, G. R.; Manello, J. S.; Matthews, R. O.; Schluenz, R. W., Polyetherimides Via Nitro-Displacement Polymerization - Monomer Synthesis and C-13-Nmr Analysis of Monomers and Polymers. *Journal of Polymer Science Part a-Polymer Chemistry* **1981,** *19* (7), 1635-1658.

76. Jiang, F. Real-time Optical and Mechano-Optical Studies During Drying and Uniaxial Stretching of Polyetherimide Films from Solution. University of Akron, 2014.

77. Bicakci, S.; Cakmak, M., Development of structural hierarchy during uniaxial drawing of PEEK/PEI blends from amorphous precursors. *Polymer* **2002,** *43* (1), 149-157.

78. Rath, T.; Kumar, S.; Mahaling, R. N.; Khatua, B. B.; Das, C. K.; Yadaw, S. B., Mechanical, morphological and thermal properties of in situ ternary composites based on poly(ether imide), silicone rubber and liquid crystalline polymer. *Materials Science and Engineering a-Structural Materials Properties Microstructure and Processing* **2008,** *490* (1-2), 198-207.

79. Woo, E. M.; Yau, S. N., Peculiar glass transition behavior and miscibility in a binary mixture comprising amorphous poly(ether imide) with semicrystalline poly(butylene terephthalate). *Macromolecules* **1997,** *30* (12), 3626-3631.

80. Chen, Y.; Tao, J.; Ezzeddine, A.; Mahfouz, R.; Al-Shahrani, A.; Alabedi, G.; Khashab, M. N., Superior Performance Nanocomposites from Uniformly Dispersed Octadecylamine Functionalized Multi-Walled Carbon Nanotubes. *C* **2015,** *1* (1).

81. Dwivedi, M.; Dixit, A.; Alam, S.; Ghosh, A. K., Dielectric and Tensile Behavior of Nanoclay Reinforced Polyetherimide Nanocomposites. *J. Appl. Polym. Sci.* **2011,** *122* (2), 1040-1046.

82. Kumar, S.; Rath, T.; Mahaling, R. N.; Reddy, C. S.; Das, C. K.; Pandey, K. N.; Srivastava, R. B.; Yadaw, S. B., Study on mechanical, morphological and electrical properties of carbon nanofiber/polyetherimide composites. *Materials Science and Engineering B-Solid State Materials for Advanced Technology* **2007,** *141* (1-2), 61-70.

83. Pitchan, M. K.; Bhowmik, S.; Balachandran, M.; Abraham, M., Effect of surface functionalization on mechanical properties and decomposition kinetics of high performance polyetherimide/MWCNT nano composites. *Composites Part a-Applied Science and Manufacturing* **2016,** *90*, 147-160.

84. Pitchan, M. K.; Bhowmik, S.; Balachandran, M.; Abraham, M., Process optimization of functionalized MWCNT/polyetherimide nanocomposites for aerospace application. *Materials &*

*Design* **2017,** *127*, 193-203.

85. Dri, F. L.; Hector, L. G.; Moon, R. J.; Zavattieri, P. D., Anisotropy of the elastic properties of crystalline cellulose I-beta from first principles density functional theory with Van der Waals interactions. *Cellulose* **2013,** *20* (6), 2703-2718.

86. Warner, S. B.; Lee, J., Towards Understanding the Increase in Strength of Thermotropic Polyesters with Heat-Treatment. *J Polym Sci Pol Phys* **1994,** *32* (10), 1759-1769.

87. Simal, A. L.; Martin, A. R., Structure of heat-treated Nylon 6 and 6.6 fibers. I. The shrinkage mechanism. *J. Appl. Polym. Sci.* **1998,** *68* (3), 441-452.

88. He, X.; Xiao, Q.; Lu, C. H.; Wang, Y. R.; Zhang, X. F.; Zhao, J. Q.; Zhang, W.; Zhang, X. M.; Deng, Y. L., Uniaxially Aligned Electrospun All-Cellulose Nanocomposite Nanofibers Reinforced with Cellulose Nanocrystals: Scaffold for Tissue Engineering. *Biomacromolecules* **2014,** *15* (2), 618-627.

89. Hooshmand, S.; Aitomaki, Y.; Skrifvars, M.; Mathew, A. P.; Oksman, K., All-cellulose nanocomposite fibers produced by melt spinning cellulose acetate butyrate and cellulose nanocrystals. *Cellulose* **2014,** *21* (4), 2665-2678.

90. Hu, W. G.; Schmidt-Rohr, K., Polymer ultradrawability: the crucial role of alpha-relaxation chain mobility in the crystallites. *Acta Polym.* **1999,** *50* (8), 271-285.

91. Smith, P.; Lemstra, P. J., Ultrahigh-Strength Polyethylene Filaments by Solution Spinning-Drawing .2. Influence of Solvent on the Drawability. *Makromol Chem* **1979,** *180* (12), 2983-2986.

92. Smook, J.; Flinterman, M.; Pennings, A. J., Influence of Spinning-Hot Drawing Conditions on the Tensile-Strength of Porous High Molecular-Weight Polyethylene. *Polym. Bull.* **1980,** *2* (11), 775-783.

93. Bersted, B. H., Entanglement Network Model Relating Tensile Impact Strength and the Ductile-Brittle Transition to Molecular-Structure in Amorphous Polymers. *J. Appl. Polym. Sci.* **1979,** *24* (1), 37-50.

94. Linares, A.; Acosta, J. L., Tensile and dynamic mechanical behaviour of polymer blends based on PVDF. *Eur. Polym. J.* **1997,** *33* (4), 467-473.

95. Dong, X.; McDowell, D. L.; Kalidindi, S. R.; Jacob, K. I., Dependence of mechanical properties on crystal orientation of semi-crystalline polyethylene structures. *Polymer* **2014,** *55* (16), 4248-4257.

96. Xu, W. N.; Qin, Z. Y.; Yu, H. Y.; Liu, Y. N.; Liu, N.; Zhou, Z.; Chen, L., Cellulose nanocrystals as organic nanofillers for transparent polycarbonate films. *J. Nanopart. Res.* **2013,** *15* (4).

97. Chirkov, S. V.; Kechekyan, A. S.; Belov, N. A.; Antonov, S. V.; Alentiev, A. Y., The influence of uniform deformation of Ultem-1000 polyetherimide films on their mechanical and gas transport characteristics. *Petroleum Chemistry* **2016,** *56* (11), 1074-1084.

98. Xu, Z. K.; Shen, L. Q.; Yang, Q.; Liu, F.; Wang, S. Y.; Xu, Y. Y., Ultrafiltration hollow fiber membranes from poly(ether imide): preparation, morphologies and properties. *J. Membr. Sci.* **2003,** *223*

(1-2), 105-118.

99. Reddy, G. V. R.; Deopura, B. L.; Joshi, M., Dry-Jet-Wet Spun Polyurethane Fibers. I. Optimization of the Spinning Parameters. *J. Appl. Polym. Sci.* **2010,** *118* (4), 2291-2303.

100. Li, D. H.; Lu, C. X.; Wu, G. P.; Yang, Y.; An, F.; Feng, Z. H.; Li, X. T., Structural heterogeneity and its influence on the tensile fracture of PAN-based carbon fibers. *Rsc Adv* **2014,** *4* (105), 60648-60651.

101. de Nicola, A.; Correa, A.; Milano, G.; La Manna, P.; Musto, P.; Mensitieri, G.; Scherillo, G., Local Structure and Dynamics of Water Absorbed in Poly(ether imide): A Hydrogen Bonding Anatomy. *J. Phys. Chem. B* **2017,** *121* (14), 3162-3176.

102. Kausar, A.; Siddiq, M., Poly(ether-imide)/polyurethane foams reinforced with graphene nanoplatelet: Microstructure, thermal stability, and flame resistance. *Int. J. Polym. Anal. Charact.* **2016,** *21* (5), 436-446.

103. Kumar, S.; Li, B.; Caceres, S.; Maguire, R. G.; Zhong, W. H., Dramatic property enhancement in polyetherimide using low-cost commercially functionalized multi-walled carbon nanotubes via a facile solution processing method. *Nanotechnology* **2009,** *20* (46).

104. Senthilkumar, S.; Rajesh, S.; Mohan, D.; Soundararajan, P., Preparation, Characterization, and Performance Evaluation of Poly(Ether-imide) Incorporated Cellulose Acetate Ultrafiltration Membrane for Hemodialysis. *Sep. Sci. Technol.* **2013,** *48* (1), 66-75.

105. Jordan, J.; Jacob, K. I.; Tannenbaum, R.; Sharaf, M. A.; Jasiuk, I., Experimental trends in polymer nanocomposites - a review. *Materials Science and Engineering a-Structural Materials Properties Microstructure and Processing* **2005,** *393* (1-2), 1-11.

106. Iwamoto, S.; Isogai, A.; Iwata, T., Structure and Mechanical Properties of Wet-Spun Fibers Made from Natural Cellulose Nanofibers. *Biomacromolecules* **2011,** *12* (3), 831-836.

107. Qiu, C. B.; Zhu, K. K.; Yang, W. X.; Wang, Y.; Zhang, L. N.; Chen, F.; Fu, Q., Super Strong All-Cellulose Composite Filaments by Combination of Inducing Nanofiber Formation and Adding Nanofibrillated Cellulose. *Biomacromolecules* **2018,** *19* (11), 4386-4395.

108. Yeh, G. S. Y., Order in Amorphous Polystyrenes as Revealed by Electron-Diffraction and Diffraction Microscopy. *Journal of Macromolecular Science-Physics* **1972,** *B 6* (3), 451-&.

109. Khayet, M.; Garcia-Payo, M. C., X-Ray diffraction study of polyethersulfone polymer, flat-sheet and hollow fibers prepared from the same under different gas-gaps. *Desalination* **2009,** *245* (1-3), 494-500.

110. Leal, A. A.; Mohanty, G.; Reifler, F. A.; Michler, J.; Hufenus, R., Mechanical response of melt-spun amorphous filaments. *Science and Technology of Advanced Materials* **2014,** *15* (3).

111. Luo, F.; Liu, X. H.; Shao, C. G.; Zhang, J. X.; Shen, C. Y.; Guo, Z. H., Micromechanical analysis of molecular orientation in high-temperature creep of polycarbonate. *Materials & Design* **2018,**

*144*, 25-31.

112. Murthy, N. S.; Minor, H.; Bednarczyk, C.; Krimm, S., Structure of the Amorphous Phase in Oriented Polymers. *Macromolecules* **1993,** *26* (7), 1712-1721.

113. Yeh, G. S. Y., Order in amorphous polystyrenes as revealed by electron diffraction and diffraction microscopy. *Journal of Macromolecular Science, Part B* **1972,** *6* (3), 451-463.

114. Dong, J.; Yin, C. Q.; Lin, J. Y.; Zhang, D. B.; Zhang, Q. H., Evolution of the microstructure and morphology of polyimide fibers during heat-drawing process. *Rsc Adv* **2014,** *4* (84), 44666-44673.

115. Yin, C.; Dong, J.; Tan, W.; Lin, J.; Chen, D.; Zhang, Q., Strain-induced crystallization of polyimide fibers containing 2-(4-aminophenyl)-5-aminobenzimidazole moiety. *Polymer* **2015,** *75*, 178-186.

116. Brown, H. R.; Mills, P. J.; Kramer, E. J., A Saxs Study of a Single Crack and Craze in Plasticized Polystyrene. *J Polym Sci Pol Phys* **1985,** *23* (9), 1857-1867.

117. Luo, F.; Liu, X. H.; Yan, C. G.; Liu, H.; Dong, M. Y.; Mai, X. M.; Shen, C. Y.; Liu, C. T.; Zhang, J. X.; Wang, N.; Guo, Z. H., Molecular orientation dependent dynamic viscoelasticity in uni-axially drawn polycarbonate. *Polym. Test.* **2018,** *69*, 528-535.

118. Chae, H. G.; Choi, Y. H.; Minus, M. L.; Kumar, S., Carbon nanotube reinforced small diameter polyacrylonitrile based carbon fiber. *Compos. Sci. Technol.* **2009,** *69* (3-4), 406-413.

119. Penning, J. P.; van Ruiten, J.; Brouwer, R.; Gabrielse, W., Orientation and structure development in melt-spun Nylon-6 fibres. *Polymer* **2003,** *44* (19), 5869-5876.

120. Haji, A.; Rahbar, R. S.; Kalantari, B., The Effect of Hot Multistage Drawing on Molecular Structure and Optical Properties of Polyethylene Terephthalate Fibers. *Materials Research-Ibero-American Journal of Materials* **2012,** *15* (4), 554-560.

121. Stachurski, Z. H., Strength and deformation of rigid polymers: the stress-strain curve in amorphous PMMA. *Polymer* **2003,** *44* (19), 6067-6076.

122. White, J. L.; Spruiell, J. E., Specification of Biaxial Orientation in Amorphous and Crystalline Polymers. *Polym. Eng. Sci.* **1981,** *21* (13), 859-868.

123. Xu, R. J.; Xie, J. Y.; Lei, C. H., Influence of melt-draw ratio on the crystalline behaviour of a polylactic acid cast film with a chi structure. *Rsc Adv* **2017,** *7* (63), 39914-39921.

## Acknowledgements

First of all, I would like to express my appreciation and gratitude to my advisor, Professor Han-Gi Chae. Thanks to him, I could get a precious chance to join his lab. I have been delighted to be a member of PNC lab. With his unbounded confidence incredible patience and timely wisdom, I would have done my research works appropriately. His counsel and advice on both research and my career have been priceless. It would also like to express my deepest appreciation to Professor Myoung Hoon Song and Hyun-Wook Lee for serving as my committee members despite their busy schedule. They let me have my defense a precious time. They offered their perceptive comments and suggestions, and it let my thesis be improved quality.

I would like to thank my first senior Sung Min Son who was one of our lab members. I got many things such as research region and inspiration of researches from her. Also, many thanks to our lab members, Dr. Young Ho Eom and Dr. Sang-Ha Hwang for their helpful advice and Jung-Eun Lee, Hye Jin Ju, So Jeong Heo, Min Jeong Kim, Dong-Je Lee and Ga-Hyeun Lee for their cooperation and commitment. They have been so nice to me for 2 years and I cannot forget this experience forever. It makes me better person than before. Also, I would like to thank my co-workers, Su Jeong Yeom and Sujin Kang. They have helped me understand and do research of sodium ion battery with them together. I also have learned from them, and I would express my appreciation to them. I am really grateful to my parents and older sister. They always understand and support me. It would never have been possible to complete this master's thesis without the help, guidance and support of many people.